

Present-day climate of Antarctica
A study with a regional atmospheric climate model

Het hedendaagse klimaat van Antarctica
een studie met een regionaal atmosferisch klimaat model

(met een samenvatting in het Nederlands)

PROEFSCHRIFT

ter verkrijging van de graad van doctor aan de Universiteit Utrecht
op gezag van de rector magnificus, prof. dr. J.C. Stoof,
ingevolge het besluit van het college voor promoties
in het openbaar te verdedigen op

maandag 11 februari 2008 des middags om 16.15 uur

door

Willem Jan van de Berg

geboren op 8 augustus 1979 te Nieuw-Amsterdam

Promotor: Prof. dr. J. Oerlemans
Co-promotoren: Dr. M. R. van den Broeke
Dr. E. van Meijgaard

*When I consider your heavens, the work of your fingers,
The moon and the stars, which you have ordained;
What is man, that you think of him?
The son of man, that you care for him?*

Psalms 8: 4-5, World English Bible

Cover: Antarctica on the globe. The surface mass balance (Antarctica), sea ice cover of October 15, 2003 (white to blue shadings) and model domain (blue box) are shown. Back cover: Northern hemisphere sea ice cover of October 15, 2003.

ISBN 978-090-393-4749-2

Contents

1	Introduction	1
1.1	Key aspects of the climate of Antarctica	3
1.1.1	Temperature	3
1.1.2	Atmospheric circulation	5
1.1.3	Precipitation	5
1.1.4	The ice sheet as an climate archive	5
1.1.5	Regional climate models	6
1.2	Antarctica in a changing global climate	6
1.3	Ice sheet mass balance	9
1.3.1	Mass balance estimates from satellite altimetry	10
1.3.2	Mass balance estimates from gravity	11
1.3.3	Mass budget using inSAR	11
1.3.4	Current level of understanding	13
1.4	Surface mass balance	14
1.5	Contents of this thesis	16
2	Characteristics of the Antarctic surface mass balance	19
2.1	Introduction	19
2.2	Model description	21
2.2.1	Snow albedo	21
2.2.2	Surface roughness lengths	22
2.2.3	Snow model	22
2.2.4	Correction of the liquid and solid precipitation	22
2.3	Results	23
2.3.1	Solid precipitation	23
2.3.2	Sublimation	23
2.3.3	Melt	26
2.3.4	Surface mass balance (SMB)	26
2.3.5	Seasonality of the mass balance	27
2.3.6	Interannual variability and trends	29
2.4	Discussion	32
2.4.1	Spatial distribution of measured and modeled SMB	32
2.4.2	The integrated SMB	33

2.4.3	Interannual variability and trends	33
2.5	Conclusions	33
3	Reassessment of the Antarctic surface mass balance	35
3.1	Introduction	35
3.2	Model description	36
3.3	Observations and data handling	37
3.3.1	Excluded areas	39
3.3.2	Model interpolation	41
3.3.3	Observationally dense areas	42
3.4	Results	43
3.4.1	RACMO2/ANT compared to V99	43
3.4.2	RACMO2/ANT compared to observations	45
3.4.3	Impact of temporal mismatch	45
3.4.4	Elevation and SMB	46
3.5	Discussion	48
3.5.1	Statistical robustness of the results	48
3.5.2	An evaluation of model performance	50
3.5.3	Towards a better understanding of Antarctic SMB	51
3.6	Conclusions	53
4	Error evaluation of a surface mass balance estimate	57
4.1	Introduction	57
4.2	Method	58
4.2.1	Definition of error margins	58
4.2.2	Verifying error margins	58
4.2.3	Spatial error autocorrelation	59
4.2.4	Error for basin mean SMB	60
4.3	Application	61
4.4	Discussion	65
5	Heat budget of the lower East Antarctic atmosphere	67
5.1	Introduction	68
5.2	Model description	69
5.3	The heat budget	70
5.3.1	Derivation of temperature tendency equation	70
5.3.2	Calculation of individual terms	71
5.4	Model evaluation	72
5.4.1	Temperature and wind	72
5.4.2	Surface energy budget	73
5.5	Results	76
5.5.1	Binning procedure	76
5.5.2	Climatological setting	76
5.5.3	Winter heat budgets	79
5.5.4	Summer heat budgets	85

5.6	Conclusions	87
6	Factors Controlling the Near Surface Temperature in Antarctica	89
6.1	Introduction	89
6.2	Model description and evaluation	90
6.3	Methods	94
6.3.1	Definition of the heat budget	94
6.3.2	Definition of free atmosphere parameters	95
6.3.3	Definition of ABL depth	95
6.3.4	Example of vertical profiles	95
6.4	Results: Winter	97
6.4.1	External heating and surface interactions	97
6.4.2	Heat advection in East Antarctica	99
6.4.3	Spatial distribution of $AdvH$ and $AdvV$	101
6.4.4	Synoptic and persistent large-scale and ABL contributions to $AdvH$.	103
6.5	Results: Summer	107
6.5.1	External heating and surface interactions	107
6.5.2	Heat advection	107
6.6	Summary and conclusions	110
7	Suggestions for future work	111
7.1	Applications for heat budget analyses	111
7.2	SMB of the Antarctic ice sheet	112
7.3	A pilot study with decreased ice crystal fall speed	112
	Bibliography	117
	Samenvatting	127
	Dankwoord	133
	Curriculum Vitae	135
	Publications	137

Chapter 1

Introduction

Antarctica is the extreme continent on Earth. It is also the only continent without original inhabitants - not without reason, the climate is truly hostile. The lowest near-surface temperature of $-89.2\text{ }^{\circ}\text{C}$ and the highest annual mean near-surface wind speed of 16.9 m s^{-1} have been observed here.

Although remote, Antarctica is an important component of the global climate system. First and foremost, 90% of the Earth's glacier ice is stored in the Antarctic ice sheet. If all this ice would be added to the oceans, global sea level would rise by 60 m (*Huybrechts et al.*, 2000). Moreover, Antarctica represents a major heat sink in the global energy budget, and influences the Earth's climate in many respects. The oceans surrounding Antarctica are an important chain in the global ocean circulation. The Weddell and Ross Seas are the second largest producers of deep ocean water (*Orsi et al.*, 1999; *Ganachaud and Wunsch*, 2000). Deep water formation relates, among other processes, to sea ice production, a process that is driven by the persistent outflow of cold continental air from the Filchner-Ronne and Ross Ice Shelves to the ocean. These examples show that although Antarctica is remote it surely is not disconnected from global climate.

It is therefore important to understand the climate of Antarctica. In this thesis, several aspects of Antarctica's climate are studied in detail. To that end, we use output of a regional atmospheric climate model.

This chapter deals with some basic characteristics of the climate of Antarctica and sketches our current level of understanding. This includes ongoing climate change in Antarctica. We also discuss observations of the ice sheet mass balance and, more specifically, of the surface mass balance (SMB). These observations directly touch upon the problem of Antarctica's contribution to past and present sea level rise.

Topographic locations referred to in this chapter are shown in Figure 1.1.

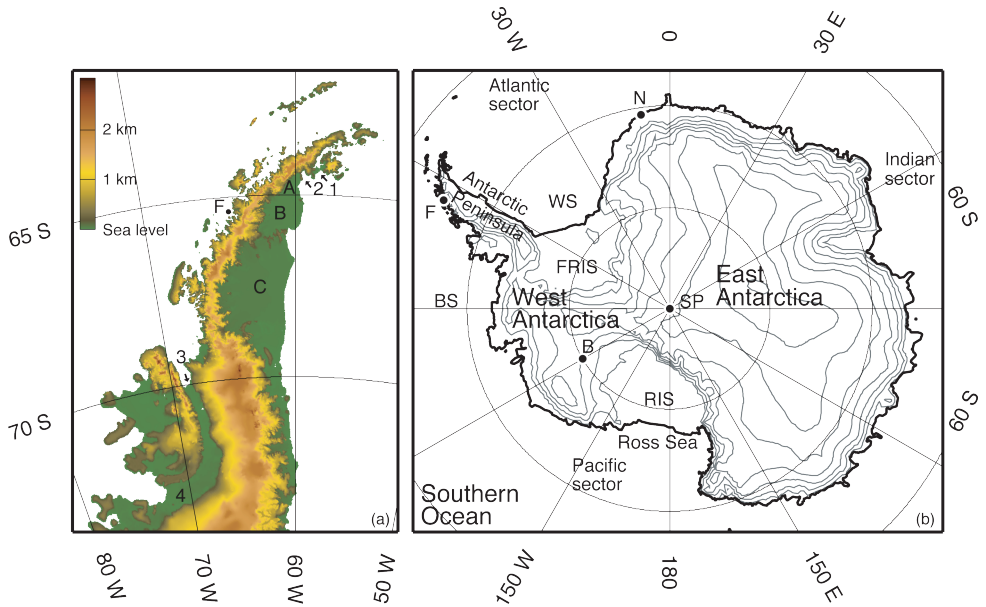


Figure 1.1: Geographic locations mentioned in this chapter. (a) The Antarctic Peninsula. A, B, C, 1 and 2 are the Larsen-A, -B -C Ice Shelves, Prince Gustav Channel and the Larsen Inlet, respectively. The George VI Ice Shelf is situated between 3 and 4. Faraday/Vernadsky is located at F. Surface elevation data are from Liu *et al.* (2001). (b) Antarctica. The Filchner-Ronne and Ross Ice Shelves; Weddell and Bellingshausen Seas are abbreviated to FRIS, RIS, WS and BS, respectively. Amundsen-Scott South Pole Station, Neumayer, Byrd and Faraday/Vernadsky are denoted by SP, N, B and F. Gray elevation contours represent 500 m elevation intervals.

1.1 Key aspects of the climate of Antarctica

1.1.1 Temperature

The most conspicuous aspect of Antarctic climate is the low near-surface temperature (Figure 1.2a). The near-surface temperature in Antarctica is determined, among other factors, by surface elevation, latitude, continentality and surface slope. The lowest temperatures are found around the ice domes of East Antarctica. The Filchner-Ronne and Ross Ice Shelves, although situated near sea-level, are also relatively cold, especially in their centers. The Antarctic Peninsula protrudes far to the north and is therefore relatively mild compared to mainland Antarctica. During summer, any remaining sea ice is largely confined to the Bellingshausen and Weddell Seas. The minimum sea ice extent occurs in February, after which the sea ice edge rapidly expands northwards to effectively double the size of Antarctica in September, when the maximum sea ice extent is reached.

Another unusual aspect of Antarctic climate is the coreless winter. The yearly 2 m temperature cycle at Amundsen-Scott South Pole Station (Figure 1.2b) is typical for inland Antarctica. The winter lasts from April until the end of September, with monthly mean temperatures that are more or less constant: obviously, inland Antarctica has a coreless winter. The summer at South Pole is short and peaked, but temperatures remain well below zero. A similar, but less cold cycle is observed at Byrd (80° S, 120° W), West Antarctica. Neumayer (71° S, 8° W) is an example of a coastal station. Here, monthly mean summer temperatures are also well below zero, but surface snow melt is regularly observed. At Neumayer, melt can incidentally also occur in the other seasons when warm air masses are transported southward by cyclones. Faraday, now renamed Vernadsky, located on the west coast of the Antarctic Peninsula, has the most significant melt season. Winter temperatures at Vernadsky are well below zero, but the inter-annual variability is large: observed monthly mean July temperatures range from -20.1 to -2.6 °C. This is a direct effect of the strong variability in sea ice cover in the Bellingshausen Sea, west of Vernadsky.

A third critical aspect of Antarctic temperatures is the quasi-continuous surface-based temperature inversion. Figure 1.2c shows radiosonde observations from Amundsen-Scott South Pole Station for January and the winter period (MJJAS) of 1998. The surface inversion indirectly originates from a surface radiation deficit: in the polar night, net longwave radiation emission cools the surface. In turn, the surface cools the near-surface air mainly through turbulent exchange. This transport of sensible heat from the air towards the surface is maintained by the near-surface wind shear. The atmosphere over Antarctica and the surrounding sea ice shows this temperature inversion quasi-permanently during winter. In summer, insolation reduces or totally removes the inversion during daytime; the inversion then mostly occurs during the night. The inversion height is a measure for the depth of the air layer that has direct interaction with the surface, the atmospheric boundary layer (ABL). In Antarctica, the ABL depth ranges from less than 100 m to over 1000 m, depending on the meteorological conditions.

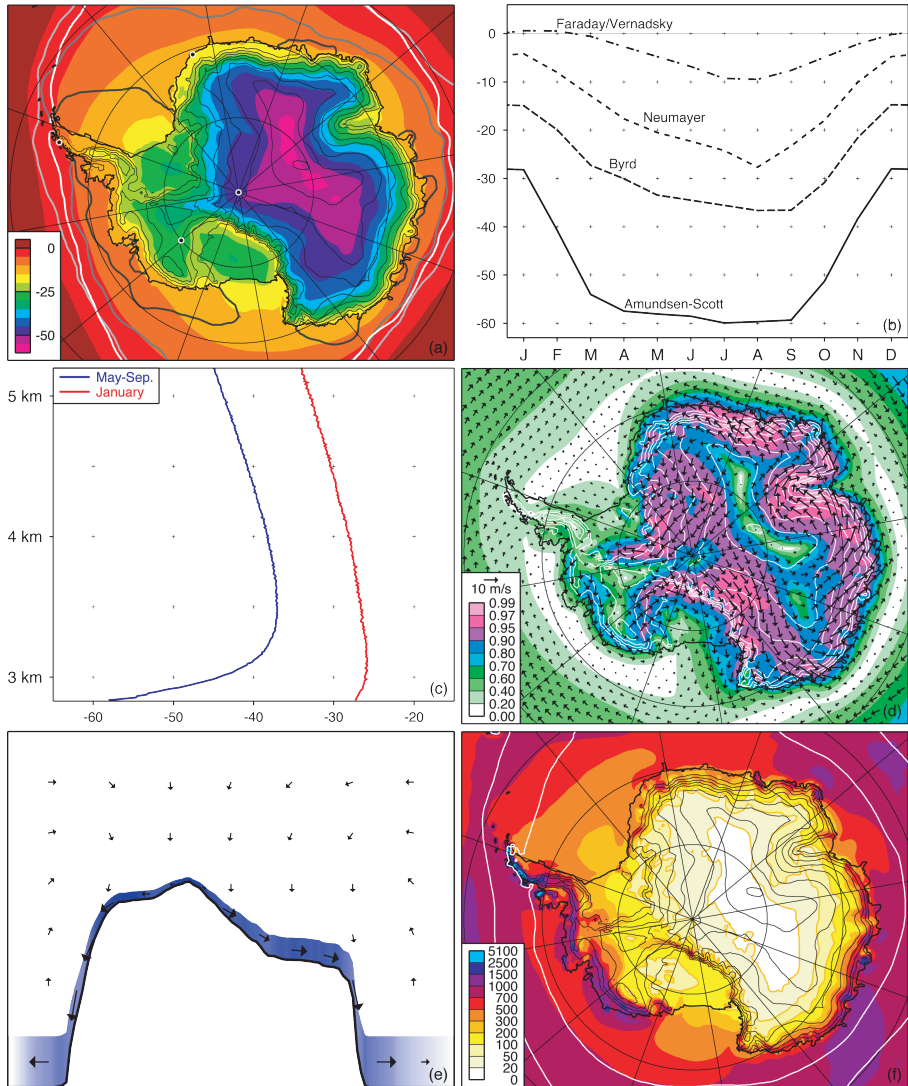


Figure 1.2: Key aspects of Antarctic climate. (a) Annual mean 2 m temperature [°C] in colors, and sea ice edge (30% coverage) in February (dark grey line), May, August and November (white line). (b) Seasonal cycle of 2 m temperature [°C] for four locations in Antarctica, also marked in (a). Data is from the SCAR REference Antarctic Data for Environmental Research (READER) project. (c) January and winter (MJJAS) 1998 upper air temperatures [°C] observed at Amundsen-Scott. Data from <http://uwamrc.ssec.wisc.edu/amrc.html>. (d) Annual mean 10 m wind (vectors) and directional constancy. (e) Sketch of the mean meridional and vertical circulation over Antarctica. (f) Annual precipitation in mm per year. White lines show where 50 and 90% of precipitation is snow. Black/white contours in (a), (d) and (f) represent 500 m elevation intervals.

1.1.2 Atmospheric circulation

Another defining aspect of Antarctic ABL climate is the persistent katabatic circulation, shown in Figure 1.2d. Cold air is heavier than warm air, and that is why the cold air below the surface inversion tends to flow downhill. Katabatic winds thus require a surface-based temperature inversion. As noted above, the surface-based temperature inversion in Antarctica is mainly due to cooling by turbulent mixing, a process which requires near-surface wind shear. The katabatic wind and the near-surface temperature inversion are thus tightly coupled. Due to the vast size of Antarctica and the continuous forcing, the Coriolis force deflects these winds to the left into a cross-slope direction, but friction maintains a downslope component. Katabatic winds are weak near the domes, where the surface slope is small. The strongest katabatic winds are found near the coast, where the ice sheet has its maximum slope. Since the inversion is nearly continuously present during winter, katabatic winds can be ceaseless. The large-scale circulation is also anti-cyclonic in the lower atmosphere over Antarctica, and thus aligns with the katabatic winds. As a result, the wind directional constancy is very high over the slopes of Antarctica. Note from Figure 1.2d that a few hundred km offshore the mean wind vector vanishes. This is the average location of the circumpolar pressure trough, the most common location of cyclonic lows. North of it, the westerlies are found, south of it easterlies prevail near the surface.

Superimposed on this outspoken zonal circulation, the wintertime Antarctic troposphere has a meridional and vertical circulation as well (Figure 1.2e). The katabatic flow drains cold air downhill in the ABL, causing the ABL wind field to be divergent. This forces large-scale subsidence, maintaining the relatively high temperatures above the capping inversion. In order to balance the subsidence, the net transport of mass in the free troposphere is poleward. This meridional circulation is strongest in winter, but persists in the other seasons.

1.1.3 Precipitation

Besides temperature and wind, precipitation is another principal aspect of Antarctic climate, as it maintains the ice sheet. Figure 1.2f shows total precipitation, in mm water equivalents. White lines mark where 50 and 90% of the precipitation consists of snow. The plateau of Antarctica is very dry with typical annual precipitation below 100 mm. The interior ice sheet, with less than 250 mm precipitation per year and an area of about 12×10^6 km², represents a cold desert larger than the Sahara (9×10^6 km²). In contrast, the west coast of the Antarctic Peninsula is very wet, with annual precipitation rates in excess of 2000 mm. On average, coastal Antarctica receives 400 mm, the equivalent of about 1.2 m of snow. More precipitation is found in regions where the upper air circulation is partly directed inland. Topographic promontories also generate more snow. Over the Southern Ocean, precipitation rates are rather uniform, but the precipitation shadow effect of the Antarctic Peninsula can be traced to the east over thousands of km.

1.1.4 The ice sheet as an climate archive

Extensive glaciation is believed to have started in Antarctica about 34 million year ago, although glaciation did not become continuous until 15 million year ago. Because no melt

occurs in the interior, the ice sheet acts as an archive of past climate. After deposition, snow densifies to firn (old and compacted snow) and transforms subsequently into ice, in the deeper layers. Ideally, the ice column at the ice sheet domes only moves vertically, representing a stacked history of climate. With increasing depth, the ice layers gradually thin, resulting in old bottom ice. The oldest ice analyzed is about 740,000 year old, but it is believed that the oldest ice still present in access in Antarctica has an age of one million year (*EPICA community members*, 2004). The analysis of ice cores is an important tool to expand our knowledge of Antarctic climate to the times prior to that of direct meteorological observations.

1.1.5 Regional climate models

Because of the sparsity of *in situ* observations, climate models in general, and regional climate models (RCM's) in particular, have contributed greatly to our knowledge of Antarctic climate. In situ observations may not provide such a complete and detailed spatial and temporal picture, but they are indispensable to the evaluation of models, and therefore very important. Satellites have also enormously enhanced the coverage of observations. However, their observations range as far south as their orbit, and not every climate property can be monitored from space, e.g. the surface mass balance. Moreover, satellites have been in operation for a limited period of time. For climate diagnostics, RCM's currently prevail over General Circulation Models (GCM's), because RCM's can be evaluated on a higher spatial resolution and their model physics can be adapted to Antarctic conditions. Figure 1.2, for instance, shows 2 m temperature (a), wind (d) and SMB (f) patterns derived from the regional climate model RACMO2/ANT.

1.2 Antarctica in a changing global climate

During the last decades, the average global tropospheric temperature has risen significantly, and the indications are that this rise is mainly of anthropogenic origin. The fourth assessment report of the IPCC (2007, page 10) states that “*most of the observed increase in global average temperatures since the mid-20th century is very likely due to the observed increase in anthropogenic greenhouse gas concentrations. This is an advance since the TARs conclusion that ‘most of the observed warming over the last 50 years is likely to have been due to the increase in greenhouse gas concentrations’.* *Discernible human influences now extend to other aspects of climate, including ocean warming, continental-average temperatures, temperature extremes and wind patterns.*”

The most tangible change in Antarctica was the collapse of the Larsen-A and B Ice Shelves in 1995 and 2002, respectively. Figure 1.3 shows satellite pictures of the collapse sequence of the Larsen-B Ice Shelf, a floating glacier with an area of about 3250 km², comparable in size to the Dutch province of Overijssel. Until its collapse, the Larsen-B Ice Shelf had been stable throughout the Holocene (*Domack et al.*, 2005), indicating that the collapse lies outside the range of recent natural climate variability. In contrast, the Larsen-A Ice Shelf, the Larsen Inlet and the Prince Gustav Channel, which became shelf-free in 1998/2002, 1998/99 and 1995, respectively, have all been without ice shelves during various stages of the Holocene (*Pudsey and Evans*, 2001). Another ice shelf with a shelf-free stage

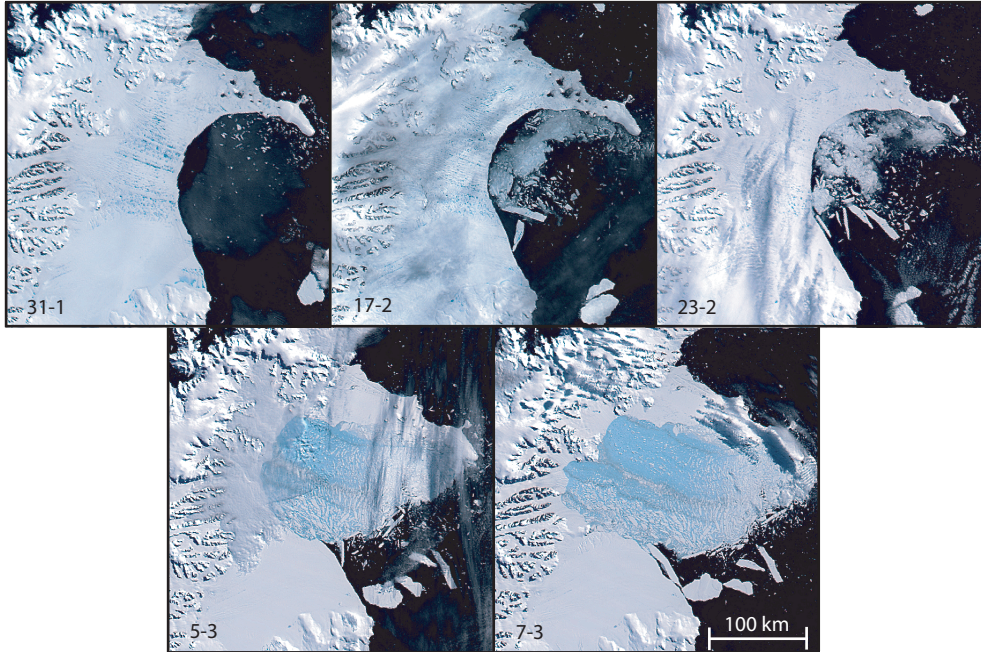


Figure 1.3: MODIS images of the collapse of the Larsen B Ice Shelf in 2002. Image courtesy of Ted Scambos, National Snow and Ice Data Center (NSIDC).

during the Holocene is the George VI Ice Shelf (*Bentley et al.*, 2005), but this ice shelf is still present.

The collapse of the Larsen-B Ice Shelf is likely caused by a combination of atmospheric and oceanic forcings. *Shepherd et al.* (2003) show that the ice shelf progressively thinned since the start of observations in 1992. This thinning could be partly caused by summer surface melt and subsequent firn densification, but is most likely the result of basal melt due to rising ocean temperatures. Increased surface melt has been identified as a cause for ice shelf collapse. *Van den Broeke* (2005) showed that the Larsen-B Ice Shelf experienced exceptional surface melt during the 2001/02 summer, just prior to its collapse. Numerous melt-water ponds visible on the satellite image of January 31 support this (Figure 1.3). Similar melt ponds were observed on the Larsen-A and Wilkins Ice Shelves prior their collapse (*Scambos et al.*, 2000). Melt ponds indicate that ample water was available to fill crevasses. Crevasses can fully penetrate through the ice once filled with water (*Van der Veen*, 1998). *MacAyeal et al.* (2003) argued that once the ice shelf has fragmented, capsizing of the fragments leads to a rapid disintegration of the ice shelf. The appearance of gray debris lines in the satellite image on March 7 directly after the collapse confirms the capsize hypothesis.

Prior to the collapse of the Larsen-B Ice Shelf, during the second part of the 20th century, the Antarctic Peninsula did experience rapid atmospheric warming. Temperature records from manned stations show temperature increases (Figure 1.4) that greatly exceed the global average (*Vaughan et al.*, 2003). The significance of the trends in these records is not over-

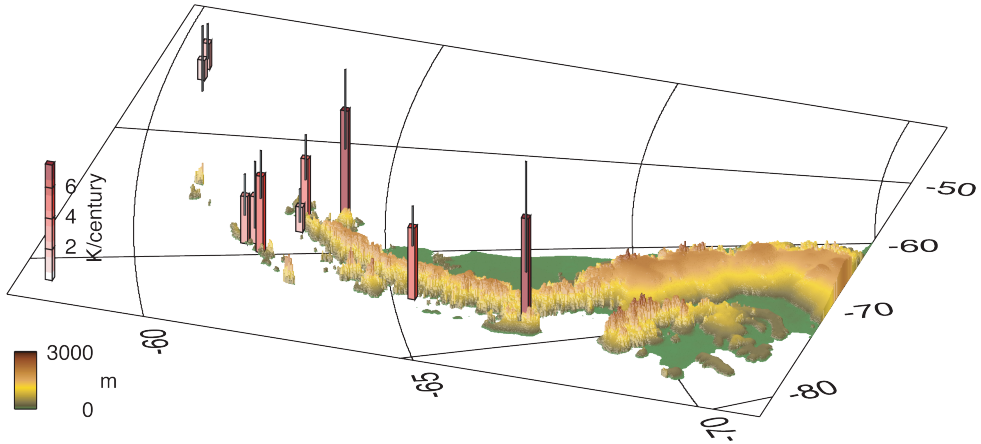


Figure 1.4: Observed annual temperature trends with uncertainty [K per century] in the Antarctic Peninsula since the start of observations. Observational data is from the Reference Antarctic Data for Environmental Research (READER) project, surface elevation from Liu *et al.* (2001).

whelming, due to the large year-to-year variability in winter temperatures. However, unambiguous signs of warming during the 20th century are provided by the retreat of several ice shelves, following the southward migration of the -9°C isotherm (Vaughan and Doake, 1996; Morris and Vaughan, 2003). Several former tributary glaciers have dramatically sped up after the ice shelf disappeared (De Angelis and Skvarca, 2003). Furthermore, 78% of the glaciers on the Antarctic Peninsula have retreated since they were first measured about 50 years ago (Cook *et al.*, 2005). Sea ice cover west of the Antarctic Peninsula is reducing (Liu *et al.*, 2004), although it is unclear whether this is a cause for or a result of the rapid warming (Vaughan *et al.*, 2003). In addition, ecological changes have been observed, for example, in the breeding locations of several penguin species (c.f. Smith *et al.*, 1999).

In contrast, no significant warming has been observed in the rest of Antarctica. The longest temperature records from this region are from manned stations and go back to 1957. All these stations are located along the coast of East Antarctica, with the exception of Amundsen-Scott South Pole Station and Vostok. No coherent or significant cooling or warming trend is found for any of these stations (Turner *et al.*, 2005).

Satellite observations can provide continent-wide trend estimates. Comiso (2000) used satellite observations of infrared emission to find a slight cooling in most of Antarctica for the time period 1979-1998 for the months January and July. However, surface emission of long-wave radiation can only be observed during cloud free conditions. Therefore, this estimate is sensitive to changes in cloudiness, since clouds have on average a warming effect on the surface temperature in Antarctica (King and Turner, 1997; Van den Broeke *et al.*, 2006a). Torinesi *et al.* (2003) provided additional indications for a cooling trend in Antarctica. They showed that along the coast of Antarctica, satellite observed melt duration and extent slightly decreased since 1979.

Estimates of temperature trends in the free atmosphere are also hampered by a lack of observations. Reasonably long upper time series of air temperature have been collected at

only 12 stations in Antarctica. Using these data, *Turner et al.* (2006) found a significant tropospheric warming signal over Antarctica for winter (JJA). In contrast, *Thompson and Solomon* (2002) observed a cooling trend during summer and autumn. *Johanson and Fu* (2007) considered satellite observations of average troposphere temperature, and found a slight cooling. The winter warming thus appears to be outweighed by summer and autumn cooling.

Unluckily, state-of-the-art global circulation models are still unable to reliably simulate the current temperature changes over the Antarctic (*Vaughan et al.*, 2001). Even the European Center for Medium-Range Weather Forecasts (ECMWF) re-analysis (ERA-40) shows an unrealistically strong and uniform trend over the Antarctic (*Johanson and Fu*, 2007; *Turner et al.*, 2005).

Numerous papers have been devoted to explain Antarctic near-surface temperature variability and trends, for example, *Thompson and Solomon* (2002); *Schneider et al.* (2004); *Shindell and Schmidt* (2004); *Van den Broeke and van Lipzig* (2004) and *Marshall et al.* (2006). The general picture that emerges is that the Southern Annular Mode (SAM), sometimes named the Antarctic Oscillation (AAO), is the main forcing mechanism for Antarctic temperature variability. Variations in the SAM represent variations in the strength of the circumpolar westerly circulation. A high SAM index represents an intensified zonal circulation, increasing near-surface temperatures in the northern part of the Antarctic Peninsula but decreasing temperatures in the mainland of Antarctica. Since the mid-1960s, the SAM has gradually become more positive, explaining a substantial part of the observed temperature patterns. The increase in the SAM has been explained as a joint result of stratospheric ozone depletion and increasing concentrations of greenhouse gases.

Statistical analysis of observational data is a powerful tool to demonstrate relations between circulation indices and Antarctic climate, but the physical mechanisms often remain concealed. That is why GCM's and RCM's are increasingly being used. GCM's do highlight forcing mechanisms and enable investigation of future climate responses. Since GCM's still have a coarse resolution, typically 2-3°, RCM's are the most suitable tool to investigate regional response patterns and processes in Antarctica. Examples of such studies are *Van Lipzig et al.* (2002a) and *Guo et al.* (2004).

1.3 Ice sheet mass balance

The Greenland ice sheet could irreversibly disintegrate in a warmer climate (e.g. *Greve*, 2000; *Toniazzo et al.*, 2004). But even in a warmer future climate, the vast majority of Antarctica will remain frozen. Nevertheless, climate variations will influence the mass balance of the Antarctic ice sheet. For example, snow accumulation will likely increase for higher atmospheric temperatures (*Van Lipzig et al.*, 2002a; *Huybrechts et al.*, 2004). Changes in the total ice volume of Antarctica could have a large impact on all coastal regions on Earth. Due to the vast volume of the ice sheet, even relatively minor changes correspond to changes of several m in global sea level.

Like for all glaciers, the ice volume of an ice sheet stays constant if the mass balance (or mass budget) is zero. For global sea level considerations, only the grounded part of the ice sheet is relevant. Melting or break-up of ice shelves does not have a (direct) effect

Table 1.1: Recent estimates of Antarctic mass balance. Figure 1.6 visualizes the estimates.

Study	Abbreviation	Method	Survey period	Area %	mass balance Gt yr ⁻¹
<i>Zwally et al. (2005)</i>	Z05	Altimetry	1992-2001	100*	-31 ± 12
<i>Wingham et al. (2006)</i>	W06	Altimetry	1992-2003	72	27 ± 29
<i>Velicogna and Wahr (2006)</i>	V06	Gravity	2002-2005	100	-139 ± 74
<i>Ramillien et al. (2006)</i>	R06	Gravity	2002-2005	100	-40 ± 36
<i>Rignot and Thomas (2002)</i>		Mass Budget	1995-2000	59	-26 ± 27
<i>Rignot et al. (2008)</i>	R07	Mass Budget	1992-2006	100**	-141 ± 57

*Surveyed 77%, remainder by interpolation. **Surveyed 82%, remainder by extrapolation

on sea level, because ice shelves have already occupied their volume in the ocean. For a zero ice sheet mass balance, snow accumulation at the surface, reflecting a positive *surface* mass balance (SMB), balances the outflow of ice at the grounding line. Integrated over the Antarctic ice sheet, sublimation, surface melt and subsequent runoff are small. This means that nearly all accumulated mass leaves the ice sheet through basal melt of ice shelves and the calving of icebergs.

It has proven difficult to accurately estimate the present-day mass balance of the Antarctic ice sheet using in situ observations. Estimating the mass balance of a glacier from in situ observations requires regular visits of stakes that cover the glacier with some resolution. For Antarctica, this is not feasible. Furthermore, most of the accumulated ice flows from the grounded ice sheet into fringing ice shelves, which subsequently loose ice by iceberg calving and basal melting. Both these processes are also hard to quantify from direct measurements. As a result, the remaining uncertainty in the ice sheet mass balance by far exceeds any potential imbalance.

More accurate estimates of the mass balance of the Antarctic ice sheet became possible with the onset of the satellite era. Three methods are currently used: observation of volume change, mass change and mass budget. Recently published estimates using either of these three methods are listed in Table 1.1.

1.3.1 Mass balance estimates from satellite altimetry

Satellite altimetry can be used to track volume changes of the Antarctic ice sheet by means of changes in elevation. Observations started in 1992 with the launch of the European Remote-sensing Satellite (ERS). This satellite includes a radar by which surface elevation can be tracked with a footprint of ~ 10 km down to 81.5° S. Using these data, *Zwally et al. (2005)* and *Wingham et al. (2006)* provide an estimate of the mass balance of -31 ± 12 (1992 to 2001) and 27 ± 29 (1992 to 2003) Gt per year, respectively. *Davis et al. (2005)* also analyzed altimetry data, but he estimated the mass balance of a part of the Antarctic ice sheet only.

The simple fact that the two estimates differ significantly, indicates that translating ERS observations to mass changes suffers from fundamental uncertainties. Firstly, the area south of 81.5° S is outside the orbit of the satellite, leaving about 25% of the ice sheet unsurveyed.

Since most of the elevation variability is found along the coast, this limited coverage is in principle not a critical problem. Secondly, a relatively smooth and flat surface is required for a good signal to noise ratio. Consequently, the elevation changes for large parts of the coastal margins are uncertain. Thirdly, long-term local mass imbalances are superimposed on shorter-term variability in the depth of the firn layer. The depth of the firn layer, where snow compacts to ice, depends strongly on accumulation and temperature. In first order, it integrates SMB departures from the long term mean (*Zwally and Li, 2002*). SMB in Antarctica has large inter-annual variability, but also the decadal to centennial variability is significant (e.g. *Mosley-Thompson et al., 1995; Hofstede et al., 2004*). Since the observation period is just over a decade, the observed elevation trends still contain significant contributions of natural climate variability. *Van den Broeke et al. (2006b)* showed, using a RCM, that the SMB also has a significant natural decadal regional variability.

1.3.2 Mass balance estimates from gravity

The second method to estimate ice mass changes in Antarctica is by observing changes in the gravity field of the Earth. Observations are made by the Gravity Recovery and Climate Experiment (GRACE) satellites, starting from April 2002. The mission consists of two identical spacecrafts flying about 220 km apart in a polar orbit 500 km above the Earth. The variations in the gravity field are obtained from changes in the distance between the two satellites.

Gravity observations are not affected by density changes in the firn pack as altimetry observations are. Nonetheless, gravity field observations do not relate one-to-one to ice mass changes; the gravity signal also contains changes in atmospheric mass and the effect of post-glacial rebound, the viscoelastic response of the Earth's mantle to glacial unloading over the past several thousand years. Atmospheric mass directly relates to the local surface pressure and is therefore well defined. Post-glacial rebound in the Antarctic however is poorly constrained. Furthermore, the method to isolate mass changes in Antarctica is not straightforward, neither the method to regionalize mass budget fluctuations. All in all, the two estimates derived from GRACE observations (*Velicogna and Wahr, 2006; Ramillien et al., 2006*) also differ significantly (Table 1.1).

The largest uncertainty in the GRACE estimates is due to the short time span of the observations. Three years of observations is rather short in the light of the large variability of the Antarctic SMB (*Van de Berg et al., 2005; Monaghan et al., 2006*). This uncertainty will reduce when the GRACE mission continues and is followed-up by the Gravity field and steady-state Ocean Circulation Explorer (GOCE) in spring 2008.

1.3.3 Mass budget using inSAR

The third method to determine the mass budget is by direct calculation of the mass fluxes. The mass input is determined by the SMB over the grounded ice sheet of Antarctica; the mass flux passing the grounding line gives the mass output. *Rignot and Thomas (2002)* provided an estimate of -26 ± 27 Gt per year, using ice flow data of 59% of the coastal glaciers. An updated estimate for 82% of the glaciers, extrapolated to the entire Antarctic ice sheet, is presented by *Rignot et al. (2008)* (-141 ± 59 Gt per year). Drainage basin integrated results of this study are shown in Figure 1.5. Colors show the ice velocity, which range from stagnant

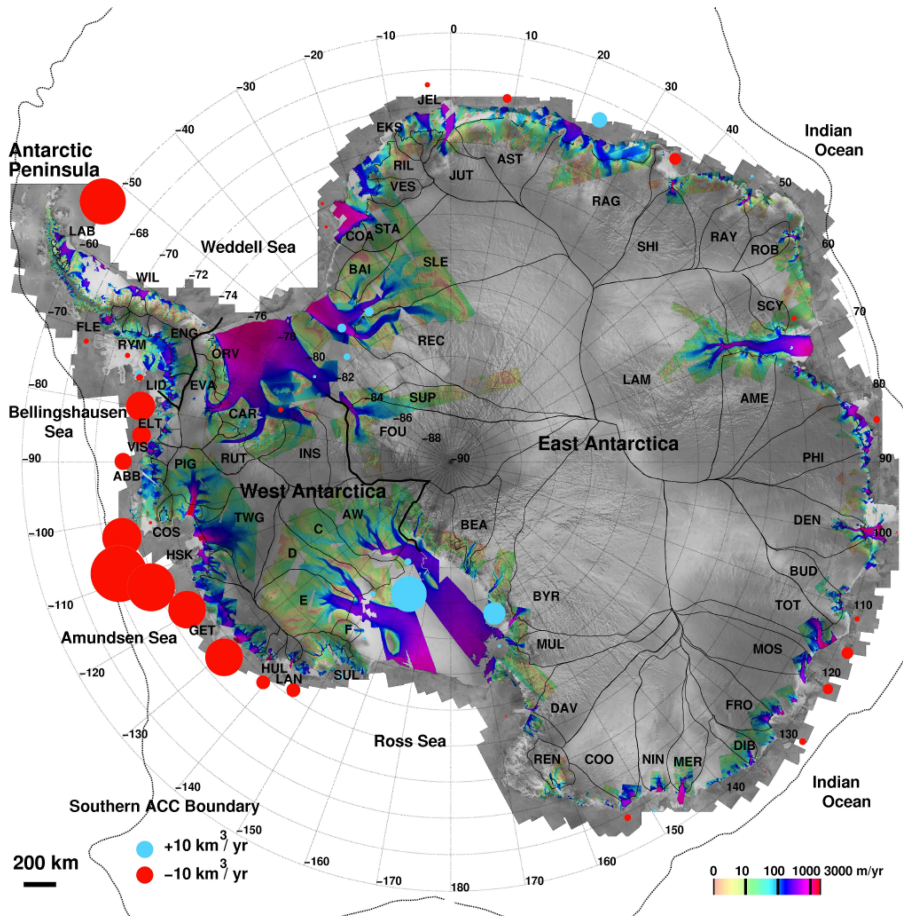


Figure 1.5: Ice velocity (blueish colors) and drainage basin integrated mass balance (red/blue circles) from Rignot et al. (2008).

up to several km per year. Red and blue circles show the imbalance per drainage basin; the circle radius increases proportional to the imbalance.

For an estimate of the solid ice flux, knowledge of the exact grounding line position, the local ice thickness and the ice velocity is required. For most of Antarctica, in situ observations of these quantities are not available, and must be derived from satellite observations. The grounding line location and ice velocity can be derived from interferometric synthetic-aperture radar (InSAR), mounted on the ERS-1 and ERS-2 satellites. The ice thickness can be estimated from surface elevation, using the fact that the ice is almost floating at the grounding line. Surface elevation is measured by several satellites. The ice sheet is covered by a firn layer, which has a lower density than ice. When surface elevation is converted into ice thickness, the firn layer must be taken into account; this firn layer depth can be modeled.

The strength of the mass budget method is that it directly estimates the mass balance of individual drainage basins in Antarctica, and that it is not sensitive to annual SMB variability. Its weakness is that the error margin will exceed any potential mass imbalance if not all input observations are accurately estimated. For example, the ice flux critically depends on the grounding line position. Small errors in the grounding line position result in amplified errors in the surface elevation at the grounding line and thus to large errors in the ice thickness and ice flux. Furthermore, SMB and mass outflow are determined for different time intervals. The ice velocity, which is determined with one or several monthly snapshots, may exhibit temporal variability. Finally, the SMB is still relatively uncertain; methods to estimate the SMB and its uncertainties will be discussed below in section 1.4.

1.3.4 Current level of understanding

Table 1.1 and Figure 1.6 show recent estimates of the Antarctic ice sheet mass balance. Agreement is lacking, because apparently the uncertainty margins of the estimates are underestimated. Agreement is even lacking between studies using the same method and data. The estimates range from -141 to +25 Gt per year, while a typical survey error margin is 75 Gt per year. Overall, it appears that Antarctica is presently losing mass by about 100 ± 75 Gt per year. Note that about 360 Gt water is needed to increase global sea level by 0.1 mm. For comparison, global sea level rise between 1961 and 2003 is estimated to be 1.8 ± 0.5 mm per year, so Antarctica is likely already contributing significantly to ongoing sea level rise (IPCC, 2007).

In spite of the differences among the methods, a consistent regional picture arises. East Antarctica is near balance or gaining mass due to an increase in SMB. The Antarctic Peninsula gains mass on the domes due to increased precipitation (Wingham *et al.*, 2006; Van den Broeke *et al.*, 2006b), but also loses mass along the coast (Cook *et al.*, 2005, and references therein). More importantly, West Antarctica bordering the Amundsen Sea is out of balance in all estimates. Estimates range from -136 to -47 Gt per year (Shepherd and Wingham, 2007). This loss is mainly due to changes in the outflow of glaciers that discharge in the Amundsen Sea (Figure 1.5). These outlet glaciers are marine-based and therefore vulnerable to changes in ocean temperatures. Although increasing attention is devoted to the dynamical behavior of glaciers, the level of understanding of nonlinear glacier flow is still low. Continued research and monitoring is therefore crucial.

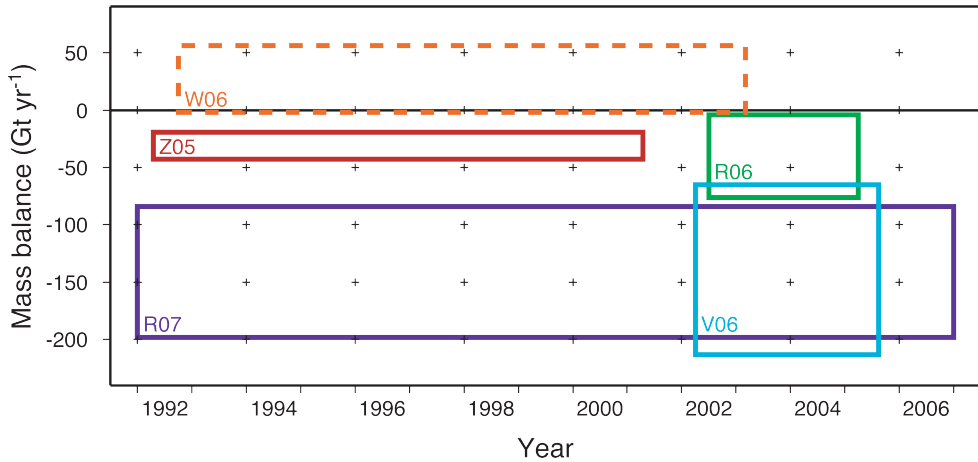


Figure 1.6: Visualization of recent mass balance estimates for Antarctica. The colored rectangles indicate the time span over which the estimates apply and the estimated range. Abbreviations are listed in Table 1.1. The survey of Wingham *et al.* (2006, W06) is dashed because it covers only 72% of Antarctica.

1.4 Surface mass balance

Accumulation of snow, i.e. a positive surface mass balance (SMB), is the source of ice for the Antarctic ice sheet. It is an essential aspect of our understanding of the current balance state of the ice sheet and predictions of its future mass balance. Estimates of the integrated SMB have suffered from a lack of in situ data, or rather, the remoteness and size of Antarctica which requires a large number of observations for a significant coverage. Unfortunately, no technique exists to date whereby the SMB can be measured directly or indirectly by satellite. As a result, recent estimates of the Antarctic SMB (i.e. *Arthern et al.* (2006) and *Van de Berg et al.* (2006)) differ by 18%.

In situ observations are the backbone of all estimates of the Antarctic SMB. The early observation methods, mostly based on the interpretation of snow stratigraphy, are subject to potentially large errors. Since the 1960s several more accurate observation methods have been developed, including tracing of nuclear bomb test and volcanic horizons in ice cores, and repeated measurements of snow stakes, occasionally grouped in stake farms or along transects. Nowadays, the SMB of a region is usually estimated with complementary usage of ice cores and a ground penetrating radar (GPR). A GPR detects reflective layers in the firn pack; these layers can be dated and followed along the profile, showing spatial SMB variability in great resolution. Such surveys have shown that along the coast and in the escarpment, the local variability of the SMB can be in the order of 100% over a km distance. Redistribution of snow by katabatic winds is significant (*Frezzotti et al.*, 2007).

About 1900 SMB observations from Antarctica are currently documented. Although this number may suggest that a reasonable coverage has been reached, several areas completely devoid of or without observations are still visible in Figure 1.7a. Extrapolation of SMB to these areas, in particular in the coastal zone, is highly uncertain. Extrapolations were first per-

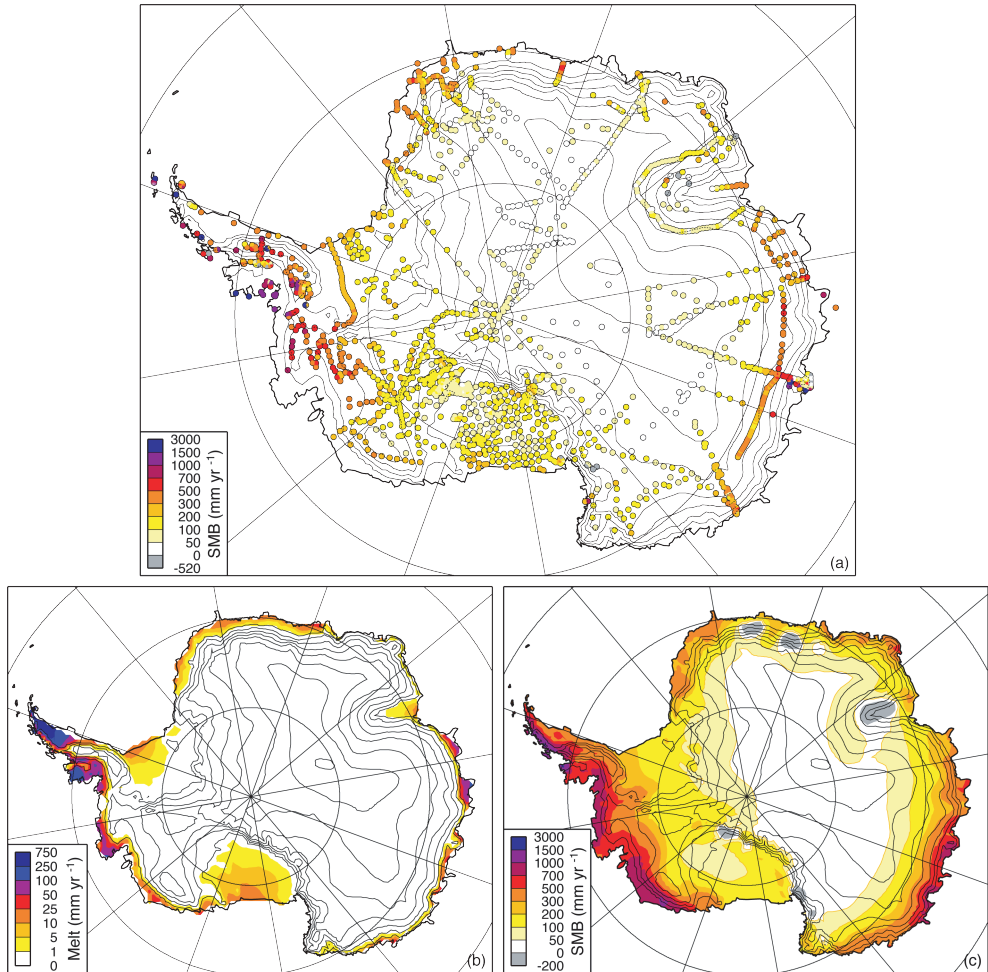


Figure 1.7: (a) A map of SMB observations in Antarctica. (b) Mean annual snow melt in Antarctica, as simulated by RACMO2/ANT. (c) Antarctic SMB as derived from RACMO1/ANT (Van Lipzig et al., 2002b). The black contours in all figures represent 500 m elevation intervals.

formed by visual interpretation, using knowledge of how the SMB depends on topography. Examples of this approach are *Bull* (1971); *Giovinetto and Bentley* (1985) and *Giovinetto and Zwally* (2000). A more objective method for extrapolation is to use satellite data. Although satellites can not measure SMB directly, the observed brightness temperature provides a dimensionless background field for interpolation. *Vaughan et al.* (1999) used this method to assess the SMB of Antarctica, and for some time his estimate became the reference SMB field. Recently, *Arthern et al.* (2006) updated this SMB estimate with an improved interpolation technique. Brightness temperature can only be considered as proxy of the SMB in dry snow areas (*Zwally and Giovinetto*, 1995; *Arthern et al.*, 2006). Hence, extrapolation to the warmer coastal areas may lead to inaccurate estimates, since the snow cover in the coastal zone may experience melt, as visible in Figure 1.7b.

Alternatively, the Antarctic SMB can be estimated with GCM's and RCM's. Figure 1.7c, from *Van Lipzig et al.* (2002b), is an example of a recent model-based SMB estimate; further examples are *Genthon and Krinner* (2001) and *Bromwich et al.* (2004). A strong aspect of GCM's and RCM's is their complete coverage of Antarctica. SMB estimates are therefore spatially and physically consistent. Furthermore, RCM's can be evaluated on high spatial resolution. However, since the snow accumulation is a result of cloud processes, sublimation and snow melt, accurate parameterization of these processes is critical for the reliability of the final SMB estimate. Parameterizations attempt to quantify complex processes in terms of resolved model variables, e.g. temperature and humidity. Evaluation of model results using in situ observations is thus indispensable to assess the quality of model estimated SMB. Because a thorough evaluation has been lacking, modeled SMB has long been regarded as to be of insufficient quality to improve estimates of Antarctic SMB.

1.5 Contents of this thesis

In this thesis, the regional atmospheric climate model RACMO2/ANT has been used to simulate the weather over Antarctica from September 1957 until the end of 2004. The performance of RACMO2/ANT is critically assessed and model results are presented and discussed. We focus on two aspects of Antarctic climate, the surface mass balance and the ABL heat budget.

Chapters 2, 3 and 4 deal with the SMB of Antarctica. In Chapter 2, the spatial distribution of solid precipitation, sublimation/deposition and melt is outlined. Furthermore, the inter-annual and seasonal variability is discussed. In Chapter 3, the model simulated SMB is evaluated. Model simulated SMB correlates well with observations, although RACMO2-/ANT tends to overestimate the coast-to-interior SMB gradient. The good correlation allowed us to re-calibrate the model simulated SMB, providing a new estimate of the present-day Antarctic SMB. The main difference with previous compilations is a higher SMB in coastal Antarctica, in particular in coastal Marie Byrd Land. In Chapter 4, a method is presented to evaluate basin-wide uncertainties in calibrated model SMB.

Chapters 5 and 6 describe the atmospheric heat budget over Antarctica that is derived from RACMO2/ANT output. These more fundamental studies are motivated by our incomplete knowledge of the processes that determine temperature and temperature change in Antarctica. The atmospheric heat budget quantifies the contributions from all physical processes to temperature evolution. Knowing the relative importance of these processes, the dependence

of Antarctic temperature on natural variability and anthropogenic forcings can be evaluated more effectively.

The atmospheric heat budget evidently has horizontal and vertical structure. Chapter 5 concentrates on the vertical distribution. Vertical profiles of the heat budget are grouped as a function of surface elevation. Only profiles of East Antarctica are used, since this part of Antarctica has a relatively uniform topography. Chapter 6 investigates spatial patterns in the heat budget in the lowest part of the atmosphere, the ABL. An intriguing result is the clear connection between topography and near-surface temperature field.

In the final chapter, suggestions for further research are given with respect to model development and analysis of model output. Furthermore, we suggest additional observations that are needed for a more stringent model evaluation in the future.

Chapter 2

Characteristics of the Antarctic surface mass balance

Abstract

Temporal and spatial characteristics of the present-day Antarctic surface mass balance (SMB) are presented, including its components solid precipitation, sublimation/deposition and melt. For this purpose, we use output of a regional atmospheric climate model (RACMO2/ANT, horizontal resolution of ~ 55 km) for the period 1958-2002. RACMO2/ANT uses European Centre for Medium-Range Weather Forecasts (ECMWF) 40 year re-analysis (ERA-40) fields as forcing at the lateral boundaries. RACMO2/ANT underestimates SMB in the high interior of East and West Antarctica and overestimates the SMB on the steep coastal slopes. Otherwise, the modeled spatial pattern of SMB is in good qualitative agreement with recent compilations of in situ observations. Large-scale patterns, like the precipitation shadow effect of the Antarctic Peninsula, are well reproduced, and mesoscale SMB patterns, such as the strong precipitation gradients on Law Dome, are well represented in the model. The integrated SMB over the grounded ice sheet is $153 \text{ mm w.e. year}^{-1}$ for the period 1958-2002, which agrees within 5% with the latest measurement compilations. Sublimation and melt remove 7% and $<1\%$ respectively of the solid precipitation. We found significant seasonality of solid precipitation, with a maximum in autumn and a minimum in summer. No meaningful trend was identified for the SMB, because the time series of solid precipitation and SMB are affected by an inhomogeneity in 1980 within the ERA-40 fields that drive RACMO2/ANT. Sublimation, melt and liquid precipitation increase in time, which is related to a modeled increase in 2 m temperature.

2.1 Introduction

In recent decades, compilations of the surface mass balance of the Antarctic ice sheet have improved in quality (Vaughan *et al.*, 1999; Giovinetto and Zwally, 2000), but they are still compromised by data sparsity (Genthon and Krinner, 2001). At the same time, the quality of

This chapter has been published as: Van de Berg, W. J., van den Broeke, M. R., Reijmer, C. H., and van Meijgaard, E. (2005), Characteristics of the Antarctic surface mass balance (1958-2002) using a regional atmospheric climate model, *Annals of Glaciology*, 41, 97–104.

global atmospheric models has improved significantly: horizontal and vertical resolution have increased because of increased computer power, and parameterizations of physical processes like precipitation, turbulent and radiative budgets produce more accurate results. Another advance has been the assimilation of measurements into the models. The European Centre for Medium-Range Weather Forecasts (ECMWF) recently completed a 40 year re-analysis project (ERA-40), in which all these improvements are cumulated. ERA-40 aims to give the best and most consistent analysis possible of the global weather during the period September 1957-August 2002.

Over Antarctica, ERA-40 nevertheless shows biases (*Genthon, 2002; Reijmer et al., 2005*). The surface temperature is overestimated by typically 3 K, mainly because snow albedo is too low. Katabatic winds over the ice-sheet slopes are underestimated because of limited model resolution (120 km) resulting in flattened model topography and too high effective surface roughness lengths. Finally, ERA-40 underestimates accumulation in the interior of Antarctica, a common problem with numerical models (*Genthon and Krinner, 2001; Van Lipzig et al., 2002b*).

Compared to a global climate model, a regional atmospheric climate model, forced at the lateral boundaries with output from a general circulation model (GCM) or a reanalysis, is expected to generate a better climatology for Antarctica, primarily because much higher resolutions are feasible and parameterizations can be adapted to the specific Antarctic situation. The added value of such an approach was shown by, for example, *Van Lipzig and van den Broeke (2002); Van den Broeke and van Lipzig (2003)*, who presented results of a regional atmospheric climate model, run over Antarctica (RACMO1/ANT). This run used the 15 year re-analysis data of ERA-15 as lateral boundary forcing.

Here, we present results of an integration with a new model (RACMO2/ANT), which was driven at the lateral boundaries by output from ERA-40, with a focus on the surface mass balance. The specific, i.e. valid for one location and a certain time period, surface mass balance (SMB) is defined as the sum of all mass fluxes towards the surface, integrated over a year:

$$SMB = \int_{\text{year}} dt (P_s + SU + M + ER_{ds} + SU_{ds}), \quad (2.1)$$

where P_s is solid precipitation, SU is sublimation, M is melt, ER_{ds} is erosion as a result of divergence in the horizontal snowdrift transport, and SU_{ds} is sublimation of drifting-snow particles. Since SMB varies in time, the estimates presented here are valid for time period of investigation. All values are expressed in mm water equivalent (w.e.) year^{-1} , and contributions are positive when directed towards the surface. Note that SU , M , ER_{ds} and SU_{ds} have negative values in Equation (2.1), because they remove mass from the surface. Snowdrift processes are not included in RACMO2/ANT, so ER_{ds} and SU_{ds} are not considered in this study. In Antarctica, most (melt)water will refreeze at some depth in the snow-pack, where temperatures are still below freezing. As this process ('internal accumulation') is not incorporated in RACMO2/ANT physics, it is not considered further either.

After a short model description in section 2.2, we present results in section 2.3, starting with the spatial distribution of the annual mean mass balance components: solid precipitation, sublimation and melt. The modelled SMB is compared with a compilation of measurements by *Vaughan et al. (1999)*. Next, we discuss the seasonality of the various SMB components,

averaged for the grounded ice sheet. Also in section 2.3, time series of ice sheet integrated SMB are compared with those derived from ERA-40. Section 2.4 discusses some possible shortcomings of model and observations and a summary is given in section 2.5.

2.2 Model description

RACMO2/ANT uses the atmospheric dynamics of the High Resolution Limited Area Model (HIRLAM, version 5.0.6, *Undén et al. (2002)*), which uses a semi-Lagrangian discretization scheme. The description of physical processes is equal to that of the ECMWF atmospheric model used in the ERA-40 reanalysis (cycle CY23R4, *White (2001)*). RACMO2/ANT differs fundamentally from RACMO1/ANT which was used by *Van Lipzig et al. (2002b)*. RACMO1/ANT uses the dynamics of an older version of HIRLAM which had an Eulerian discretization scheme and ECHAM4 physics.

The horizontal resolution of RACMO2/ANT is ~ 55 km. The model has 40 hybrid levels in the vertical, of which the lowest is at ~ 10 m above the surface. Hybrid levels follow the topography close to the surface and pressure levels at higher altitudes. ERA-40 fields force the model at the lateral boundaries, while the interior of the domain is allowed to evolve freely. The model integration over 2002 is completed using ECMWF operational analysis. Sea surface temperature and the sea ice mask are prescribed from ERA-40. If sea ice is prescribed, a sea ice thickness of 1.5 m is assumed. The model treats ice shelves as grounded ice. *Reijmer et al. (2005)* present a more detailed description of RACMO2/ANT and the associated improvements compared to ERA-40. Below, we restrict ourselves to a summary of the most important model adjustments that were made to better represent Antarctic conditions, and the post-process correction applied to the liquid and solid precipitation.

2.2.1 Snow albedo

The ECMWF description of snow albedo uses the method described by *Douville et al. (1995)*, in which the snow albedo decreases linearly from 0.85 immediately, after an accumulation event, to 0.75 in 12.5 days for temperatures below freezing. The method underestimates snow albedo in Antarctica, where temperatures are well below zero and the albedo changes very slowly.

The snow albedo scheme of *Van den Hurk and Viterbo (2003)* was therefore implemented in RACMO2/ANT. This method accounts for temperature effect on albedo changes and assumes a negligible decrease of albedo when temperatures are below -10 °C. Furthermore, we increased the lower limit of albedo to 0.80 and lowered the threshold value of a snow event affecting the albedo to 0.3 mm/hr. In the original formulation, the sea ice albedo consisted of a climatological value with a fixed seasonal cycle. In the formulation of RACMO2/ANT, the sea ice albedo was calculated using the snow albedo scheme, but the minimum albedo for sea ice was set to 0.6.

2.2.2 Surface roughness lengths

The surface roughness length for momentum (z_0) was initially calculated with the method described by *White* (2001). This method, however, leads to an overestimation of the roughness length in Antarctica, with values up to 100 m. Therefore, z_0 was scaled down to a basic value of 10^{-3} m for the ice sheet and allowed to increase to up to 1 m for mountainous areas like the Trans Antarctic Mountains, to account for sub-grid orography. The ECMWF physics uses the method of *White* (2001) for the calculation of the roughness lengths for heat and moisture (z_h, z_q). We replaced this by *Andreas's* (1987) theoretical model, which was developed especially for snow and ice surfaces. The model expresses z_h as a function of z_0 and the surface friction velocity u_* . Typical new values of z_h are 3×10^{-4} m for the quiet upper parts of the interior decreasing to 6×10^{-6} m for the mountain regions. We assume z_q to be equal to z_h .

2.2.3 Snow model

The original ECMWF physics treats the surface of the ice sheets as a seasonal snow cover, i.e. as a single snow layer of 10 m w.e. thickness on top of soil, while all calculations of snow temperature use a snow layer of 1 m w.e. thickness. An infinitely thin skin layer is used to derive surface energy fluxes and surface temperature.

In RACMO2/ANT, a four layer snow model was added between the snow layer already present and the soil. The thickness of the snow layers is fixed and increases with depth from 0.1 to 6 m. Daily and seasonal variations of snow temperature are better represented with this model. The representation of melt and runoff was not changed. Meltwater is assumed to run off immediately, and not to refreeze in the deeper snow layers. Due to the low temperatures in Antarctica, melt seldom occurs in the interior, but occurs quite frequently in the coastal zone (*Schneider and Steig, 2002*).

2.2.4 Correction of the liquid and solid precipitation

It was found that RACMO2/ANT overestimates the liquid precipitation over Antarctica at the expense of solid precipitation, because of an inadequate parameterization of precipitation formation in mixed-phase clouds at temperatures between -20 and 0 °C. In this temperature range, the parameterization utilized in the ECMWF physics (*White, 2001*) assumes a direct conversion of cloud water and cloud ice into liquid and solid precipitation, respectively. However, if cloud ice exists at the level where precipitation is formed, the precipitation will develop as solid only (*Rogers and Yau, 1989*). We have corrected the liquid and solid precipitation output of RACMO2/ANT by analyzing the daily vertical profiles of temperature and precipitative fluxes, assuming that the precipitation develops as solid if the vertical layers, in which the precipitation is formed, are partly colder than -10 °C, leaving the total precipitation sum unchanged.

2.3 Results

In this section, we discuss the spatial and temporal variability of the modeled SMB components over Antarctica. Figure 2.1 shows a map of Antarctic topography and the topographical features mentioned in the text.

2.3.1 Solid precipitation

Figure 2.2 shows the corrected annual mean solid precipitation (P_s), averaged for 19582002. The Antarctic interior is dry, and the coastal slopes, in particular of Marie Byrd Land and the Antarctic Peninsula, receive most precipitation. Note the very strong upwind/downwind effects on (P_s) in coastal East Antarctica, where topographic promontories block the circumpolar easterlies. The spatial pattern of (P_s) over Law Dome is shown as an example in the inset. The model grid (the crosses in the inset of Figure 2.2) greatly simplifies the P_s pattern over Law Dome. Nevertheless, the modeled upwind/downwind effect is a realistic phenomenon, considering the observed strong eastwest accumulation gradients on Law Dome (*Van Ommen et al.*, 2004). Strong precipitation shadow effects are also visible east of the Antarctic Peninsula and over the Ross Ice Shelf.

After the correction described in section 2.2.4, the frequency of rain events (not shown) agrees with the sparse information available (*King and Turner*, 1997; *Turner et al.*, 1995). Only the coasts receive some rain, but less than 10 mm per year except for the Antarctic Peninsula. Towards the northern edge of the Antarctic Peninsula, the amount of rain quickly increases to 100 mm per year, which is still a small amount compared to the solid precipitation (Figure 2.2).

2.3.2 Sublimation

Sublimation is largely controlled by temperature, which depends strongly on elevation, and regionally by the katabatic wind. The largest values of absolute net sublimation (not shown) are found in Dronning Maud Land and the Transantarctic Mountains, with values up to 200 mm w.e. per year. Net deposition is largest on the West Antarctica plateau, where it reaches values up to 25 mm w.e. per year. The sublimation on the slopes of Antarctica is similar to earlier model-based estimates (*Van den Broeke*, 1997, and references therein), but the interior deposition seems to be slightly overestimated locally when compared to calculations based on automatic weather station (AWS) observations (*Van den Broeke et al.*, 2004b).

The sublimation as a fraction of the solid precipitation (SU/P_s) is shown in Figure 2.3b. The areas where sublimation exceeds solid precipitation, in Dronning Maud Land, the Lambert Glacier valley and at the foot of the Transantarctic Mountains, are drawn grey. These areas could be sensitive to blue-ice formation (see section 2.3.4). Over large parts of the dry East Antarctic plateau, deposition constitutes about 10% of the amount of solid precipitation, although the absolute amount is less than 3 mm w.e. per year.

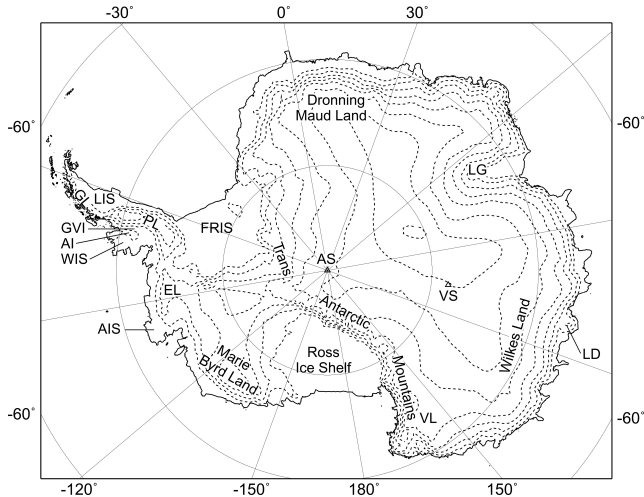


Figure 2.1: Map of Antarctica with elevation contours at 500m intervals. Locations marked are the Larsen Ice Shelf (LIS), Palmer Land (PL), Graham Land (GL), George VI Ice Shelf (GVI), Alexander Island (AI), Wilkins Ice Shelf (WIS), FilchnerRonne Ice Shelf (FRIS), Ellsworth Land (EL), Abbot Ice Shelf (AIS), Lambert Glacier (LG), Law Dome (LD), Victoria Land (VL), AmundsenScott Station (AS) and Vostok station (VS).

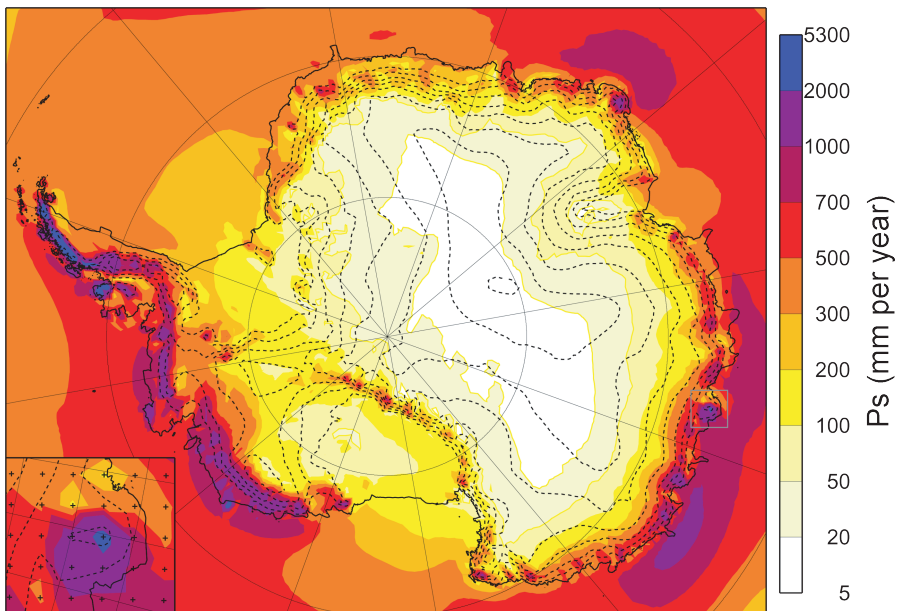


Figure 2.2: Modeled annual solid precipitation (P_s) averaged for the period 1958-2002. The inset shows an enlargement of the pattern over Law Dome (gray square). Crosses in this inset mark the location of the model grid points. The unit is mm w.e. per year

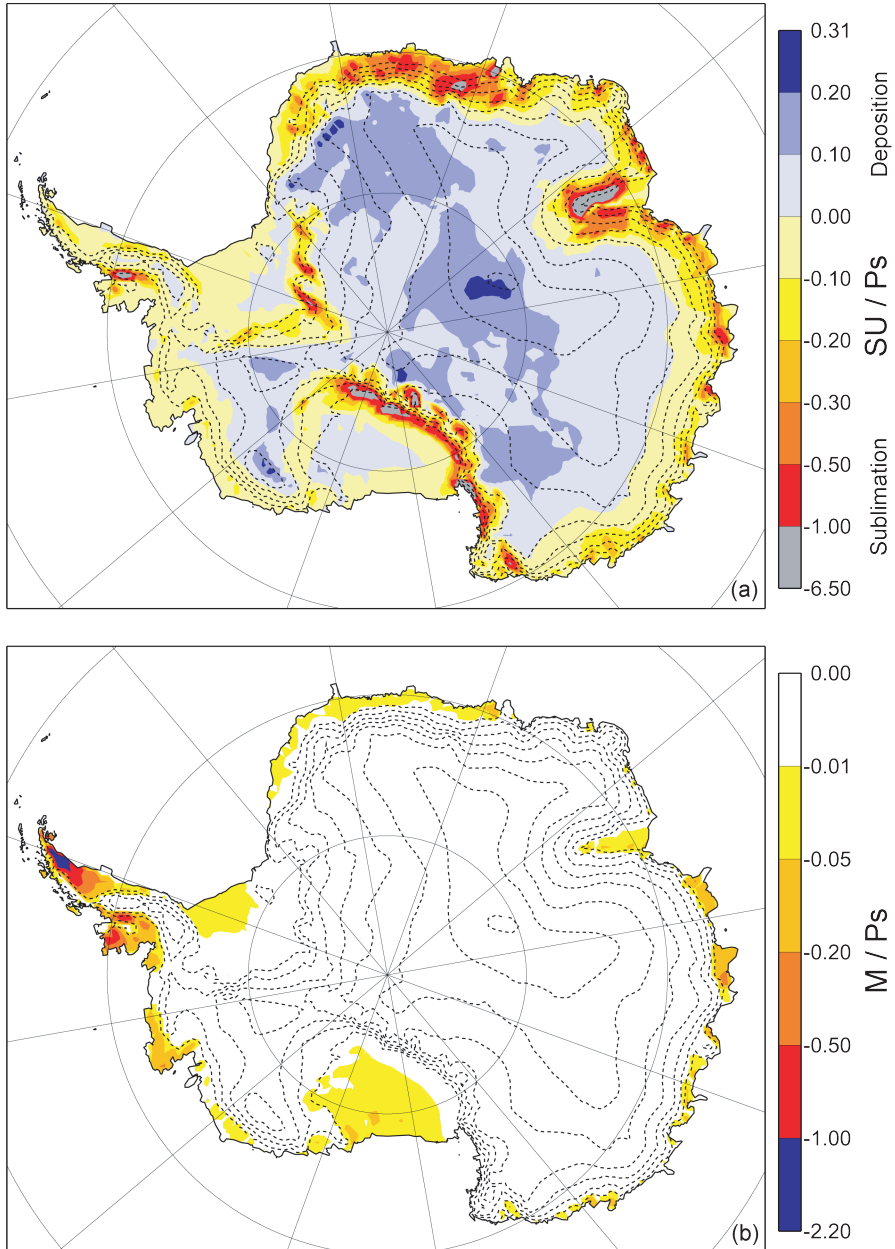


Figure 2.3: Annual averages (1958-2002) of (a) modeled sublimation/deposition, (b) melt flux, both expressed as a fraction of the solid precipitation, i.e. SU/P_s and M/P_s , respectively. Values below -1 (grey areas) indicate that sublimation or melt exceeds precipitation.

2.3.3 Melt

Annual surface melt is shown as a fraction of the solid precipitation in Figure 2.3b. As can be seen, all ice shelves experience melting. Large melt fractions of more than 50% are found on the western side of the Antarctic Peninsula (the Wilkins and George VI Ice Shelves), and up to 25% on the Abbot Ice Shelf, West Antarctica. Melt exceeds solid precipitation on the former Larsen A and B ice shelves on the eastern side of the Antarctic Peninsula. The absolute annual melt flux (not shown) reaches a maximum of 0.5 m w.e. per year at the northern edge of the Larsen Ice Shelf. The value for this location is probably an underestimation, since the lower limit of the albedo was set at 0.8. A much lower albedo is likely for large melt events. For example, meltwater ponds have been observed over the Larsen A and B ice shelves and Wilkins Ice Shelf during summer months (*Scambos et al.*, 2000), and melt ponds significantly reduce the surface albedo. The modeled strong melt cannot be compared to observations since the surface mass balance has not been measured on the northern part of the Larsen Ice Shelf. The largest melt is nevertheless expected at sea level on the western side of the Antarctic Peninsula, where temperatures are significantly higher than on the eastern side. However, at the employed resolution of 55 km the model does not contain continental gridpoints with an elevation less than 200 m in this area, so this maximum is not well represented.

2.3.4 Surface mass balance (SMB)

Figure 2.4a shows the SMB, i.e. the sum of solid precipitation, sublimation/deposition and melt, as modeled in RACMO2/ANT. As expected, the SMB largely reflects the distribution of solid precipitation (Figure 2.2), but sublimation and melt do have important regional impacts. For instance, sublimation removes an important part of the precipitated snow in Dronning Maud Land, over the Lambert Glacier basin and at the foot of the Transantarctic Mountains, leading locally to areas with a negative SMB (grey areas in Figure 2.4a). Note that a negative SMB only occurs in areas with high sublimation together with low solid precipitation.

For comparison, the absolute differences between the modeled SMB and the SMB compilation of *Vaughan et al.* (1999), based on in situ measurements, are shown in Figure 2.4b. Although many deviations are visible, overall the two fields are in good qualitative agreement. Areas with known higher accumulation compared to other coastal zones, i.e. the western part of the Antarctic Peninsula and Ellsworth Land, also have higher accumulation in the modeled SMB. The extent of the dry interior, where accumulation is typically less than 100 mm, is reproduced well. Areas with a negative SMB in RACMO2/ANT compare well in distribution and extent with reported blue-ice areas (*Winther et al.*, 2001), though RACMO2/ANT predicts blue-ice areas in Dronning Maud Land and at the foot of the Transantarctic Mountains at somewhat lower elevations than reported.

However, systematic differences are also noticed. The SMB in the interior in the *Vaughan et al.* (1999) compilation exceeds the modeled SMB by about 30 mm w.e. per year, about a factor of 2. Modeled SMBs over the coastal slopes are systematically greater than those reported by *Vaughan et al.* (1999). Especially remarkable is the large modeled SMB on the Marie Byrd Land coast, which is much greater than compiled values in Figure 2.4b.

The resemblance between modeled and observed SMB in the Antarctic Peninsula (as compiled by *Turner et al.* (2002); not shown) is very strong. The spatial pattern and absolute

Table 2.1: Integrated SMB (mm w.e. per year) from RACMO2/ANT compared to several compilations.

	Period	SMB		
		Grounded ice sheet	Antarctica	Antarctica*
RACMO2/ANT	1958-2002	153	165	154
RACMO2/ANT	1958-1979	139	152	141
RACMO2/ANT	1980-2002	166	178	166
<i>Vaughan et al.</i> (1999)	variable	149	166	
<i>Giovinetto and Zwally</i> (2000)	variable			149 ± 14
<i>Van Lipzig et al.</i> (2002b)	1979-1993	156		
<i>Krinner et al.</i> (1997)	5 years		162	
<i>Bromwich et al.</i> (2004)	7/96-6/99		186 ± 16	

* Except Graham Land, the former Larsen Ice Shelf and eastern Palmer Land.

values agree. The negative SMB modeled on the Larsen and Wilkins Ice Shelves is caused by a combination of low solid precipitation (Figure 2.3.1), due to the rain-shadow effect of the Antarctic Peninsula for the Larsen Ice Shelf and of Alexander Island for the Wilkins Ice Shelf, and large melting values (Figure 2.3b). It is well known that ice shelves in these regions have shown significant retreat in recent decades, which has so far been primarily ascribed to an increase in melt (*Vaughan and Doake, 1996; Scambos et al., 2000*).

The SMB as modeled by RACMO2/ANT is better in several respects than the results of RACMO1/ANT (*Van Lipzig et al. (2002b, Figure 6b)*). The spatial resolution has increased, because smoothing of the model fields is no longer required due to the improved discretization scheme. Sublimation has decreased to more realistic values, due to improved estimates of the surface roughness lengths, and melt has been added. However, underestimation of the SMB over the interior has increased, and much higher SMBs are modeled in the coastal zone, which is not necessarily an improvement.

Using the grounding-line definitions of *Vaughan et al. (1999)*, 45 year means of modeled solid precipitation, sublimation, melt and rain, averaged over the grounded ice sheet, are 164, -11, -1 and <1 mm w.e. per year, respectively. The modeled SMB over the grounded ice sheet is 153 mm w.e. per year. When the ice shelves and ice rises are included, the SMB increases to 165 mm w.e. per year. When all meltwater and liquid precipitation is added, the values increase by 1.5 and 4 mm w.e. per year, respectively.

Table 2.1 shows that the modeled SMB, averaged over 1958-2002, compares well with estimates based on measurements by *Vaughan et al. (1999)* and *Giovinetto and Zwally (2000)*. The modeled SMB for the satellite era only, beginning in 1980, is somewhat higher than the latter estimates. The RACMO2/ANT modeled SMB also compares well with model results of *Krinner et al. (1997)* and *Van Lipzig et al. (2002b)*, but note the different time periods. The model results of *Bromwich et al. (2004)* are slightly higher (Table 2.1).

2.3.5 Seasonality of the mass balance

Figure 2.5 shows the modeled seasonality (1958-2002 average) of the various SMB components. All components of the SMB show a seasonality that exceeds the uncertainty due

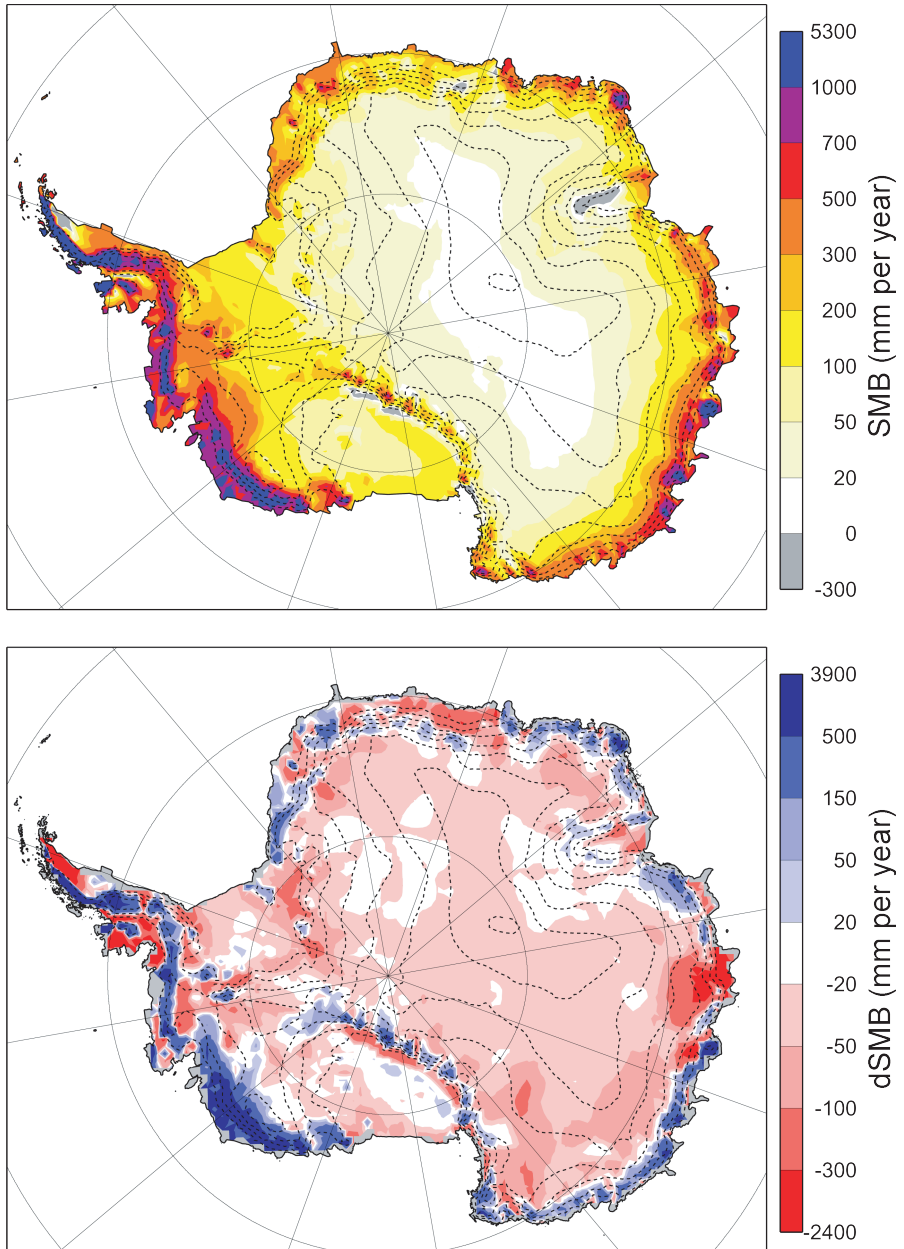


Figure 2.4: (a) Modeled SMB (mm w.e. per year), averaged for the period 1958-2002. (b) Difference map with the compilation of the surface mass balance (mm w.e. per year), based on in situ observations (Vaughan et al., 1999). Positive values imply that the modeled SMB exceeds the compilation. Gridpoints for which the compilation is not determined are drawn grey.

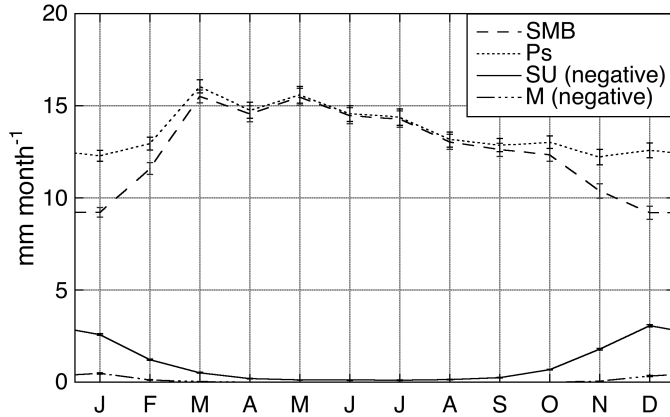


Figure 2.5: Modeled seasonality of the SMB and its components over the grounded ice sheet (1958-2002). P_s , SU and M denote solid precipitation, sublimation and melt, respectively. Error bars denote the uncertainty due to year-to-year variability.

to year-to-year variability. Solid precipitation (P_s) is smallest during summer, and peaks in autumn. A similar pattern was found by *Van Lipzig et al.* (2002b), but in that study the amplitude was not significant, as a result of the shorter period. Sublimation (SU) and melt (M) peak during summer and nearly vanish in the other months. In the summer months December and January, sublimation becomes a significant sink term in the SMB, removing 25 to 30% of the solid precipitation from the surface. Averaged over the year and across the grounded ice sheet, sublimation removes 7% of solid precipitation. This is less than *Van den Broeke* (1997) GCM-based estimate of 10 to 15%, but compares well with sublimation calculations from AWSs (*Van den Broeke et al.*, 2004b).

Figure 2.6 shows the seasonality of the solid precipitation per region. The solid precipitation is shown, instead of the SMB, to avoid a bias associated with sublimation and melt, both summer phenomena. The Filchner-Ronne Ice Shelf and large coastal areas have dry summers (horizontal red lines). Solid precipitation is largest during autumn over large parts of Antarctica. Wilkes Land, however, receives most solid precipitation during winter. This figure compares well with the results of *Genthon et al.* (1998) and *Van Lipzig et al.* (2002b). The solid precipitation minima and maxima over the ocean are a result of the seasonal cycle of temperature and the associated solid fraction of the precipitation, i.e. less snowfall in summer and more in winter.

2.3.6 Interannual variability and trends

Figure 2.7 shows year-to-year variations in the various terms of the SMB integrated over the grounded ice sheet. We also included the SMB of ERA-40, calculated by including rain and neglecting melt. We had to do so to obtain realistic values, because in ERA-40 rain is strongly overestimated and melt is unrealistically large probably due to underestimated snow albedo. In an absolute sense, all components show an increase in time (Table 2.2). Nevertheless,

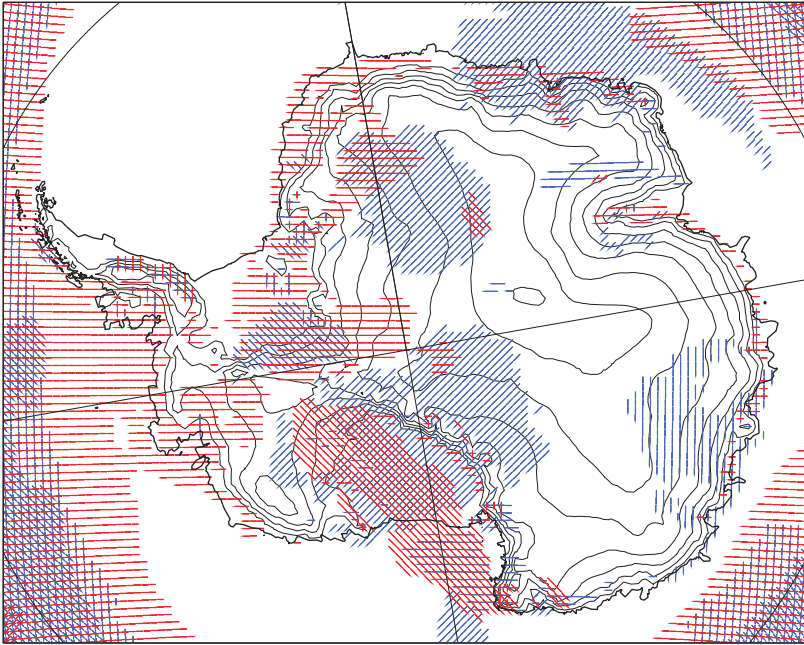


Figure 2.6: Seasonality of solid precipitation (1958-2002). Blue lines mark areas in which a season is 33% wetter than the annual mean; red lines mark 33% dryer than the annual mean. Deviations were derived by comparing mean daily solid precipitation. Hatching denotes seasons as follows: — summer; / autumn; | winter; \ spring.

the time series of solid precipitation and SMB show an inhomogeneity around 1980, which is most pronounced in the ERA-40 SMB. For all time series, the method of *Easterling and Peterson* (1995) was used to trace inhomogeneities. Linear trends in the solid precipitation and SMB over the split periods (pre- and post-1980) are not significant.

The time series of sublimation, melt and rain (P_l) do not show an inhomogeneity around 1980. Sublimation, melt and liquid precipitation are controlled most by near-surface meteorological conditions, unlike solid precipitation, which is strongly dependent on the large-scale circulation. Near-surface conditions are less sensitive to changes in general circulation forcing from ERA-40 at the lateral boundaries than the large-scale circulation itself. Therefore, an absence of an inhomogeneity is possible. Linear trend fits to the data are summarized in Table 2.2. The trends in sublimation, melt and liquid precipitation for the period 1958-2002 are much larger than the uncertainty due to interannual variability. Note, however, that 2 m temperature trends are overestimated in RACMO2/ANT. Trend analysis on the split periods gives similar values, except for the sublimation. Sublimation seems to be affected by multi-annual variations, which erase the possible trend if the split time series are considered.

Figure 2.7 shows that the solid precipitation varies strongly from year to year. The regional variability (not shown) is even larger. The standard deviation of P_s reaches up to 50%

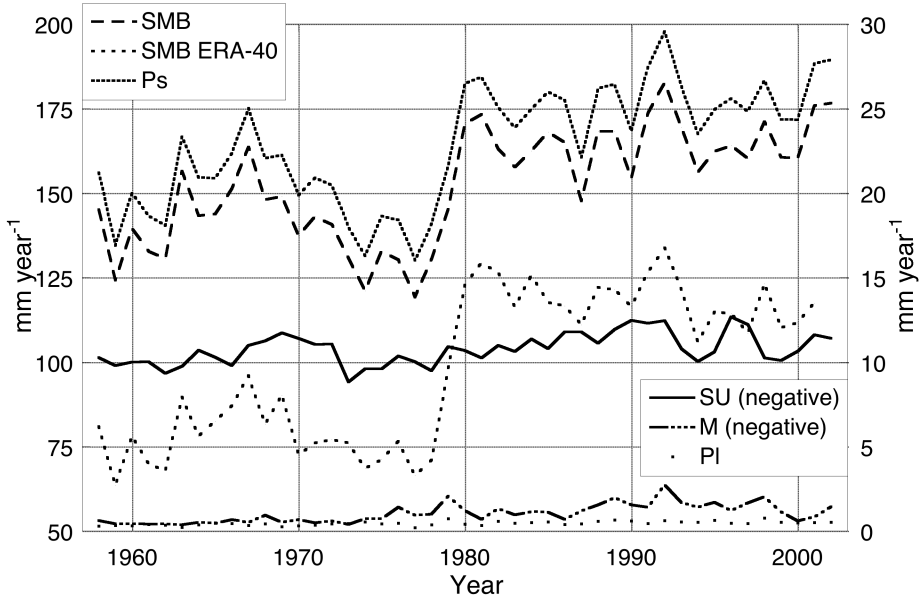


Figure 2.7: Time series of the SMB components, averaged for the grounded ice sheet as found by RACMO2/ANT. The left axis displays the values of SMB, the SMB determined by ERA-40 and solid precipitation (P_s); the right axis the values for the sublimation (SU) and melt (M).

Table 2.2: Results of linear trend analysis of SMB components averaged over the grounded ice sheet. The method described by Easterling and Peterson (1995) was used to determine the position of the inhomogeneity in the P_s time series. Mean values are in mm w.e. per year and trends in mm w.e. year^{-2} . Error margins in trends are one standard deviation.

RACMO2/ANT	1958-2002		1958-1979		1980-2002	
	mean	trend	mean	trend	mean	trend
SMB	153	-	139	-0.49 ± 0.40	166	0.15 ± 0.28
P_s	164	-	150	-0.45 ± 0.39	178	0.17 ± 0.27
SU	-10.8	-0.035 ± 0.010				
M	-1.0	-0.029 ± 0.005				
P_i	0.5	0.006 ± 0.001				

ERA-40	1958-2001		1958-1979		1980-2001	
	mean	trend	mean	trend	mean	trend
SMB	98	-	78	0.03 ± 0.32	119	-0.50 ± 0.22
P	120	-	97	0.18 ± 0.34	142	-0.42 ± 0.24

of the annual sum in Victoria Land, Lambert Glacier, the inland part of Marie Byrd Land and the southern and eastern parts of the Filchner-Ronne Ice Shelf.

2.4 Discussion

2.4.1 Spatial distribution of measured and modeled SMB

Compared with a recent compilation of Antarctic SMB, RACMO2/ANT appears to underestimate accumulation on the plateau of East and West Antarctica and to overestimate accumulation on the steep coastal slopes. For instance, modeled accumulation on the slopes of Marie Byrd Land is twice the values presented by *Vaughan et al.* (1999).

The high modeled accumulation over the ice-sheet slopes may have been caused by artificial diffusion of moisture along model levels. This diffusion, implemented to stabilize the model, generates an artificial uphill moisture transport. Diffusion-enhanced moisture transport is a common problem with atmospheric models in regions of steep topography (see *Connolley and King*, 1996; *Van Lipzig and van den Broeke*, 2002; *Lenderink et al.*, 2003). A 1 month test with the horizontal diffusion of moisture switched off shows an accumulation reduction of about 10% on the steepest slopes (not shown). This modest change casts doubt on the assumption that horizontal diffusion is the culprit.

Other reasons for the differences between modeled and compiled SMB could be snowdrift transport and snowdrift sublimation, which are not included in RACMO2/ANT. Snowdrift sublimation and erosion is strongest in areas with the strongest wind, which is closely related to the topographic slope. RACMO2/ANT especially seems to overestimate solid precipitation in regions with a large surface slope; therefore including snowdrift-associated processes might bring the model results closer to the observations.

The modeled SMB is more than twice that presented by *Vaughan et al.* (1999) on the slopes of Marie Byrd Land, but compares well with results of other models in this region, e.g. RACMO/ANT1 (*Van Lipzig et al.*, 2002a), other GCMs and ERA-15 (*Genthon and Krinner*, 2001). Such a common bias may be caused by neglecting snowdrift, but it is difficult to explain why snowdrift would strongly affect the accumulation on the slopes of Marie Byrd Land only. Therefore, the sparsity of measurements in this region could also be partly responsible for the difference.

The underestimation of SMB on the Antarctic Plateau appears to be a shortcoming of many numerical atmospheric models (see *Genthon and Krinner*, 2001; *Van Lipzig et al.*, 2002b). One reason could be the neglect of diamond dust, the physical mechanism of which is yet not fully understood. Diamond dust can constitute a substantial component of the SMB in the Antarctic interior, e.g. up to 75% at Vostok (*Ekaykin*, 2003). The artificial diffusion of moisture is not the source for the possible underestimation of the SMB in the interior. The test without horizontal diffusion showed no significant increase of SMB in this part of Antarctica.

The sparsity and temporal inhomogeneity of accumulation measurements could also partly explain the differences. The reliability of observation compilations depends strongly on the quality of the interpolation, in particular over the coastal slopes where accumulation gradients are large. Furthermore, the observations have not been corrected to cover a com-

mon time period. A detailed evaluation of the differences between measured and modeled SMB will be made in Chapter 3.

2.4.2 The integrated SMB

The problems listed above also affect the integrated SMB values, but because they partly compensate, the differences between integrated values are small (Table 2.1). The divergence in wind-driven transport of snow is assumed to be an order of magnitude or more smaller than the other moisture fluxes in the Antarctic SMB (*Déry and Yau, 2002*). The contribution of diamond dust to the SMB is probably significant in the very dry interior, but decreases when the integrated SMB is considered. Refreezing of liquid precipitation adds an uncertainty of only 1 mm w.e. per year. The long integration period reduces the uncertainty in the mean SMB due to year-to-year variability to ~ 3 mm w.e. per year. Finally, the temporal inhomogeneity in the SMB adds uncertainty to the time-integrated sums. Since ERA-40 might be of lesser quality before 1980, the inhomogeneity observed for 1980 might indicate that the modeled SMB before 1980 is slightly underestimated. Despite these uncertainties, the integrated SMB compares well with measurement estimates.

2.4.3 Interannual variability and trends

Contrary to what was argued by *Bromwich (1988)*, we found a relatively large year-to-year variation of the Antarctic SMB. A significant inhomogeneity was found in the time series of solid precipitation and SMB of RACMO2/ANT, which is even larger in ERA-40. This inhomogeneity nearly coincides with the start of the data assimilation of modern satellite measurements (e.g. TIROS Operational Vertical Sounder) into the re-analysis in 1979 (see www.ecmwf.int). The increase in SMB is probably mainly caused by this inhomogeneity in input data. Any trend analysis of the time series of solid precipitation and SMB would therefore require an accurate estimate of the magnitude of the SMB inhomogeneity.

The linear trends of the sublimation (SU) and melt (M) for 1958-2002 in Table 2.2 are significant up to 99%. We found no indication that these time series were affected by inhomogeneities, but the integrated sublimation correlates well with the averaged 2 m temperature ($r = 0.69$, detrended). A smooth, continent-wide increasing trend in 2 m temperature is modeled by RACMO2/ANT. The temperature records of Admundsen-Scott and Vostok stations and the satellite observations from 1979 to 1998 (*Comiso, 2000*) show a cooling trend. The modeled temperature and sublimation trends are likely erroneous. Satellite observations of melt suggest a decreasing trend averaged over Antarctica (*Torinesi et al., 2003*). A strong increase in rain is observed on the Antarctic Peninsula (*Turner et al., 1997*). It is too early to draw a final conclusion about uncertainty trends based on model results.

2.5 Conclusions

We present characteristics of the SMB of Antarctica, using a regional atmospheric climate model (RACMO2/ANT), driven at the lateral boundaries by ERA-40 data. This model has a favorable combination of high horizontal (~ 55 km) and vertical resolution (40 layers) and

a long integration period (1958-2002). The modeled Antarctic SMB, integrated over the grounded ice sheet, agrees well with earlier estimates from models and observations. The modeled spatial SMB distribution is in good qualitative agreement with the most recent measurement compilations. However, the model seems to underestimate the SMB in the interior of Antarctica, whereas it overestimates the SMB on steep coastal slopes. The reasons for this are unclear. The effect of artificial moisture diffusion appears to be small. Other possible reasons are the neglect of snowdrift transport, snowdrift sublimation and diamond dust in RACMO2/ANT. However, the sparsity and temporal mismatch of accumulation observations and shortcomings in the interpolation procedure should not be ruled out.

The integrated solid precipitation peaks in autumn, but the seasonality of the solid precipitation differs regionally. Sublimation and melt are only significant in summer. Where modeled sublimation exceeds solid precipitation, we find blue-ice areas or dry valleys in qualitative agreement with their present position. Melt only affects ice shelves, especially the former Larsen A and B ice shelves in the northern Antarctic Peninsula: here, melt exceeds solid precipitation and causes the SMB to become significantly negative.

The modeled time series of SMB and solid precipitation are dominated by an inhomogeneity in 1980, which is even more prominent in the ERA-40 record. Given that the inhomogeneity coincides with the start of extensive satellite data assimilation into ERA-40, we suspect that this increase is of numerical origin, rather than a climatological shift. However, sublimation and melt increase significantly within the full time-span of the RACMO2/ANT integration.

In the light of the good quality of this new dataset as described above, we conclude that this dataset offers a range of possibilities not only for the study of the Antarctic SMB, but also for research of regional climate-change, energy balance and circulation patterns.

Acknowledgements

Thanks to Dr. D. G. Vaughan for providing the data of his mass balance compilation, and to ECMWF which made available the ERA-40 fields.

Chapter 3

Reassessment of the Antarctic surface mass balance

Abstract

A detailed comparison of model simulated and observed Antarctic surface mass balance (SMB) is presented, using output of a regional atmospheric climate model (RACMO2/ANT) for the period 1980 to 2004. All available SMB observations from Antarctica ($N = 1900$) are used for the comparison, except clearly erroneous observations and data which are in areas where dominant SMB patterns occur on scales smaller than the model resolution. A high correlation is found ($r = 0.82$), while the regression slope (1.2) indicates that the model slightly overemphasizes SMB gradients. Comparing the model SMB with the latest SMB compilation, a similarly high correlation is found ($r = 0.79$), but the regression slope is much too steep because model simulated SMB agrees less with the compilation in data-sparse regions. Model simulated SMB resembles the observed SMB as a function of elevation very well. This is used to calibrate model simulated SMB to reassess the contemporary Antarctic SMB. Compared to the latest SMB compilation, calibrated model simulated SMB is up to 1 m per year higher in the coastal zones of East and West Antarctica, which are without exception in areas with few observations. As a result, the SMB integrated over the grounded ice sheet (171 ± 3 mm per year) exceeds previous estimates by as much as 15%. Support or falsification of this model result can only be found in new SMB observations from high accumulation regions.

3.1 Introduction

An important aspect of the influence of Antarctica on the global climate system is the storage of fresh water in ice, which lowers sea level by about 61 m (*Huybrechts et al.*, 2000). Changes in the ice volume on Antarctica, i.e., a nonzero mass balance of the grounded ice sheet (GIS), directly changes global sea level. Several Antarctic ice drainage basins have been reported to

This chapter has been published as: Van de Berg, W. J., van den Broeke, M. R., Reijmer, C. H., and van Meijgaard, E. (2006), Reassessment of the Antarctic surface mass balance using calibrated output of a regional atmospheric climate model, *Journal of Geophysical Research*, 111, doi:10.1029/2005JD006495.

be out of balance. In coastal West Antarctica, the Pine Island and Thwaites glaciers discharge each year about 250 km^3 of ice into the ocean, 60% more than is estimated to accumulate within their catchment basins (Thomas *et al.*, 2004). This is sufficient for a global sea level rise of 0.24 mm per year, a very significant number compared to the value of -0.1 ± 0.1 mm per year that was estimated for the contribution of the whole Antarctic ice sheet in the last century (IPCC, 2001). In contrast to the retreat in West Antarctica, satellite radar altimetry suggests that the ice sheet thickened between 1992 and 2003 in East Antarctica, lowering sea level by 0.12 mm per year (Davis *et al.*, 2005).

During the last decade, solid ice fluxes are determined with much higher precision because surface elevation changes and surface velocities can be measured by satellites (cf. Thomas *et al.*, 2004). However, such a step forward has not been made for the surface mass balance (SMB), because it cannot directly be measured by satellites. Recent SMB compilations are based on observations first of all, but in situ observations are lacking for vast areas of Antarctica. Giovinetto and Zwally (2000) visually interpolated the observations, and Vaughan *et al.* (1999) (hereinafter referred to as V99) used passive microwave data from satellites for their interpolation. Atmospheric models provide another estimate of the Antarctic SMB (Bromwich *et al.*, 2004; Genthon and Krinner, 2001). Model results are usually validated by subtracting the SMB compilation of V99 from the model simulated SMB and visually interpreting the differences. In that way model results can only be qualitatively assessed. A similar statement can be made about simulation of the Greenland SMB (Dethloff *et al.*, 2002; Box *et al.*, 2004; Box, 2005), where ablation plays a major role.

Here we carry out a more detailed and quantitative evaluation of model simulated Antarctic SMB. The simulated SMB includes solid precipitation, sublimation and snow melt. After the evaluation, we slightly calibrate model SMB to match observations, in order to get a best possible estimate of the contemporary Antarctic SMB. This reassessed SMB primarily provides a new estimate of the SMB where few observations are available.

We present a description of the model in 3.2. In section 3.3, SMB observations are presented and we describe how model values are interpolated to the location of the observations, and how observationally dense areas are treated. In section 3.4, we statistically compare model results with the compilation of V99 and with the derived observational data set. We consider the importance of temporal variability compared to spatial variability. The section is concluded with a verification of model simulated SMB as a function of elevation for East and West Antarctica separately. Section 5 discusses the statistical robustness of results. Finally, model simulated and observed SMB are combined to derive a best estimate of contemporary Antarctic SMB. Conclusions are drawn in section 3.6.

3.2 Model description

RACMO2/ANT is adapted from the second version of the Regional Atmospheric Climate Model (RACMO2). The atmospheric dynamics description of RACMO2 originates from the High-Resolution Limited Area Model (HIRLAM), version 5.0.6 (Undén *et al.*, 2002). The physical processes are adopted from the European Centre for Medium-Range Weather Forecasts (ECMWF), cycle CY23R4 (White, 2001).

The horizontal resolution of RACMO2/ANT is ~ 55 km. The model has 40 hybrid levels in the vertical, of which the lowest is ~ 10 m above the surface. Hybrid levels follow the topography close to the surface and pressure levels at higher altitudes. ECMWF Reanalysis (ERA-40) fields force the model at the lateral boundaries, while the interior of the domain is allowed to evolve freely. ECMWF operational analyses have been used to extend the model time series by 28 months until the end of 2004. Although the operational cycle is processed at double horizontal resolution compared to ERA-40, both products have been derived with a very similar formulation of the same numerical weather model and we consider the extension a useful and almost consistent continuation. Ice free sea surface temperature and the sea ice fraction are prescribed from ERA-40. Sea ice has a thickness of 1 m.

Several physical parameterizations within RACMO2/ANT have been changed to better represent Antarctic conditions. The snow albedo parameterization of *Van den Hurk and Viterbo (2003)* was implemented. For freezing conditions, the albedo decay in this parameterization is diminished proportional with the fourth power of the temperature. As a result, the albedo of snow remains almost constant below -10 °C. Furthermore, the surface roughness length for momentum was reduced (*Reijmer et al., 2004*), and the expression presented by *Andreas (1987)* was applied to calculate the surface roughness lengths of heat and moisture over snow surfaces. A four layer snow model was added to improve subsurface heat fluxes into the snowpack. These adjustments and their positive effect on the boundary layer, together with the setup of RACMO2/ANT, are described by *Reijmer et al. (2005)*.

In addition, horizontal diffusion of moisture has been decreased, which reduces artificial uphill moisture transport (*Lenderink et al., 2003*). Concentrations of CO₂ and other trace gasses were varied following IPCC 2001.

Finally, a correction was applied to the precipitation scheme. The original scheme puts the generated rain to snow ratio equal to the cloud water to cloud ice ratio. The ratio is a parabolic function of temperature and favors cloud ice for temperatures below -7 °C. Although such a cloud ice fraction closely below 0 °C is unrealistically high, it still overestimates the rain fraction of supercooled clouds. Supercooled clouds can only generate rain if the cloud contains cloud water only, which rarely happens. Snow formation processes dominate in the prevailing mixed clouds (*Rogers and Yau, 1989*). This model flaw is corrected by imposing that clouds below -1 °C form snow only. The effect of the additional energy release in the cloud on the temperature profile was found to be small.

Bromwich and Fogt (2004) and *Sterl (2004)* have shown that the quality of ERA-40 before 1980 is poor for the Southern Hemisphere. The incorporation of satellite data in 1979 causes a sudden increase of model simulated SMB for ERA-40 as well as for RACMO2/ANT (*Van de Berg et al., 2005*). Therefore we only use model results for the period 1980 to 2004.

3.3 Observations and data handling

Figure 3.1 shows the observed values of SMB that are used for the comparison. This data set is a revised version of that used by V99, which comprised 1796 observations. Furthermore, 236 new observations described by *Van den Broeke et al. (1999)*; *Frezzotti et al. (2004)*; *Karlöf et al. (2000)*; *Kaspari et al. (2004)*; *Magand et al. (2004)*; *Oerter et al. (1999, 2000)* and *Smith et al. (2002)* have been added. For the Antarctic Peninsula, data presented by

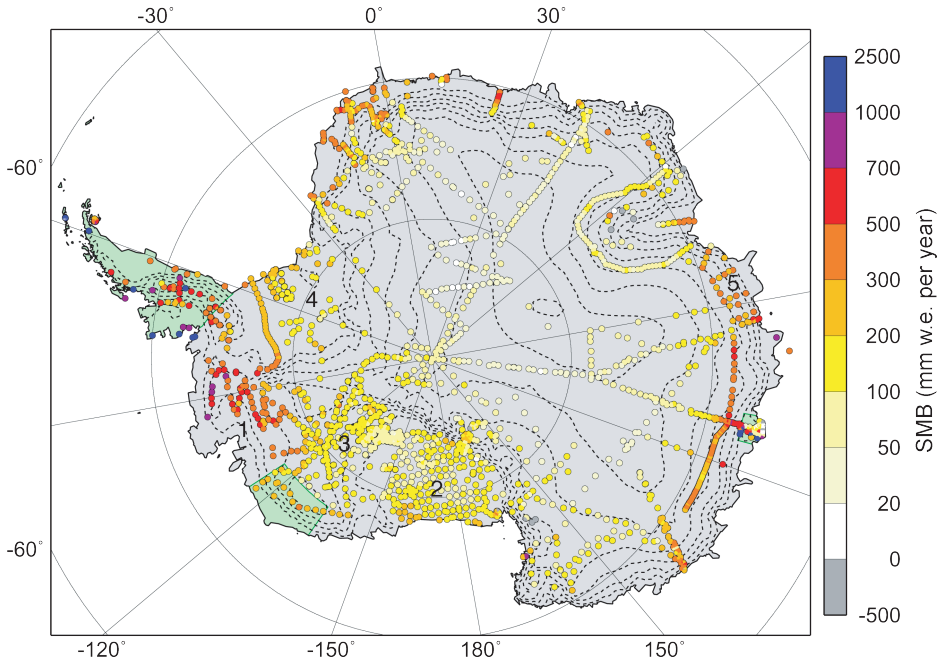


Figure 3.1: Observed surface mass balance (SMB) over Antarctica. Circles mark measurements. In case of clustered observations a continuous map is drawn. The excluded areas are marked with a green background. The numbers mark regions in Antarctica: 1, Pine Island and Thwaites Glacier; 2, Ross Ice Shelf; 3, Siple Coast; 4, Flichnerr Ronne Ice Shelf; 5, Wilhelm II Land.

Turner *et al.* (2002) have been used. The observations within the data set have been derived with various measurement techniques, for example stake arrays, bomb horizons or chemical analysis of ice cores. As a result, the time period covered by an observation varies from only a few years to more than a century. Single-year observations have been discarded.

Observations were checked for processing errors by comparing the stated elevation with Radarsat Antarctic Mapping Project (RAMP) elevations (Liu *et al.*, 2001), because an unreasonable elevation often indicates an error in the geographical location. Such possible errors and missing information on elevation and time horizons of the accumulation observations have been looked up in the original publications as much as possible. For binning purposes (see section 3.4.4), RAMP elevations have been used for unrecoverable elevations.

In the next paragraphs the arguments for omitting three areas are given, followed by the method of how observed SMB is compared with model simulated SMB. Lastly, a description is given of the treatment of areas with dense observations. The influence of data processing on the results will be discussed in section 3.5.1.

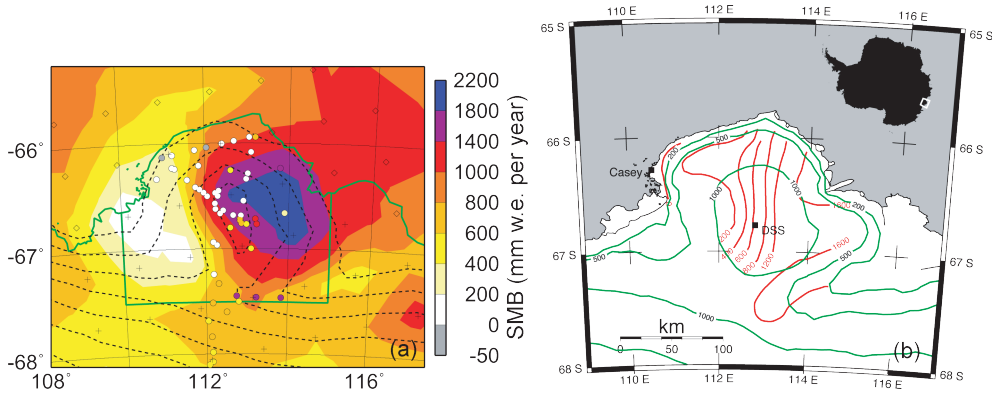


Figure 3.2: (a) Model simulated and observed SMB over Law Dome. Observations are indicated by circles. Crosses mark land grid points, and diamonds mark grid points on sea, for which the annual solid precipitation is displayed. The dashed contours display the model surface elevation with an interval of 250 m. The green borders indicate the edges of the land and ice shelves and also the border of the excluded area. (b) Pattern based on SMB observations from Van Ommen et al. (2004) (reprinted with permission from the International Glaciological Society), which disagrees with the observations in (a).

3.3.1 Excluded areas

Observations from three areas are excluded from the comparison between model simulated and observed SMB, namely, coastal Marie Byrd Land (MBL), the Antarctic Peninsula and Law Dome, indicated by green areas in 3.1.

The observations of Pirrit and Doumani (1961), made during the Marie Byrd Land traverse in the austral summer of 1959-1960, are the only available observations from coastal MBL. They estimated the SMB using snow density, descriptive stratigraphy, pit wall photographs and rammsonde hardness. The snow density was determined up to a depth of 10 m, while the pits were 3 m deep (~ 1 m w.e.). Using this information, they found SMB rates between 180 and 320 mm w.e. per year. Although visual interpretation has been shown to work well for plateau sites, it is not very reliable in areas of high accumulation, nor is it fully independent of the observers expectation (cf. Bull, 1971). A snow pit should cover at least one annual layer, so a snow pit depth of 3 m indicates that a larger annual accumulation rate was not expected. Passive microwave data, as presented by Zwally and Giovinetto (1995), do suggest a larger accumulation rate for this region. We decided to exclude all observations of Pirrit and Doumani (1961) north of 77° South and between 115° and 135° West. The remaining data set still contains observations that are based on visual interpretation techniques, but we chose to exclude only observations that are clearly erroneous.

We also exclude two regions with a combination of relatively high observational density and strong SMB gradients due to small-scale topography. The first area is Law Dome, where the typical length scale of elevation and accumulation variability is about 10 km. Exclusion is reasonable because the model surface topography of this region is smoothed, since the model resolution is ~ 55 km. Nevertheless, a similarity between observed (Figure 3.2b, Van Ommen et al. (2004)) and model simulated SMB (Figure 3.2a) is clearly present. The strong east-west

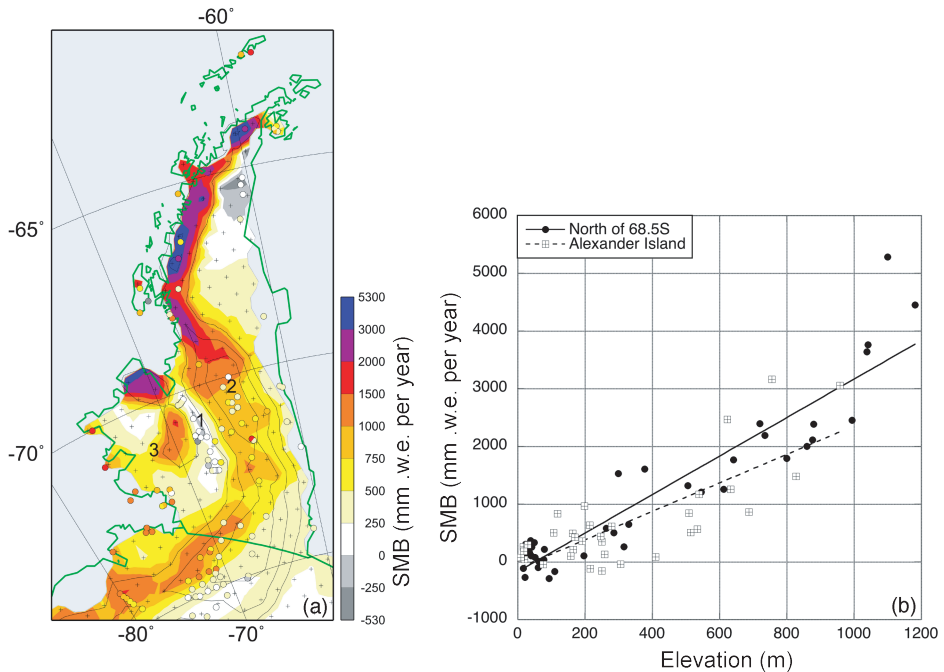


Figure 3.3: **(a)** Model simulated and observed SMB in the Antarctic Peninsula. Observations are indicated by circles. A light blue is used for model sea grid points. The crosses mark land grid points. Model elevation is drawn in thin black lines with 500 m interval. The thick green line indicates the actual edges of land and ice shelves and also the southern border of the peninsula. The numbers mark locations in the peninsula: 1, King George VI Sound; 2, Dyer Plateau; 3, Alexander Island. **(b)** Relation between elevation and model simulated SMB on the Antarctic Peninsula. The SMB of grid points north of 68.5° S (north of Dyer Plateau) and on Alexander Island are selected. The lines are linear fits.

SMB gradient as well as the magnitudes of maximum and minimum SMB compare well with *Van Ommen et al. (2004)*. The lower model resolution mainly shifts and smoothes the pattern. Surprisingly, the SMB observations in our observational data set, represented by the circles in Figure 3.2a, are not consistent with the pattern of *Van Ommen et al. (2004)*. Although the area of Law Dome is relatively small, these observations could seriously bias the regression due to its large SMB gradients.

The Antarctic Peninsula is the second area where topography is dominated by small-scale features. As a result, SMB observations are often not representative for an area that approaches the model grid box size and model topography does not always capture the characteristic topographic features. A second reason for leaving out the Antarctic Peninsula is the SMB behavior with elevation. On the Antarctic mainland, accumulation rates are rather low and decrease with height. On the Antarctic Peninsula, the magnitude of the SMB can be one order of magnitude larger and the SMB increases with height. Hence we exclude the Antarctic Peninsula in our comparison.

Nevertheless, the model simulated SMB for the Antarctic Peninsula (Figure 3.3a) is briefly evaluated here. Although the limited model resolution smoothes the topography, the model simulated SMB patterns are reasonable. For example, accumulation patterns in King George VI Sound are modeled well, because the model topography captures the sheltered position of the sound. The SMB on Dyer Plateau is overestimated, probably because the topographic shape of the Dyer Plateau in the model is still a ridge instead of a plateau. Smaller grid spacing indeed improves model simulated SMB patterns, as shown by *Van Lipzig et al.* (2004). They also showed that the influence of snow drift on the plateau of the Antarctic Peninsula cannot be neglected, however, this process is not included in RACMO2/ANT.

The model simulated SMB behaves rather linearly with elevation in the northern part of the peninsula (Figure 3.3b), in agreement with the linear relationship that was found by *Turner et al.* (2002) based on SMB observations. The model simulated SMB increases 3.3 mm w.e. per year per m elevation. This is much more than the 1.40 that was found by *Turner et al.* (2002) for the Western side of the peninsula. This might be due to the effects of snow drift which is not incorporated in RACMO2/ANT.

A linear relation between elevation and SMB is less distinct for Alexander Island. If all grid points in Alexander Island are used, the SMB increases with 2.5 mm w.e. per year per m elevation. The three large values (> 2 m) in the north eastern corner of Alexander Island largely determine the slope. If these are omitted, the slope decreases to 1.2 mm w.e. per year per m elevation. Figure 3.3a shows that the southern part of Alexander Island lies in the precipitation shadow of the northern hills. The relation between elevation and SMB is thus not equal above Alexander Island and in general lower than for the northern spine. These results differ from *Turner et al.* (2002), who uses the relationship of the northern peninsula to determine the SMB for Alexander Island as well.

We may conclude that the model qualitatively resembles the SMB and its gradients in the complex regions of Law Dome and the Antarctic Peninsula, but that model resolution is not sufficient to enable a quantitative comparison.

3.3.2 Model interpolation

The remaining observations and model values are compared by interpolating model simulated SMB to the location of the observation ($SMB_{g \rightarrow o}$). The interpolation is carried out using a weighted average of SMB of nearby model grid points. The weight $w_{g,o}$ of the model grid point g at the observation location o is given by

$$w_{g,o} = \alpha_o \cdot \max \left[0, 1 - \frac{dx_{g,o}}{dx_{max}} \right] \quad (3.1)$$

in which $dx_{g,o}$ denotes the distance between the grid point and the observation location and dx_{max} the maximum distance for which a grid point affects the SMB of this location. The scaling factor α_o makes the sum of $w_{g,o}$ over all grid points one.

The maximum distance dx_{max} is set to 55 km, equal to the grid distance. In that case the method boils down to a linear interpolation between the 4 surrounding grid points. For smaller dx_{max} , $SMB_{g \rightarrow o}$ approaches the SMB of the most nearby grid point and for larger dx_{max} the model simulated SMB field is smoothed. Observations that are outside the land domain of RACMO2/ANT are omitted.

3.3.3 Observationally dense areas

If all SMB observations are equally distributed over Antarctica, all model grid points over the ice sheet would have the same weight when observations are compared with interpolated model values. In practice, observations are very irregularly distributed and are in some parts strongly clustered. If all observations would be given equal weights, areas in Antarctica with dense observations would be overrepresented in the comparison. Therefore weighting of observations is necessary. Nevertheless, the reliability of a regional value increases when the number of observation increases. An area with dense observations is given a somewhat greater weight than areas with sparse observations.

The weighting starts with calculating the observation density d_g around grid point g as the sum of $w_{g,o}$ over all observations. Next, the observation density d_o around observation o is derived by

$$d_o = \sum_g \max[d_g, 1] \cdot w_{g,o} \quad (3.2)$$

in which a d_g less than one is set to one because a correction is only needed if the observation density exceeds 1. This d_o is scaled with a factor γ to get the weight β_o of an observation:

$$\beta_o = d_o^\gamma \quad (3.3)$$

and the scaled grid point weight W_g of a grid point is derived using

$$W_g = \sum_o \beta_o w_{g,o} \cdot \quad (3.4)$$

This scaled grid point weight W_g represents the weight of a grid point when weighted observations are compared with interpolated model simulated values. The scaling factor γ is set to -0.75, to some extent an arbitrary value. For this value of γ , an area with uniform observation density $d_g = 16$ per grid point receives a double weight W_g compared to areas where $d_g = 1$. However, in practice observations are not uniformly distributed and there are only a few distinct locations with dense observations. The derivation of d_o incorporates some smoothing; therefore a grid point with a d_g less than 16 could still have a weight W_g that exceeds 2 if it is surrounded by grid points with low d_g .

Figure 3.4 shows W_g as derived for the observations presented in Figure 3.1. Some parts of West Antarctica, like the Ross Ice Shelf and Siple Coast, are well covered by observations. The Filchner-Ronne Ice shelf, on the other hand, has a poor coverage. In East Antarctica, the coverage is on average so low that individual traverses can still be identified. The Antarctic Peninsula, coastal Marie Byrd Land and Law Dome have a zero weight because these areas are not included in the analysis.

Finally, the weight β_o is used to determine an approximation of the observed SMB_o on the grid points ($SMB_{o \rightarrow g}$), using the formula

$$SMB_{o \rightarrow g} = \frac{\sum_o \beta_o w_{g,o} SMB_o}{\sum_o \beta_o w_{g,o}} \quad (3.5)$$

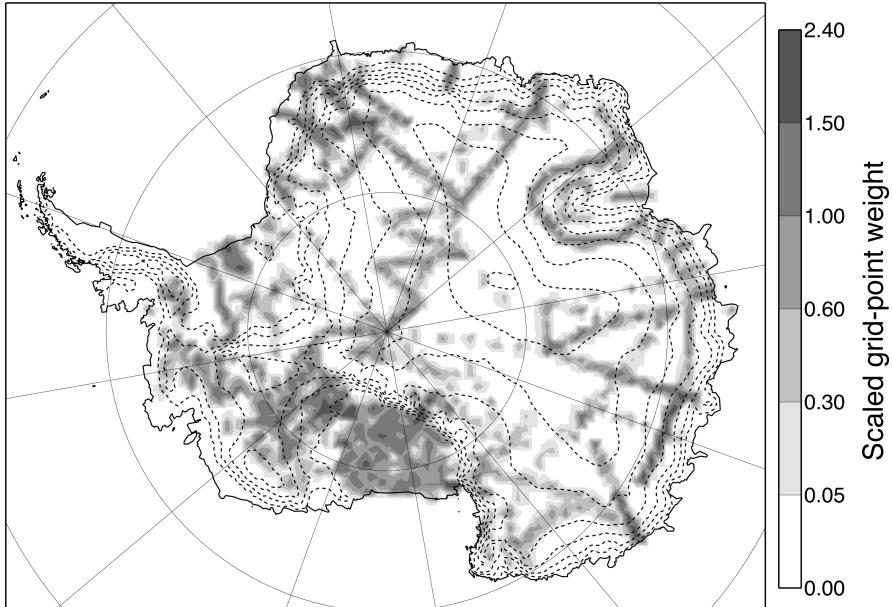


Figure 3.4: Scaled grid point weight (W_g) in Antarctica. Excluded areas have zero weight (see text).

3.4 Results

3.4.1 RACMO2/ANT compared to V99

Figure 3.5a depicts the difference between model simulated SMB and the compilation of V99. A clear general pattern is visible. The model simulated SMB in the high interior of East Antarctica is generally 20 to 40 mm lower, being only 25 to 75% of V99. In contrast, the model simulated SMB exceeds the compilation in general by 100 to 400 mm over the coastal slopes, except in the escarpment zone of Marie Byrd Land, where differences up to 1 m per year are found. Furthermore, the model simulated SMB compares favorably with V99 on the Ross Ice Shelf, the Filchner-Ronne Ice Shelf and the interior of West Antarctica. The model simulated SMB in the Antarctic Peninsula shows a stronger elevation dependency than the compilation does.

Figure 3.5b shows a scatterplot of model simulated and compiled SMB with each point representing a grid point of RACMO2/ANT. The fit is derived by minimizing the squared distances perpendicular to the fit line. Data from Law Dome, coastal Marie Byrd Land, and the Antarctic Peninsula are not included. The solid line is derived weighting all points equally. The correlation is 0.79 ± 0.011 and the slope of the best fit is 1.71 ± 0.06 (Table 3.1). Statistical error margins are derived by repeated fitting using a randomly chosen one third of the data set. The large regression slope links to the spatial pattern of a too dry simulated interior and an much wetter coastal zone. The mean SMB of RACMO2/ANT and V99 are

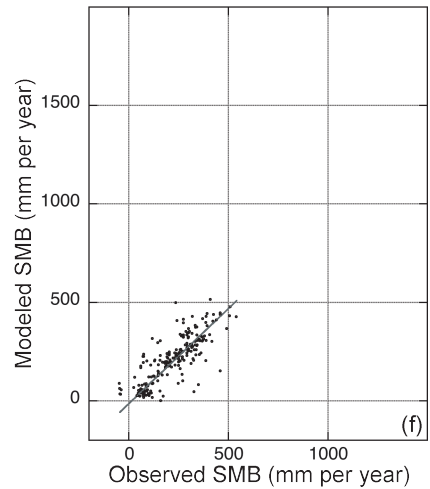
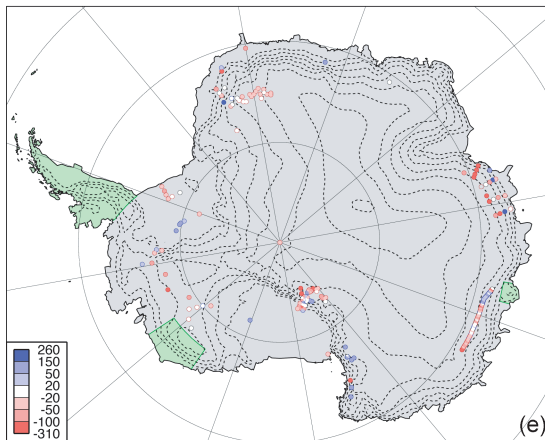
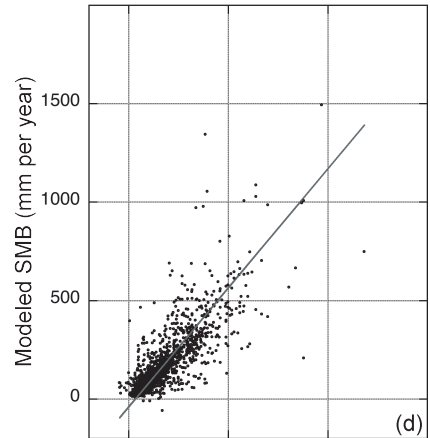
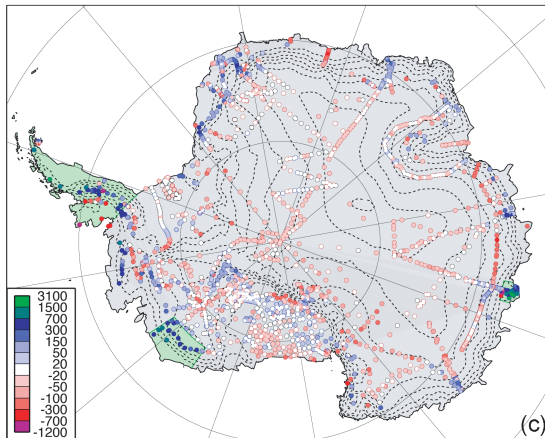
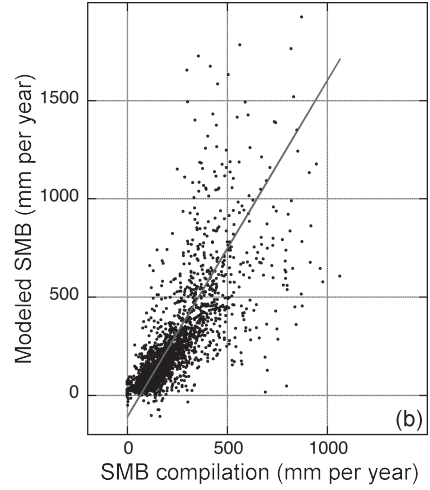
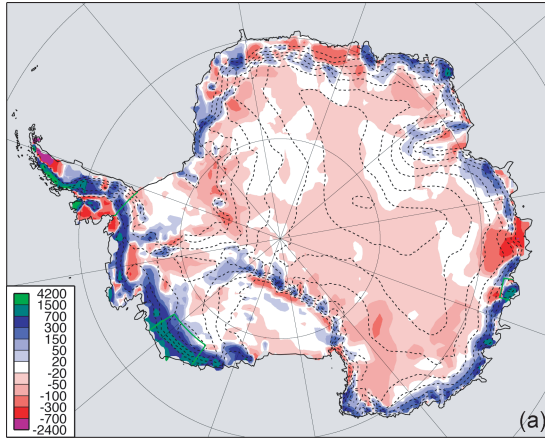


Figure 3.5: Comparison of model simulated SMB with compiled and observed SMB (mm w.e. per year). (a and b) Model results compared with V99. (c and d) Model results compared with observations. (e and f) Model results compared to observations, matching the time horizon of the observation. The excluded areas are bounded in (a) by a solid green line. In (c) and (e) these areas are drawn green. Figures (a), (c), and (e) show differences in mm per year. Positive values are used if the model simulated SMB is larger than the compiled/observed SMB. In Figure (b) a dot denotes a grid point; in Figures (d) and (f) a dot is an observation. The lines in Figures (b), (d), and (f) are regression lines. Fit properties are listed in Table 3.1, second, fourth, and sixth rows.

also listed in Table 3.1. The mean values are nearly equal, which implies that in the model the drier plateau of East Antarctica is balanced by a wetter escarpment.

3.4.2 RACMO2/ANT compared to observations

The differences between observed and model simulated SMB at the observation locations are shown in Figure 3.5c. The qualitative similarity between Figures 3.5c and 3.5a is strong, unsurprisingly perhaps, because the majority of the observations shown here were used to construct the SMB compilation. However, new observations do not always confirm the compiled SMB in V99. The most distinct examples are the recent accumulation observations in Wilhelm II Land, which are more than twice the value in V99 (Smith *et al.*, 2002). For comparison, RACMO2/ANT is on average 25% drier than these new observations.

The negative SMB bias in the model data in the interior of East Antarctica is confirmed by Figure 3.5c. Averaged over elevation, the model simulated SMB linearly decreases from 75% at 2500 m to only 30% of the observed SMB at 4000 m. The SMB on the large ice shelves agrees well and an overestimated accumulation along the coast is no longer that clearly apparent in Figure 3.5c: areas with overestimated accumulation alternate with areas where accumulation is underestimated and the absolute values are much smaller than in Figure 3.5a. In line with this, the slope of the regression line, shown in Figure 3.5d, is 1.21 ± 0.06 , which indicates that the distribution of SMB is well simulated. Furthermore, the correlation coefficient is 0.82 ± 0.016 . Note that this correlation coefficient cannot be compared directly to the correlation derived in section 3.4.1, because the data amount has decreased and the spatial distribution has become less homogeneous. Although weighting of observations was applied, areas without any observations do not count in this comparison. All in all, RACMO2/ANT reliably reproduces the Antarctic SMB, although with slightly too strong SMB gradients from the interior to the coast.

3.4.3 Impact of temporal mismatch

The results discussed in the previous section ignore temporal SMB variability. The model simulated SMB is averaged over the period 1980 to 2004, while observations are also averages, but averaged over different time periods. This might be problematic, because the model simulated SMB varies in time (Van de Berg *et al.*, 2005) and accumulation records may also show trends (e.g. Hofstede *et al.*, 2004). Therefore ignoring temporal variability could decrease the correlation between observed and model simulated SMB.

Table 3.1: Summary of SMB results.

Model simulated SMB compared to	N_{eff}^a ($\sum_o \beta_o$)	correlation	regression slope	mean SMB	
				(mm w.e. per year) V99/obs.	model
V99, whole Antarctica	4534	0.70 ± 0.02	2.1 ± 0.12	169	184
V99, selected areas	4333	0.79 ± 0.011	1.71 ± 0.06	152	153
Observations, whole Antarctica	1281	0.69 ± 0.04	1.7 ± 0.2	171	182
Observations, selected areas	1225	0.82 ± 0.016	1.21 ± 0.06	157	149
Observations, within 1980-2004	136	0.81 ± 0.04	1.00 ± 0.10	204	192
+ match time period	136	0.79 ± 0.05	0.96 ± 0.10	194	183

^aThe total weight of the data set (N_{eff}) is the sum of the individual observations weights β_o .

In order to investigate the impact of temporal variability, observations are selected of which the time domain is covered at least for 80% by the model integration period (1980 to 2004). In many cases, however, the time span covered by an observation could not be recovered. Hence application of this criterion strongly reduces the number of observations. Yet most zones are still represented, except the highest part of the plateau of East Antarctica (Figure 3.5e and Table 3.1, fifth and sixth rows).

The correlation of these observations to the mean model SMB is 0.81 ± 0.04 . If the observations are compared with model SMB for the exact time period covered by the measurement, the correlation decreases slightly to 0.79 ± 0.05 . Furthermore, the regression slope, which was close to one, does not vary significantly either. These minor changes confirm that temporal variability may be ignored when spatial variability is considered on timescales shorter than a century.

3.4.4 Elevation and SMB

Elevation is one of the most important factors for the SMB. Furthermore, the topography of East and West Antarctica differs significantly. East Antarctica has a steep escarpment and coastal zone with less ice shelves, and a high and large plateau. West Antarctica includes the extensive Ross and Filchner-Ronne Ice Shelves, and the slopes are on average more gentle. Moreover, West Antarctica does not have a similarly distinct plateau as East Antarctica. Therefore we consider SMB as a function of elevation separately for East and West Antarctica, excluding the Antarctic Peninsula.

Figures 3.6a and 3.6b compare model simulated and observed SMB in 500 m elevation bins, for which the elevation of the SMB observation is used. The lowest bin covers elevations from sea level to 250 m asl. The limited data set inhibits a smaller bin size. Since the SMB data is not normally distributed and thus standard deviations are improper, the averages of the upper and lower quartile are shown instead. In this case the tail to a high SMB is often much longer than the tail to a low SMB. The error bar on the bias displays the uncertainty on the bias and not the standard deviation.

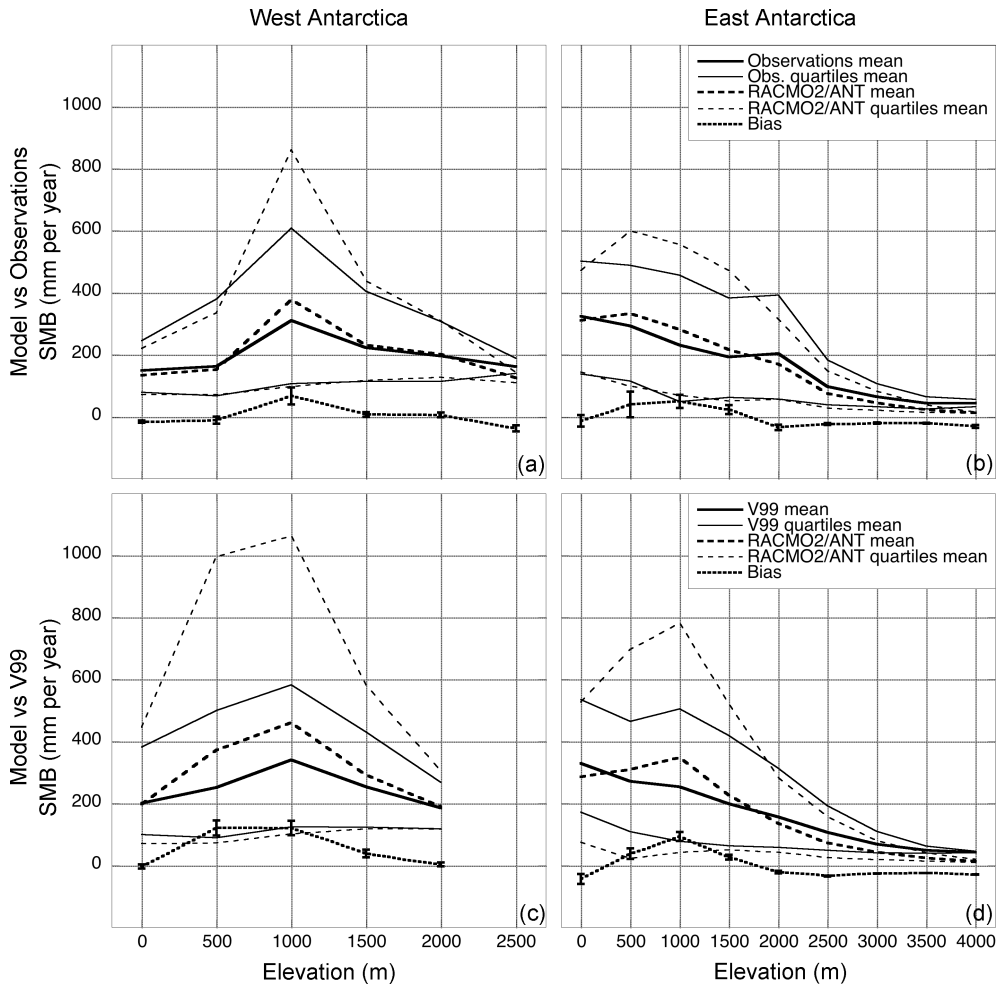


Figure 3.6: Comparison of model simulated SMB with (a and b) observations and (c and d) V99 for West Antarctica (a and c) and East Antarctica (b and d), as a function of elevation. The thick lines display the bin average, and the thin lines display the bin average of the upper and lower quartiles. The bias is the mean difference between model simulated SMB and V99/observations. The error bar is the statistical uncertainty on the bias.

The agreement between the model simulated and observed SMB for West Antarctica (Figure 3.6a) is good. The biases are small, only around 1000 m height the bias is clearly positive. Also, the distribution of the SMB is simulated well, even though the upper quartile mean is overestimated around 1000 m height. Another sign of the quality of the model simulation is that the correlations inside bins are all very high, between 0.75 and 0.91.

In East Antarctica (Figure 3.6b), RACMO2/ANT overestimates the SMB for high accumulation sites between 250 and 1750 m. On the plateau the distribution width is simulated well, but the mean SMB is 25 mm per year too low for all plateau bins. Since the SMB gradually decreases uphill, relative deficiencies increase to more than 50% at 4000 m. The correlation inside bins is around 0.7 for all bins, except for 250 to 750 m asl, for which the correlation is 0.54. However, only 18 observations are available for this elevation bin, while the variability is large. New observations of SMB from the coastal zones of Antarctica are therefore urgently required.

Figures 3.6c and 3.6d compare model simulated SMB with V99. Figures 3.6c and 3.6d are based on many more data points. Striking differences with Figures 3.6a and 3.6b are visible. The model simulated SMB and its spread are larger than V99 in the escarpment zones of both East and West Antarctica. Nevertheless, the correlation inside all bins is between 0.7 and 0.8. An exception is the lowest 250 m in East Antarctica, for which the correlation is only 0.41.

3.5 Discussion

3.5.1 Statistical robustness of the results

Before the implications of the model results will be discussed, their statistical robustness will be considered. The statistical analysis consisted of a number of steps, which all could influence the final results (Table 3.2).

First, observations from some parts of Antarctica (Antarctic Peninsula, Law Dome, coastal Marie Byrd Land) were excluded as discussed in section 3.3.1. Model simulated SMB interpolated to the observation location matches the observations less well for these regions, as can be concluded from the decrease in correlation coefficient when they are not omitted.

Second, the model simulated SMB is interpolated from model grid points to the observation locations, using equation (3.1). The default interpolation distance is 55 km, which implies that observations are nearly linearly interpolated between the 4 nearest grid points. If simply the model SMB of the nearest grid point is used, the correlation deteriorates. When model output is smoothed, the correlation improves. A maximum correlation is found for dx_{max} is 193 km. Simultaneously, the regression slope gradually decreases from 1.40 using the nearest grid point method to 1.06 for dx_{max} is 193 km. The decrease of the regression slope is a logical result of smoothing. From the fact that a certain amount of smoothing yields an improvement of correlation and the regression slope, we may conclude that the model simulated SMB distribution has somewhat too pronounced gradients.

Equation (3.1) uses a linear decrease of the relative weight for increasing distance. A test with a quadratical decrease of the relative weight leads to nearly equal results.

Table 3.2: *The effect of observation handling. The results are derived using all observations over Antarctica except from the excluded areas, unless noted otherwise. The effective data amount N_{eff} is the sum of β_o over all included observations. The correlations and regression slopes are from the comparison between model and observations.*

Adjustment	N_{eff}	correlation	regression slope
Default analysis (i.e. exclude areas, $dx_{max} = 55$ km, linear decreasing weight, $\gamma = -0.75$)	1225	0.82	1.21 ± 0.06
No areas excluded	1281	0.69	1.7 ± 0.2
Fit to most nearby model grid point	1225	0.78	1.40 ± 0.09
Smoothed model output for $dx_{max} = 193$ km	1225	0.84	1.06 ± 0.04
Weight decreases quadratically	1225	0.82	1.20 ± 0.06
Weight scaling $\gamma = -0.5$	1373	0.82	1.21 ± 0.05
Weight scaling $\gamma = -1.0$	1110	0.82	1.21 ± 0.06
Outliers removed ($ da \leq 300$ mm)	1205	0.87	1.08 ± 0.01
Unequal measurement error		0.81	1.14 ± 0.04
Effect of elevation biases ($ dh \leq 250$ m)	1193	0.82	1.23 ± 0.06

Third, observations have been weighted in order to balance the unequal spatial distribution of measurements. However, the weight function is more or less arbitrary. Fortunately, tests with different values of γ in equation (3.3) show that this has no impact on the results.

We conclude that these three steps of the data analysis procedure do not strongly influence the final results, except that some additional smoothing would improve the correlation between model simulated and observed data.

Additionally, the assumptions behind the statistics are validated. A properly determined regression line assumes a smooth distribution of the data, a requirement which is not fully satisfied as visible in Figure 3.5d. If outliers are removed, the slope of the regression decreases, because for about two thirds of the outliers the model simulated SMB exceeds the observation. The result for a maximum accepted difference of 300 mm is given in Table 3.2 as an example. Another way to deal with nonhomogeneous data distribution is by using an additional weight that incorporates a linearly increasing error margin for the model simulated and observed SMB. Table 3.2 shows the results for the assumption that the error margin for a SMB of 200 mm is twice that of a SMB of 0 mm. In line with this particular example, the regression slope decreased for stronger weighting. Concluding, both inquiries give a decrease of the regression slope toward one, which affirms that the model simulated distribution of the SMB is close to the observed one and that the correlation has not been strongly influenced by the data distribution.

A final source of error could be elevation differences between the observation site and the representative grid box. The observed elevation may be inaccurate or it may not match model elevation in the case of small-scale topographic features. If such observations are removed the correlation slightly improves, but the regression slope remains unchanged. The impact on the results is thus small.

Table 3.3: Regression quantities of different data sets compared to observations. All observations are used, except from excluded areas (see text).

Observations compared with	correlation	regression slope
Observations interpolated to grid points	0.971	0.945 ± 0.010
Vaughan <i>et al.</i> (1999)	0.928	0.94 ± 0.02
RACMO2/ANT	0.82	1.21 ± 0.06
Interpolated mean SMB for 500 m elevation bins	0.59	0.39 ± 0.02

3.5.2 An evaluation of model performance

The detailed comparison with observations in section 3.4.2 and 3.4.4 revealed that RACMO2-/ANT underestimates the SMB on the plateau of East Antarctica. The bias is between 20 and 44 mm per year. Most contemporary numerical SMB estimates (*Bromwich et al.*, 2004; *Genthon and Krinner*, 2001; *Van Lipzig et al.*, 2002b) show a similar underestimation of the SMB on the plateau. Diamond dust has been shown to contribute significantly to the SMB on the plateau (*Ekaykin et al.*, 2004). Since diamond dust, which essentially is a removal of boundary layer cloud ice, is not yet specifically parameterized in the model physics, the underestimated SMB is likely in part due to this neglected process.

For the remainder of Antarctica, a direct comparison with observations shows a very reasonable agreement. The range of the SMB is simulated well, although slightly overestimated in some cases, and the correlation between the model simulated and observed longitudinal variations is high. Moreover, model simulated SMB is more accurate than would be expected from a direct comparison with V99.

A quantitative assessment of model performance is listed in 3.3. First, observations of SMB are compared with the weighted mean of observations on grid points, using equation (3.5). This interpolation removes all patterns smaller than 55 km. The deviation of the correlation from one indicates the amount of such small-scale patterns in the observation data set. The value does not represent the average contribution of small-scale variability on the total spatial variability of the SMB of Antarctica, because in that case a high observation density for whole Antarctica is required.

Second, the observations are compared to V99 data, choosing the nearest value in the original 10 km grid. It is no surprise that the compilation resembles the observations adequately. If V99 is compared to new observations that were not used in the compilation, the correlation is 0.75. The correlation of RACMO2/ANT to these new data is 0.82, similar as for the whole data set.

Finally, the observations are compared with the observed mean of their elevation. This mean is linearly interpolated from the results as given in Figures 3.6a and 3.6b. The results show that a simple SMB estimate based on elevation is still significantly correlated with the observations, but that a significant fraction of the variance explained is lost. Moreover, the spread of the SMB in Antarctica is severely underestimated, because the regression slope is far below one. We conclude that the model simulated SMB distribution doubles the variance explained in the observations as compared to very simple parameterizations, and is also better capable of representing the absolute values.

3.5.3 Towards a better understanding of Antarctic SMB

In this section, the calibration of model results to fit observations is discussed. The calibration aims at retrieving a SMB distribution that is as correct as possible. In contrast, an intelligent interpolation of the observations using RACMO2/ANT data as background field would have focused on regional correct distributions. The calibration performed here gives insight in the major remaining uncertainties of the contemporary spatial SMB of Antarctica.

In section 3.4.4, the bias and slope of the regression line were derived for each elevation bin in East and West Antarctica. If the model results would have matched the observations perfectly, the bias would be zero and the regression slope one. An adjustment of the model results toward these perfect fits only improves the results if the correlation between observations and model in a bin is significant. Most elevation bins have a high and strongly significant correlation, which makes a correction feasible.

The model simulated SMB (SMB_g) is calibrated to $SMB_{g,c}$ with

$$SMB_{g,c} = \frac{SMB_g - \overline{SMB}_{mod}}{\max(0.9, s^\zeta)} + \overline{SMB}_o, \quad (3.6)$$

in which \overline{SMB}_{mod} and \overline{SMB}_o are the mean model simulated and observed SMB for the elevation of the model grid point, respectively. The regression slope s to the power ζ scales the model simulated SMB variability along elevation bands to observed variability, but only if the variability is larger than the observed variability. If this threshold is not applied, nonexisting variability might have been created. The values of \overline{SMB}_{mod} , \overline{SMB}_o and s are linearly interpolated for each grid point from the binned results. Optimal results are found for $\zeta = 0.5$ and a threshold value of 0.9.

Figure 3.7a shows the calibrated spatial SMB. The first main difference with the original model field is the 20-30 mm per year wetter plateau of East Antarctica. Second, the accumulation in the coastal and escarpment zone between 500 and 1500 meter elevation is on average reduced with 15%. Note that the correction that is applied for the Antarctic Peninsula uses correction data from West Antarctica, so model results in this area must be interpreted with care. Furthermore, note that this correction is a calibration and not an interpolation of observations using model results as background, so locally the calibration might diverge model results from observations. The overall correlation with the observations increases slightly to 0.83 and the regression slope becomes 1.00.

We also show the statistical uncertainty of the calibrated SMB in Figure 3.7b. This uncertainty is determined by repeating the calibration procedure 10.000 times using a randomly chosen one third of the observations. The resulting standard deviation is a measure of the uncertainty of the calibrated SMB distribution owing to the calibration procedure. For all locations the statistical uncertainty is one order of magnitude smaller than the SMB.

Subsequently, Figure 3.8a shows the differences of the calibrated SMB with the observations. Although the calibration procedure did not focus on individual observations, overall the deviations have decreased (Figure 3.5c). These improvements are clear for the interior of East Antarctica. Elsewhere, improvements are less traceable because of the scatter between model data and observations. Noteworthy is that within one transect the calibrated SMB is often strongly correlated to observations. Examples are the transects at 20° and 40° West and ~72° South.

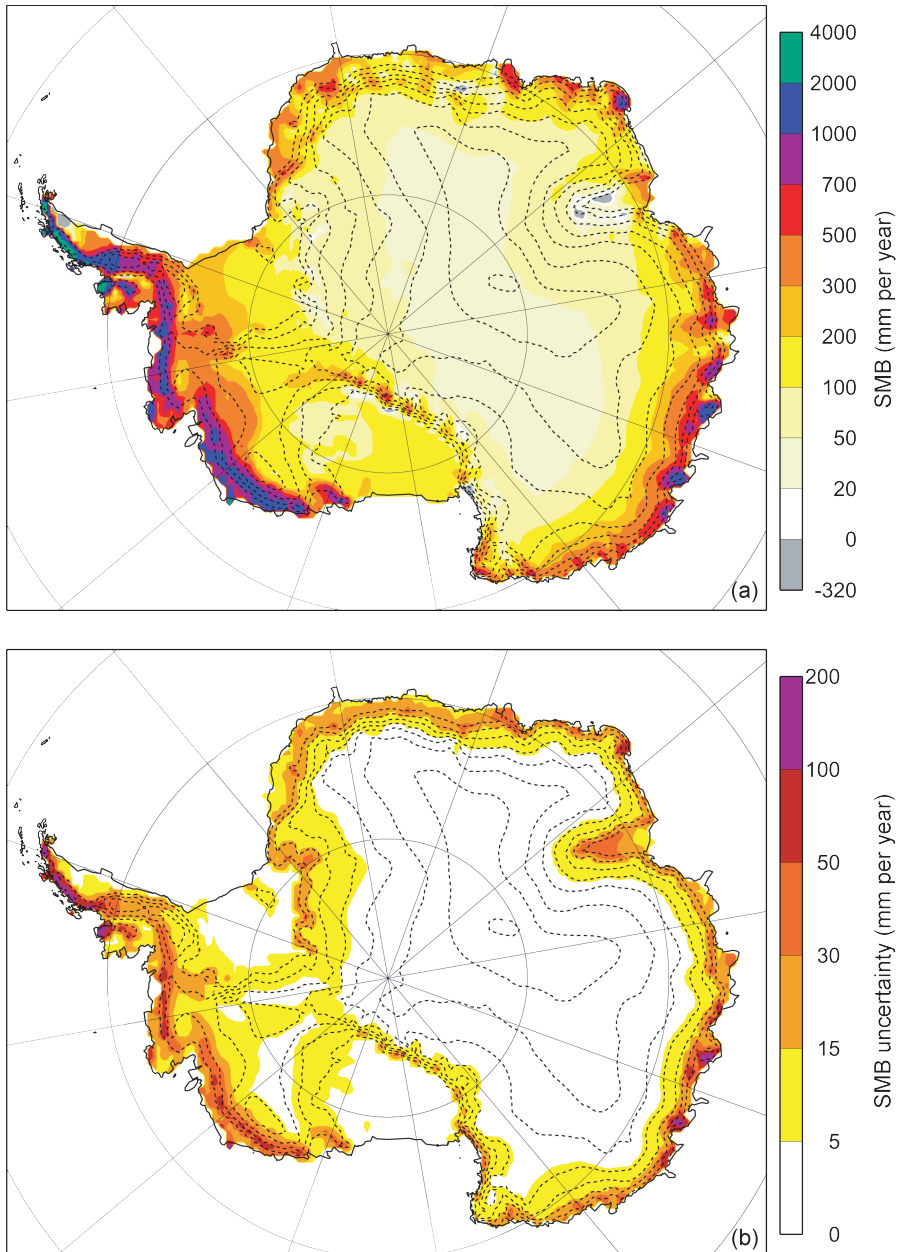


Figure 3.7: (a) Calibrated model SMB and (b) statistical uncertainty due to calibration procedure. Only model land points are shown. The SMB of the Antarctic Peninsula is calibrated using the data from West Antarctica.

The calibrated SMB is compared to V99 in Figure 3.8b. For the most of Antarctica, the differences are closely connected with those in Figure 3.8a. Exceptions are the much higher model simulated SMB in the coastal regions which are East of Law Dome in East Antarctica and the Amundsen and Bellingshausen Sea coast of West Antarctica. These differences are also much larger than the statistical uncertainty of the calibrated SMB, and exceed the range of deviations that is found between the calibrated model results and the observations.

In Figure 3.8c the relative differences of the model with the compilation of V99 and the biases to the observations are shown. As indicated earlier, since V99 is a proper interpolation of almost all observations used in this manuscript, there is a general correspondence between the two. The biases are all within a reasonable limit. Consequently, significant deviations of the calibrated SMB fields with the compilation of V99 in areas poorly covered by observations, visible in the above listed regions, can unlikely be blamed on poor model performance. Therefore the SMB of these regions has likely been severely underestimated until now.

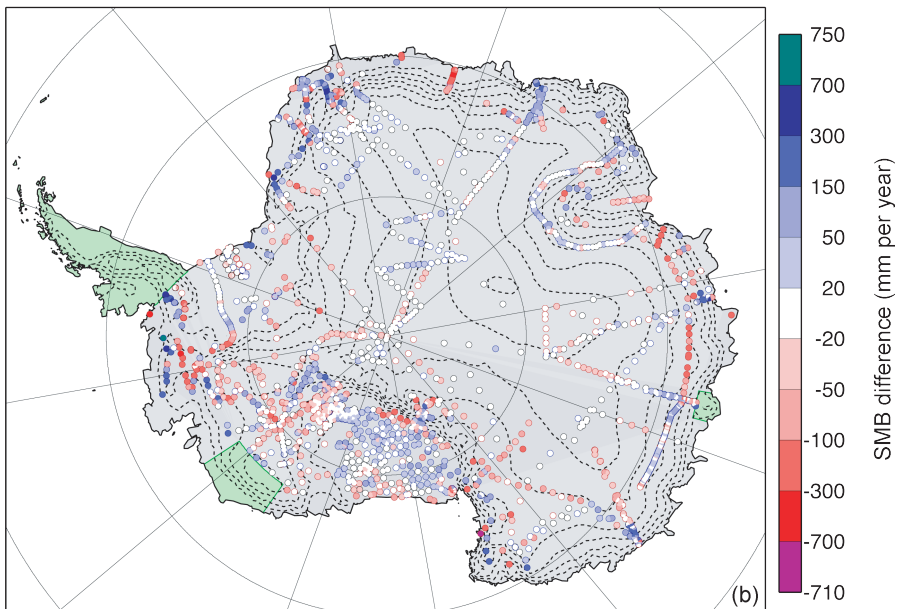
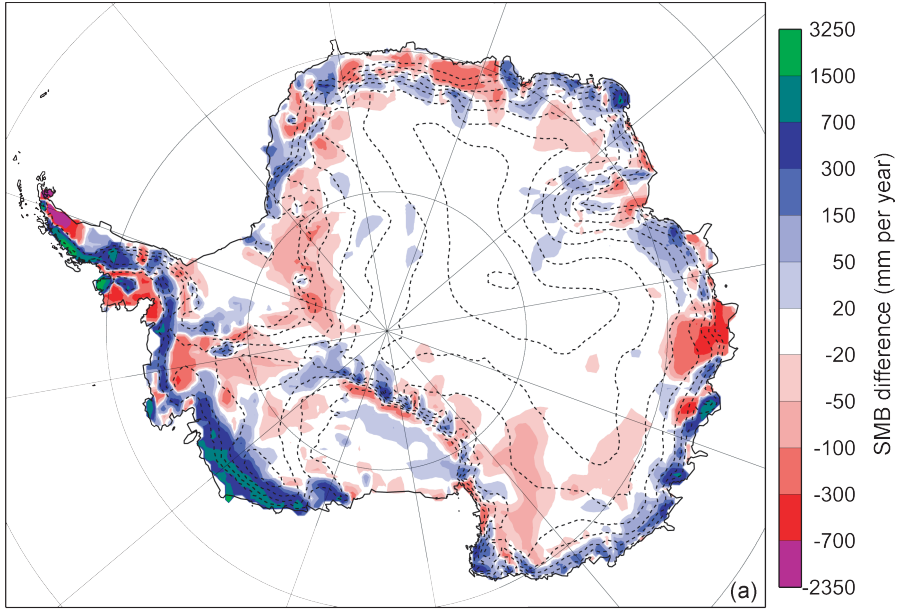
Next, the model simulated and calibrated SMB are averaged over the grounded ice sheet (GIS). RACMO2/ANT simulates an integrated SMB of 169 mm per year for 1980 to 2004, the calibrated average SMB is 171 ± 3 mm per year. This estimate is about 15% higher than the estimate of V99 (149 mm per year). The calibrated SMB equals a total mass input to Antarctica of $2.08 \pm 0.03 \times 10^{15}$ kg per year for the GIS and $2.52 \pm 0.03 \times 10^{15}$ kg per year for the whole of Antarctica including ice shelves. These values are higher than all estimates listed by IPCC (2001, page 651), but they are comparable with the recent model estimate from Bromwich *et al.* (2004) (Table 3.4). The increase of the SMB compared to the IPCC estimate represents an additional storage of water on Antarctica of 0.6 mm global sea level per year. Since model results are calibrated with observations of which most cover an older time period, the likelihood is small that increased precipitation in the last two decades of the 20th century is the source for this difference.

The largest uncertainties about the contemporary spatial SMB distribution in Antarctica lay in the coastal and escarpment regions. The sharp accumulation gradients and the large-scale longitudinal variations related to the upper air circulation (Van Lipzig *et al.*, 2002b), combined with few observations, cause these uncertainties. Although these regions make up only a small fraction of the Antarctic continent, their impact on the integrated SMB is substantial because of the large average accumulation rates. If indeed the SMB of these regions is larger than previously thought, the annual mass input in the grounded ice sheet of Antarctica is larger than recent estimates have suggested. The only method to validate or disprove these results is to perform more SMB measurements in coastal areas of Antarctica.

3.6 Conclusions

We made a detailed comparison of model simulated and observed SMB in Antarctica, and calibrated the model simulated SMB distribution to construct a best estimate of contemporary Antarctic SMB.

The model results used here are from a regional atmospheric climate model (RACMO2-/ANT) for the time period 1980 to 2004, using ERA-40 fields as lateral forcing. The model results of the period 1958-1979 are not used because of the poor quality of ERA-40 in the Southern Hemisphere before 1980 (Bromwich and Fogt, 2004).



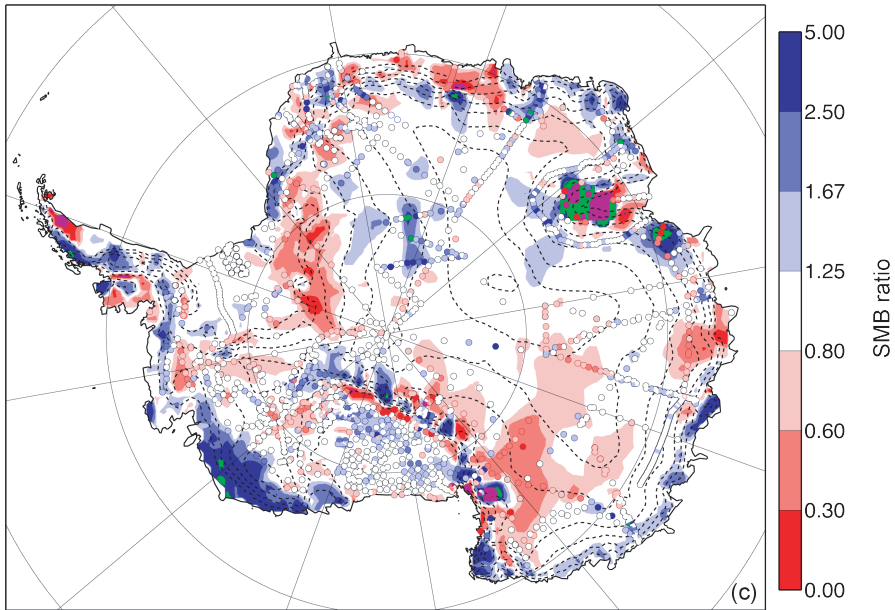


Figure 3.8: (a) Differences between calibrated model SMB and the observations that were used for the calibration. (b) Differences between calibrated model SMB and V99. (c) Continuous map showing the ratio between the calibrated model results and V99. The overlaid circles are the ratio between the calibrated model results and observations. Values larger than one indicate that the calibrated SMB is larger than the observations or V99.

Table 3.4: Estimated SMB, integrated over the grounded Antarctic ice sheet (GIS) or including ice shelves and compared to recent other estimates as listed by IPCC (2001).

Source	Remarks	GIS (10^{12} kg yr $^{-1}$)	All ice sheets (10^{12} kg yr $^{-1}$)
Turner et al. (1999)	Atmospheric moisture budget analysis from ECMWF re-analysis, 1979 to 1993		2106
V99		1811	2288
Huybrechts et al. (2000)	Updated accumulation map.	1924	2344
Giovinetto and Zwally (2000)	Updated map on 50 km grid.	1883	2326
IPCC (2001, p. 651)	Mean and standard deviation	1843 ± 76	2246 ± 86
Van Lipzig et al. (2002b)	Precipitation minus evaporation using RACMO1/ANT	1890 ± 90	
Bromwich et al. (2004)	Precipitation minus evaporation using regional atmospheric model MM5		2572 ± 221
This study, 1980-2004		2076 ± 29	2521 ± 33

We used all available SMB observations for the comparison. Observations were only discarded if clearly erroneous. Before the comparison, the individual weight of clustered observations was reduced, otherwise these areas would be overrepresented. Furthermore, the Law Dome area and the Antarctic Peninsula are left out of the comparison, because of small-scale topography that inhibit a meaningful quantitative comparison on model resolution (55 km). Model results for these areas have been discussed separately

Comparing model simulated SMB with the compilation of *Vaughan et al.* (1999), a correlation of 0.79 and a regression slope of 1.7 is found. When model simulated SMB is directly compared to observations, a correlation of 0.82 and a regression slope of 1.21 is found. The model simulated SMB closely matches the observations and V99 in data covered regions, but does not agree with V99 in data-sparse regions. We binned the observations in 500 m elevation intervals for East and West Antarctica and compared these to model SMB in each bin separately. The correlation remains high (0.66 to 0.91) and the mean and distribution of the SMB compares well for most bins, although a systematic underestimation is found for the high plateau of East Antarctica. These results support the robustness of the model simulated SMB and offers the possibility to calibrate model simulated SMB without losing reliability.

The main difference between calibrated model SMB and the compilation of V99 is a higher model SMB in the coastal zones of (eastern) East Antarctica and West Antarctica, without exception areas with few observations. Along the coast of Marie Byrd Land the differences reach 1 m w.e. per year. These higher values result in a 15% higher estimate (171 ± 3 mm per year) of the SMB integrated over the grounded ice sheet compared to V99. Despite the apparent small statistical uncertainty which is based on the calibration procedure only, this new estimate of Antarctic SMB is as reliable as the reliability that is credited to atmospheric models. Support or falsification of this result can only be found in new SMB observations from poorly covered high accumulation regions in coastal Antarctica.

Acknowledgements

We would firstly like to thank David Vaughan for providing his SMB observation database and the data of his SMB compilation. We also would thank Massimo Frezzotti, Susan Kaspari, Hans Oerter and Roderik van der Wal for providing recent SMB observations. We are grateful to Elisabeth Isaksson, Lynn Lay, Nicole van Lipzig, Andrew Monaghan and Rob Mulvaney for their valuable help on various parts of this project.

Chapter 4

Error evaluation of a surface mass balance estimate

Abstract

A method is presented to calculate area-averaged error margins for modeled variables using an a priori error estimate. This method is tested and applied to two model-based surface mass balance (SMB) maps of Antarctica. First, error margins are assigned to observations and model output. Then, the factors in these expressions are optimized to obtain a normal distribution of the remaining differences between predicted and observed SMB. Next, the error autocorrelation distance is required for averages over ice drainage basins. This autocorrelation distance is obtained from the decorrelation distance of model deviations from observations. Using this method, relative error margins in drainage-basin mean SMB are obtained that range from 10% for large and arid drainage basins to 30% for small and wet basins.

4.1 Introduction

An error estimate is often essential to assess the significance of presented results. But in meteorology, it is not simple to assign an error to a model result. For observations, the uncertainty is determined by the technical limitations of the measurement device. The model uncertainty, however, can only be estimated afterwards by comparing model results with observations that have not been used for tuning.

Here, we describe how error margins can be calculated for basin-mean, model estimated SMB over ice sheets. For this, we use >1900 Antarctic SMB observations from *Van de Berg et al. (2006)*, Chapter 3 of this thesis, from now on referred to as ‘observed SMB’. Further we use maps of modeled Antarctic SMB from *Van de Berg et al. (2006)* and *Van den Broeke et al. (2006c)*. These maps will be referred to as ‘model estimated SMB’.

In the next section, an error margin is constructed and evaluated for model estimated SMB in a single grid box. Next, in order to properly average the SMB error margin over a basin, the auto decorrelation distance for SMB deviations is calculated. The auto decorrelation distance

determines the effective number of degrees of freedom in the basin under consideration. In Section 4.3, SMB error estimates are presented for the drainage basins originally used in *Vaughan et al.* (1999) and later applied to model results in *Van den Broeke et al.* (2006b). Section 4.4 discusses the results.

4.2 Method

4.2.1 Definition of error margins

The error margin E_o of a single SMB observation SMB_o , in mm per year, is assumed to consist of a constant contribution of 5 mm plus 15 percent of the SMB value:

$$E_o = 5 + 0.15 \cdot |SMB_o| \quad (4.1)$$

An error margin of fifteen percent is a reasonable number since SMB_o can vary several tens of percents on km or even sub km scales, even on the East Antarctic plateau. This error margin thus mainly accounts for the uncertainty in spatial representativeness in a single SMB observation.

In this analysis, model estimated SMB fields of *Van de Berg et al.* (2006) and *Van den Broeke et al.* (2006c) are used. Since both fields are based on RACMO2/ANT model output, the error margin is assumed to be of similar shape. For both fields, denoted by SMB_m , the error in model estimated SMB for a single grid box is assumed to obey (in mm per year):

$$E_m = c_1 + c_2 \cdot |SMB_m| + c_3 \cdot SMB_m^2 \quad (4.2)$$

For high SMB_m values the error margin may exceed 30% of SMB_m , but is then maximized to 30% of SMB_m . Qualitative arguments to support this choice for the error in model estimated SMB for a single grid box are:

- a) Low SMB_m (<100 mm per year) is found on the extensive East Antarctic plateau. SMB is well calibrated there. However, low SMB sites are also found at lower elevations and the uncertainty is larger for these locations. The error margin thus reaches a minimum value for zero SMB_m but always remains larger than zero.
- b) In the medium SMB range (100 to 400 mm per year), SMB_m agrees well with observations. The error margin in this range has the lowest relative value.
- c) The relative and absolute errors both increase for high SMB_m (>400 mm per year), because few observations are available in this range for comparison and model calibration. The relative error margin is maximized at 30%.

4.2.2 Verifying error margins

The optimum values of c_1 , c_2 and c_3 in Equation (4.2) are obtained by looking at the difference between observations and model estimated SMB in a single grid box. This difference

Table 4.1: Optimal parameters for Equation (4.2) and decorrelation distances R_a .

SMB estimate	parameters for Eq. (4.2)			R_a (km)	
	c_1	c_2	c_3	<2000 m	>2000 m
<i>Van de Berg et al. (2006)</i>	10	0.09	0.00029	155	281
<i>Van den Broeke et al. (2006c)</i>	8	0.11	0.00037	154	473

can be normalized with the total error margin, i.e. the squared-summed error margins of model estimated and observed SMB, to obtain $dSMB$:

$$dSMB = \frac{SMB_m - SMB_o}{\sqrt{E_o^2 + E_m^2}}. \quad (4.3)$$

For a properly estimated error margin, the distribution of $dSMB$ should be a normal distribution with $\sigma = 1$. The error margin should be applicable to the whole range of SMB's, therefore subsets with high (>300 mm per year), medium (100-300 mm per year) and low (<100 mm per year) SMB values have been created. The mean of observed and model estimated SMB is used as threshold, in order to avoid biases. Next, the optimal value of E_m is found by minimizing the deviation of the four $dSMB$ distributions from the normal curve.

Ideally, the parameters for E_o and the maximum relative error of E_m , fixed here at 30%, are also optimized. However, E_o and E_m are not independent, a larger E_o induces a smaller E_m and vice versa. A good estimate of the uncertainty in observations thus improves the quality of the final model uncertainty. Furthermore, too few high SMB observations are available for a proper determination of the maximum relative error of E_m : only 13% of the observations has a SMB larger than 300 mm per year.

The optimized values of c_1 , c_2 and c_3 are listed in table 4.1 and the distribution of $dSMB$ for all available observations using the maps of *Van de Berg et al. (2006)* and *Van den Broeke et al. (2006c)* are shown in Figure 4.1. The solid black line represents the distribution using all observations. The red, purple and blue lines shows the distributions for low, medium and high SMB classes, respectively. The low and medium SMB groups contain the majority of the observations (45 and 43%, respectively). The distributions match the normal distribution ($\sigma = 1$), represented by the dashed black line well. We conclude that the optimized error margins calculated using Equation 4.2 statistically explain the remaining differences between model estimated and observed SMB.

4.2.3 Spatial error autocorrelation

We also want to be able to assign an uncertainty to basin mean modeled SMB. If differences between model estimated SMB and observations are due to physical processes that are active on spatial scales larger than the model grid cells, deviations in adjacent grid cells will be spatially correlated. This means that individual grid cells in a basin cannot be considered independent for calculation of the error margin for basin mean SMB. To correct for this, we calculated the distance at which the differences between model estimated SMB and observations become spatially decorrelated. As the correlation exponentially decreases for increasing distance, an exponential function is fitted to these correlations.

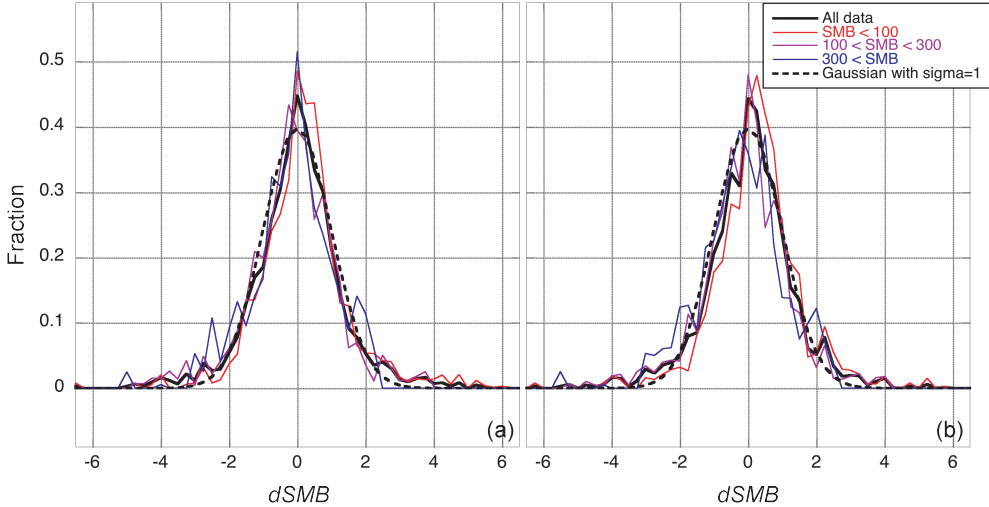


Figure 4.1: Distribution of $dSMB$ (Eq. 4.3) for (a) Van de Berg et al. (2006) and (b) Van den Broeke et al. (2006c). The solid black line is the distribution for all observations. The red, purple and blue lines are the distributions for low, middle and high SMB classes, respectively. The dashed black line represents a Gaussian distribution curve for $\sigma = 1$.

Since spatial SMB patterns have larger scales in the interior plateau, the decorrelation distance R_a is calculated separately for the area below 2000 m and for the area above 2000 m. The first step to obtain R_a is to calculate the correlation between model errors for each occurring distance between grid boxes. The correlation of model errors exponentially decreases to zero for increasing distance; the second step is thus to fit an exponential function to these correlations. Finally, R_a is set equal to the distance where the exponential fit shows less than 5% correlation. The area in which model estimates are assumed to be dependent is then bounded by a circle with radius R_a . It implies, for example, that a basin contains an independent estimate of model SMB error for each app. $125 \times 10^3 \text{ km}^2$ (approximately 40 grid boxes) if R_a is 200 km.

Note that R_a does not represent the auto decorrelation distance of SMB in Antarctica. The latter is much larger (approximately 600 km), as it is primarily determined by continental scale SMB patterns of a dry interior and a wet coast. This larger value should not be used, because it is not the auto decorrelation distance of SMB itself that is relevant here, but that of its errors.

4.2.4 Error for basin mean SMB

Using E_m as defined in Equation (4.2) and the auto decorrelation distance, the error margin in model estimated SMB for basin means ($E(b)_m$) is:

$$n_{free} = MAX\left(1, \frac{A_h}{\pi R_{ah}^2} + \frac{A_l}{\pi R_{al}^2}\right) \quad (4.4)$$

$$E(b)_m = \frac{\sqrt{\sum_{n=1}^{basin} E_m^2 \cdot A_{grid\ box}}}{\sqrt{(A_h + A_l) \cdot n_{free}}}, \quad (4.5)$$

in which $A_{grid\ box}$ is the grounded ice sheet area within a gridbox (in km²), n_{free} is the number of independent model points in the basin, and A_h and A_l are the area of the basin of interest (in km²) above and below 2000 m, respectively. Note that $E(b)_m$ is the standard deviation of the model estimated SMB, not the 95% confidence interval. $E(b)_m$ thus represents the most likely range of basin mean SMB.

4.3 Application

We tested the method on the basin definition from *Vaughan et al.* (1999), which was applied to the RACMO2/ANT grid in *Van den Broeke et al.* (2006b). Figure 4.3 shows the basin average model estimated SMB and error margin using the SMB fields of *Van de Berg et al.* (2006) and *Van den Broeke et al.* (2006c). The basin average presented by *Vaughan et al.* (1999) is also included. The data for this graph are also given in Table 4.3.

As can be seen, the error margins in model estimated SMB for basin means range from typically 10% in large, dry basins to 30% in wet and smaller coastal basins. Only in basin 1, located in Dronning Maud Land, do the maps of *Van de Berg et al.* (2006) and *Van den Broeke et al.* (2006c) differ outside of their uncertainty ranges, consistent with the fact that snowdrift and blowing snow sublimation are important processes in this region. To make matters worse, this basin is also poorly covered by observations.

For most dry basins (i.e. 1 to 12 and 20 to 24) the estimate of *Vaughan et al.* (1999) is close to or within the error margins of model estimated basin mean SMB. For basins 13 to 19, the absolute and relative error margins on the model estimated SMB are larger than for the drier basins. For example, the relative error margin for basin 13 is about 32%. Nevertheless, the estimate by *Vaughan et al.* (1999) for nearly all these basins is (far) below the lower range of model estimated SMB. Significant differences between model-estimated SMB and *Vaughan et al.* (1999) are also found for basins 8 and 9. These basins have rough topography, which makes both modeling and interpretation of observations more complicated.

Several basins (i.e. basins 8, 9, 14, 16 to 19 and 24) are less than twice the area of one independent model estimate. As a result, the error derived for the whole grounded ice sheet (GIS) or large regions of combined drainage basins is larger than the squared sum of the error estimates of the individual basins within the region of interest. For example, the squared sum of the errors in the total accumulation for whole GIS are 93 and 110×10^{12} kg per year for *Van de Berg et al.* (2006) and *Van den Broeke et al.* (2006c), respectively. As can be seen in Table 4.3, these numbers grow to 108 and 135×10^{12} kg per year, respectively, if basin SMB errors are not assumed to be independent.

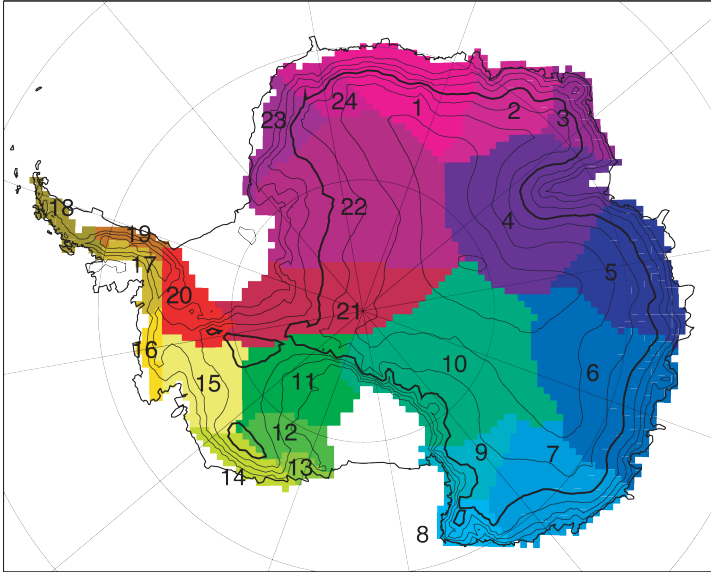


Figure 4.2: Basin definitions of Van den Broeke et al. (2006b). Elevation isopleths are drawn every 500 m, with the 2000 m isopleth drawn thicker.

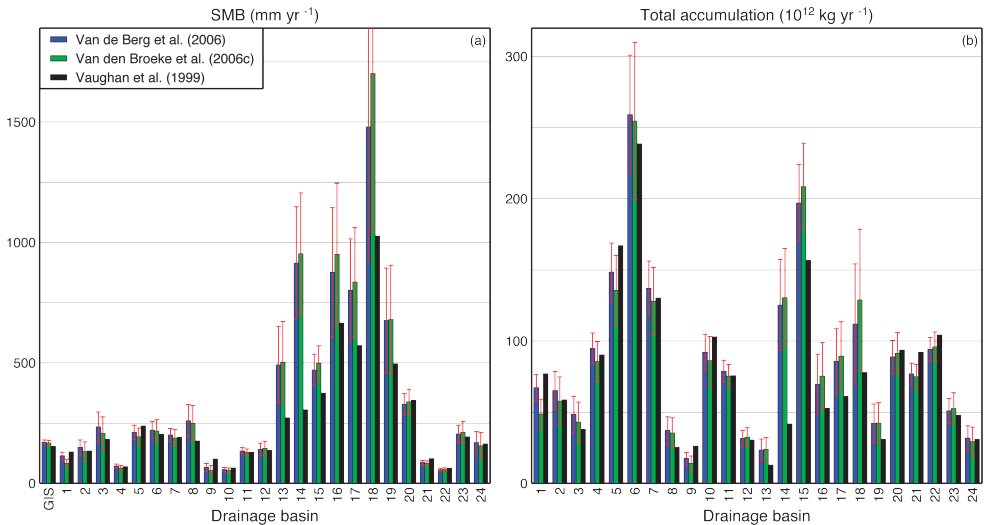


Figure 4.3: Basin mean of model estimated (a) SMB (mm per year) and (b) total accumulation (10^{12} kg per year), both with error margins. Basin definitions of Van den Broeke et al. (2006b) (Figure 4.2) are used, GIS is the grounded ice sheet.

Table 4.2: Area and statistical properties of the drainage basins. Basin definitions of Van den Broeke et al. (2006b) are used. AP, WA, EA and GIS denote the Antarctic Peninsula, West and East Antarctica, and the grounded ice sheet, respectively.

Basin number	Area (10^3 km 2)				n_{free}	
	V99	Total	RACMO2/ANT		vdBerg	vdBroeke
			<2000 m	>2000 m		
1	586	590	223	367	4.4	3.5
2	425	436	127	309	2.9	2.1
3	211	207	132	75	2.1	1.9
4	1320	1326	266	1060	7.8	5.1
5	710	699	254	444	5.2	4.1
6	1169	1171	270	902	7.2	4.9
7	684	683	271	412	5.2	4.2
8	156	143	107	35	1.6	1.5
9	263	264	76	188	1.8	1.3
10	1610	1606	161	1445	7.9	4.2
11	570	584	479	105	6.8	6.6
12	218	223	205	18	2.8	2.8
13	48	48	48	0	0.6	0.6
14	141	137	110	27	1.6	1.5
15	410	418	394	25	5.3	5.3
16	76	79	79	0	1.1	1.1
17	102	107	107	0	1.4	1.4
18	71	76	76	0	1.0	1.0
19	64	63	63	0	0.8	0.8
20	267	271	261	9	3.5	3.5
21	884	893	349	544	6.8	5.5
22	1676	1677	405	1272	10.5	7.3
23	248	248	179	69	2.6	2.5
24	190	188	75	113	1.4	1.2
AP		245	245	0	3.2	3.3
EA		9238	2547	6690	60.6	43.8
WA		2653	1925	728	28.4	26.9
GIS	12101	12136	4717	7419	92.3	73.9

Table 4.3: Results of the error in the SMB estimates per basin. Basin definitions of Van den Broeke et al. (2006b) are used. AP, WA, EA and GIS denote the Antarctic Peninsula, West and East Antarctica, and the grounded ice sheet, respectively.

Basin number	SMB (mm yr ⁻¹)			Total accumulation (10 ¹² kg yr ⁻¹)		
	V99	vdBerg	vdBroeke	V99	vdBerg	vdBroeke
1	129	114 ± 15	83 ± 8	76	67 ± 9	49 ± 10
2	144	150 ± 31	132 ± 39	61	65 ± 13	58 ± 17
3	188	234 ± 61	208 ± 68	40	48 ± 13	43 ± 14
4	66	72 ± 8	64 ± 11	87	85 ± 11	85 ± 14
5	225	213 ± 29	194 ± 35	160	149 ± 20	136 ± 24
6	210	221 ± 36	217 ± 47	246	259 ± 42	255 ± 55
7	192	201 ± 28	187 ± 35	131	137 ± 19	128 ± 24
8	189	260 ± 66	248 ± 74	29	37 ± 10	35 ± 11
9	97	66 ± 16	53 ± 20	26	17 ± 4	14 ± 5
10	64	57 ± 8	54 ± 11	103	92 ± 13	86 ± 17
11	131	135 ± 13	129 ± 14	75	79 ± 8	75 ± 8
12	127	141 ± 26	146 ± 29	28	32 ± 6	33 ± 6
13	285	493 ± 160	503 ± 168	14	24 ± 8	24 ± 8
14	313	915 ± 233	954 ± 251	44	125 ± 32	131 ± 34
15	382	471 ± 65	499 ± 72	156	197 ± 27	209 ± 30
16	679	876 ± 268	951 ± 295	52	70 ± 21	75 ± 23
17	584	801 ± 214	836 ± 226	60	86 ± 23	89 ± 24
18	579	1480 ± 557	1701 ± 656	41	112 ± 42	129 ± 50
19	497	676 ± 217	680 ± 226	32	42 ± 14	42 ± 14
20	345	328 ± 43	338 ± 53	92	89 ± 12	92 ± 14
21	101	86 ± 8	84 ± 10	89	77 ± 7	75 ± 8
22	63	56 ± 5	57 ± 6	106	94 ± 9	96 ± 10
23	196	206 ± 35	213 ± 45	49	51 ± 9	53 ± 11
24	168	169 ± 46	156 ± 54	32	32 ± 9	29 ± 10
AP		979 ± 205	1063 ± 234		240 ± 50	261 ± 57
EA		124 ± 7	116 ± 8		1145 ± 61	1067 ± 78
WA		261 ± 20	269 ± 23		692 ± 54	713 ± 61
GIS	149	171 ± 9	168 ± 11	1825	2076 ± 108	2041 ± 135

4.4 Discussion

A method to estimate the error margin on model estimated SMB is presented. First, an error margin is constructed for model estimated SMB in a single grid box, taking into account the uncertainty in the observations themselves. It is shown that the expression that results after optimization statistically explains the remaining differences between observations and model estimated SMB. Second, in order to properly average the SMB error margin over a basin, the auto de-correlation distance for SMB deviations is calculated. This is used to obtain the effective number of degrees of freedom in the basin under consideration, which yields the desired error margin for the basin-mean, model estimated SMB. As a pilot study we applied the method to the basins used in *Vaughan et al. (1999)* and *Van den Broeke et al. (2006b)*, using model estimated SMB from *Van de Berg et al. (2006)* and *Van den Broeke et al. (2006c)*.

A point of attention is the estimate of the observational error. As can be seen in Equation (4.3), larger observational errors reduce the errors in the model estimate. Analysis showed that neglecting the error in observed SMB increases the error margin for basin mean SMB by 15% on average; an increase of observational error by 50% reduces final error margins by 35% on average. In both cases, however, the optimized error distribution (c.f. Figure 4.1) matches the normal distribution less well than for the observational error used here, supporting the validity of the prescribed observational error estimate.

A second sensitive variable in the method is the auto decorrelation distance. For basins with n_{free} larger than one, the error estimate varies with one over the auto decorrelation distance. A robust estimate of the the auto decorrelation distance is thus important.

To conclude, the method described here uses all available SMB observations in order to provide an possible error estimate of model SMB that is as accurate and objective as possible. Furthermore, using Equations (4.2) and (4.5), it is straightforward to apply this method to any Antarctic drainage basin, from individual glaciers to the entire ice sheet.

Chapter 5

Heat budget of the East Antarctic lower atmosphere derived from a regional atmospheric climate model

Abstract

The heat budget of the lower East Antarctic atmosphere is calculated using output from a regional atmospheric climate model. The climatology of this model compares well with observations, although the surface energy budget shows an underestimation of the downwelling longwave radiation and an overestimation of the sensible heat flux. The winter atmospheric boundary layer over Antarctica is characterized by a strong surface inversion, due to longwave cooling of the surface. The longwave radiation loss is balanced by heat extracted from the atmosphere by turbulent mixing, which in turn is compensated by large-scale horizontal and vertical heat advection. Above the boundary layer, net longwave cooling is balanced by subsidence. In the coastal margin, latent heat release from condensation is a significant heat budget component. In summer, the surface is near radiative balance, resulting in a weak surface inversion. As a result, cooling by turbulent mixing and heating by advection in the atmospheric boundary layer are largely reduced. Absorption of shortwave radiation is a small heating source throughout the atmosphere, reducing the importance of advection above the boundary layer. Net longwave cooling and heating by condensation remain unchanged compared to winter.

This chapter has been published as: Van de Berg, W. J., van den Broeke, M. R. and van Meijgaard, E., Heat budget of the East Antarctic lower atmosphere derived from a regional atmospheric climate model (2007), *Journal of Geophysical Research*, 112, D23101, doi:10.1029/2007JD008613.

5.1 Introduction

Antarctica is covered by the largest ice sheet on Earth, and its sheer size permits it to create its own climate. The most prominent elements of the climate of East Antarctica are the near-surface temperature inversion of up to 30 K (Connolley, 1996), and the katabatic wind in the boundary layer (Parish and Bromwich, 1987). During winter, in the absence of solar radiation, both phenomena are most prominent and persistent.

The climate of the atmospheric boundary layer (ABL) of East Antarctica is mainly forced by the negative surface radiation budget, which cools the surface of the Antarctic ice sheet. This imbalance is largest during the polar winter night; the surface radiation budget becomes slightly positive during the short summer (Van den Broeke *et al.*, 2004a). Cerni and Parish (1984) explained the strength and depth of the inversion as a balance between net longwave emission and sensible heat transport. Over sloping surfaces, the cold near-surface air introduces a horizontal pressure gradient force, which drives the katabatic winds. Even over the gentle slopes of the East Antarctic plateau, the katabatic forcing is significant (Brost and Wyngaard, 1978). The near-surface winds are enhanced by the large-scale forcing, which is directed parallel to the katabatic forcing for most of East Antarctica (Van den Broeke *et al.*, 2002; Parish and Cassano, 2003b).

The heat budget governs the atmospheric temperature evolution. Several studies have addressed the momentum budget of the East Antarctic lower atmosphere (Van den Broeke *et al.*, 2002; Van den Broeke and van Lipzig, 2003), or specific aspects such as a pure katabatic flow (Renfrew, 2004). However, only few quantitative analyses of the heat budget have yet been provided. King *et al.* (2001) analyzed the components of the ABL heat budget in order to assess mixing parameterizations. Furthermore, Van As and van den Broeke (2006) deal with the heat budget of the summertime ABL over the Antarctic interior.

Analysis of the heat budget does not directly provide insight in the dependency of temperature on measurable quantities such as katabatic or large-scale wind speed, cloud cover and optical thickness. Rather, it provides the physical connection between these quantities and atmospheric temperature. For example, a change in cloud thickness would alter the net longwave cooling at that level, but also affects the surface radiative balance and thus reduces the cooling of the boundary layer by turbulent mixing.

In the ABL, the heat budget directly interacts with the surface energy budget, but it is also influenced by large-scale dynamical processes. Above the ABL, heat advection is a major driving mechanism. Significant heat advection on climatological time-scales requires persistent temperature gradients along the dominant wind direction, and these temperature gradients can only be maintained by other processes, such as longwave radiative cooling.

In this paper, we present the climatological heat budget of the lower East Antarctic atmosphere as estimated from output of an atmospheric climate model. In the end, these results can help explain temperature change in the Antarctic, as reported by Van den Broeke and van Lipzig (2004); Turner *et al.* (2005). However, the analysis of temporal changes in the heat budget is postponed to a forthcoming paper.

Although atmospheric heat budget terms could be directly measured in theory, it is unfeasible in practice. We therefore use output from a regional climate model to quantify the heat budget of the Antarctic lower atmosphere. Atmospheric models solve the heat budget equation in order to calculate the temperature evolution in time.

Here, we limit ourselves to mean winter and summer heat budgets over East Antarctica and the surrounding seas. In contrast to West Antarctica and the Antarctic Peninsula, East Antarctica has a rather uniform topography, allowing for a grouping of the heat budget terms in elevation bins over the ice sheet and distance bins over the coastal seas.

In the next section, a brief description of the model is given. In section 5.3, the heat budget is derived and calculation methods are presented. In section 5.4, the model climatology is evaluated. Section 5.5 presents the heat budget results, starting with the climatology of East Antarctica, and after that the winter and summer heat budgets.

5.2 Model description

For this study, model output is used from the regional atmospheric climate model RACMO2/ANT. This model is especially adapted for Antarctic conditions. It consists of the atmospheric dynamics of the High-Resolution Limited Area Model (HiRLAM), version 5.0.6. (Undén *et al.*, 2002) and the physical processes package from the European Centre for Medium-Range Weather Forecasts (ECMWF), cycle CY23R4 (White, 2001).

Several physical parameterisations within RACMO2/ANT have been changed to better represent Antarctic conditions. The snow albedo parameterisation of Van den Hurk and Viterbo (2003) was implemented. For freezing conditions, the albedo decay in this parameterization is diminished proportional with the fourth power of the temperature. As a result, the albedo of snow remains almost constant below -10°C . Furthermore, the surface roughness length for momentum was reduced (Reijmer *et al.*, 2004), and the expression presented by Andreas (1987) was applied to calculate the surface roughness lengths of heat and moisture over snow surfaces. A four layer snow model was added to improve subsurface heat fluxes into the snow pack. These adjustments and their positive effect on the boundary layer, together with the set-up of RACMO2/ANT, are described in Reijmer *et al.* (2005). Since that publication, a correction has been made to include fractional sea ice cover. Horizontal diffusion of moisture has been decreased by a factor of ten in order to reduce artificial uphill moisture transport (Lenderink *et al.*, 2003). Concentrations of CO_2 and other trace gasses have been varied following IPCC (2001). Erratic rain generation for sub-zero temperatures has been corrected, taking in account the additional energy release (Van de Berg *et al.*, 2006).

The integration with RACMO2/ANT has been performed with a horizontal resolution of ~ 55 km and 40 levels in the vertical, of which the lowest is about 10 m above the surface. The model employs a hybrid vertical coordinate. ECMWF Reanalysis (ERA-40) fields forced the model at the lateral boundaries and provided sea surface temperature and sea ice fraction. Model results prior to 1980 have been excluded from the analysis because of the reduced quality of ERA-40 in high southern latitudes (Bromwich and Fogt, 2004; Sterl, 2004; Van de Berg *et al.*, 2005). The model integration has been extended until the end of 2004 with lateral forcings and sea surface boundary conditions taken from ECMWF operational analysis.

We used a regional climate model for two reasons. Firstly, the model interior of RACMO2/ANT evolves freely without intermediate model re-initialisations, thus the model heat budget components all link to physical processes in the interior model domain. In contrast, intermediate model re-initializations or assimilation methods, as used in ECMWF products, have a systematic temperature effect. Although the heat budget still closes, this repre-

Table 5.1: List of used physical parameters and constants.

Symbol	Name	Unit
T	Temperature	[K]
θ	Potential temperature	[K]
p	Pressure	[Pa]
ρ	Density	[kg m ⁻³]
\vec{u}	3D velocity field	[m s ⁻¹]
u, v, w	cross-, along-slope and vertical wind	[m s ⁻¹]
c_p	Heat capacity of air	[J K ⁻¹ kg ⁻¹]
J	External heating term	[J s ⁻¹ kg ⁻¹]

sents an additional spurious heat budget term that has no physical meaning. Secondly, as discussed in the next section, flux profiles of numerous parameters are required for the analysis of the heat budget. The standard archived model output of global circulation models is insufficient in this respect for a heat budget analysis.

5.3 The heat budget

5.3.1 Derivation of temperature tendency equation

Conservation of energy in the atmosphere can be formulated as (Holton, 1992)

$$c_p \frac{dT}{dt} - \frac{1}{\rho} \frac{dp}{dt} = J. \quad (5.1)$$

Physical parameters and constants are listed in Table 5.1. The left hand side of equation (5.1) represents the adiabatic interaction between temperature and pressure, the right hand side represents diabatic processes. The local temperature tendency (LTT) and the resolved advection ($RAdv$) can be separated in the adiabatic interaction, since

$$\frac{dT}{dt} - \frac{1}{\rho c_p} \frac{dp}{dt} = \underbrace{\frac{\partial T}{\partial t} - \frac{1}{\rho c_p} \frac{\partial p}{\partial t}}_{LTT} + \underbrace{\vec{u} \cdot \left(\nabla T - \frac{1}{\rho c_p} \nabla p \right)}_{RAdv}. \quad (5.2)$$

An atmospheric model captures only flow patterns coarser than the model resolution: the advection simulated by a model thus only represents contributions from the large-scale flow. Within this resolved large-scale advection, ‘horizontal’ ($AdvH$) and vertical ($AdvV$) advection have been separated. ‘Horizontal’ advection is not calculated on levels of constant height, but along η -levels. The η -coordinate system was retained for this analysis, because of its favourable characteristic that low-level winds follow the surface, independent of the surface slope, while the free-atmosphere circulation, which tend to follow pressure levels, is mostly ‘horizontal’ too.

On the right hand side of equation (5.1), J represents external heating processes, numerical filtering (K) and small-scale heat advection. In the atmosphere, external heating processes are absorption of shortwave radiation (SWD), absorption and emission of longwave

radiation (LWD), and heat exchange by various water phase changes (Q) like condensation and evaporation or melt of precipitation. The radiation fluxes of shortwave and longwave are abbreviated to SW and LW , respectively.

Horizontal temperature variations with a length scale similar to the model resolution are numerically filtered, to prevent numerical instabilities. This diffusion K can be considered as implicit advection and consists of a ∇^4 filter; it is calculated in the model dynamics section.

The exchange of heat by sub-grid scale vertical air motion is parameterized in the model physics package. The ECMWF physics package makes a distinction between vertical turbulent mixing and convection. Turbulent mixing represents the exchange of heat between vertical levels and with the surface through the sensible heat flux (SHF). Sensible heat divergence (SHD) represents the local heating or cooling due to convergence or divergence of SHF . Convection represents transport of energy by rising air parcels in a conditionally unstable atmosphere and has no direct interaction with the surface. Similar to turbulent mixing, local heating or cooling by convection (CHD) represents convergence or divergence of the convective heat flux (CHF).

Summarizing, in our atmospheric model conservation of energy is expressed by the following heat budget equation

$$\begin{aligned} \frac{\partial T}{\partial t} - \frac{1}{\rho c_p} \frac{\partial p}{\partial t} = & -\vec{u} \cdot (\nabla T - \frac{1}{\rho c_p} \nabla p) + K - \frac{1}{\rho c_p} \frac{\partial SW}{\partial z} - \\ & - \frac{1}{\rho c_p} \frac{\partial LW}{\partial z} - \frac{1}{\rho c_p} \frac{\partial SHF}{\partial z} - \frac{1}{\rho c_p} \frac{\partial CHF}{\partial z} + Q, \end{aligned} \quad (5.3)$$

which is abbreviated in this paper as

$$\begin{aligned} LTT = AdvV & + AdvH + K + SWD + \\ & + LWD + SHD + CHD + Q. \end{aligned} \quad (5.4)$$

5.3.2 Calculation of individual terms

The heat budget terms in equation (5.4) are calculated using monthly averaged diagnostic model profiles of SW , LW , SHF , LHF and six-hourly model states of T , Q , p and cloud content. In order to validate the truncation to six-hourly intervals for advection and monthly intervals for the external heating processes, the outcome is compared to a one-year control run in which all temperature tendency terms were explicitly stored. Using the tendencies of the temperature and pressure, the resolved advection could be exactly determined. The resolved advection that is computed using six-hourly instantaneous wind, temperature and pressure fields, shows a good match with the control run. Consequently, large-scale energy transport owing to variability on time-scales shorter than six hours is found negligible.

The vertical profiles of SW , LW , SHF and CHF are derived from monthly accumulated profiles. The temperature change by Q is calculated afterwards using the vertical fluxes of solid and liquid precipitation and the temporal change and advection of cloud content. This estimate of Q is successfully validated with the control run, in which accumulated water phase change profiles have been stored. SWD , LWD , SHD , C and Q thus obtained, are found to agree with the temperature tendency for the control run, with two exceptions.

Energy fluxes induced by turbulent mixing at the top and base of stratiform clouds, usually occurring over the Southern Ocean, have not been included in the diagnostic output, which locally leads to an imbalance in the heat budget, but one that is always less than 1 K per day. Furthermore, during situations with strong winds and a very large downward SHF , the diagnostic flux exceeds the model flux near the surface. A maximum underestimation of 2 K per day is found near the surface in the escarpment zone.

Finally, diffusion (K) is determined as a residual. Analysis of the one-year control run shows that on longer time-scales, the contribution of K to the heat budget is only significant over steep terrain. Note that errors in the diagnostics of turbulent mixing, as described above, also leads to residuals in the heat budget, and thus contribute to the presented value of K . These occasions will be discussed.

5.4 Model evaluation

Heat budget terms do not represent directly observable quantities. Therefore, the calculated heat budget can only be evaluated indirectly, using observable quantities such as temperature, wind and surface radiation fluxes. Most meteorological observation sites are located along the coast of East Antarctica and the Antarctic Peninsula. West Antarctica and the East Antarctic plateau are nearly devoid of stations, as is the Southern Ocean.

A thorough evaluation of the model climatology is presented by *Reijmer et al. (2005)*. They compared RACMO2/ANT output with 10 m wind speed and 2 m temperatures measured at (automatic) weather stations, and radiosonde data of wind and temperature at Neumayer and South Pole stations. They concluded that near-surface winds and temperatures are well represented in RACMO2/ANT, and that the model performs better than ERA-40 in this respect. The model also represents the radiosonde data well. They did not observe a seasonal variation of the model performance.

The adjustments that have been added to the physics package of RACMO2/ANT since the study of *Reijmer et al. (2005)*, namely the reduction of horizontal moisture diffusion, the time varying of trace gas concentrations, and the correction of sub-zero rain generation, have an insignificant impact on model climatology. However, the inclusion of fractional sea-ice cover introduces a near surface temperature rise for the northern edge of the sea-ice extend of up to 8 K in early winter. It also improves the agreement with temperature records from coastal stations.

5.4.1 Temperature and wind

For this study, the surface and upper air temperatures have been compared with deep snow temperature, (automatic) weather station data and radiosonde data from *Turner et al. (2005)*, respectively. Observations locations are shown in Figure 5.1.

In Figure 5.2a, the model simulated annual mean surface temperature for 1980 to 2004 is compared with observed 10 m firm temperatures. At this depth, the temperature closely resembles the climatological mean surface temperatures. The model has a 1.7 K cold bias compared to these observations, but is otherwise well capable to capture the 45 K wide range of annual mean surface temperatures in Antarctica ($r = 0.996$).

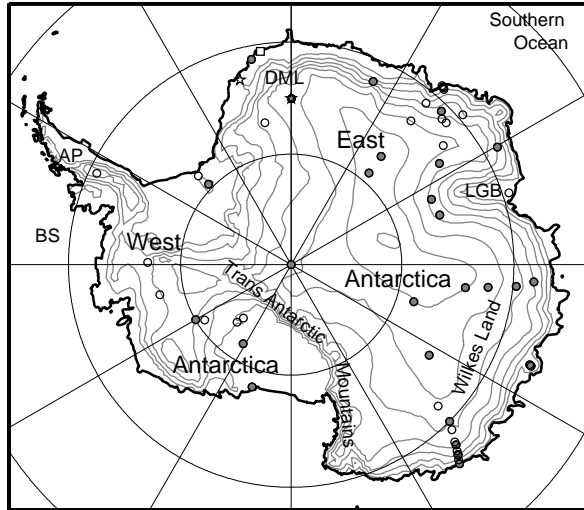


Figure 5.1: *Map of Antarctica. Grey lines are 500 m elevation contours. The Antarctic Peninsula, Bellingshausen Sea, Dronning Maud Land and Lambert Glacier Basin are abbreviated to AP, BS, DML and LGB, respectively. Macquarie Island is outside this map. The square locates Neumayer station, the left and right star locate AWS 4 and AWS 9, respectively. Circles mark the locations of 10 m firm temperature observations. A filled grey circle marks a wind speed observation.*

Figure 5.2b compares the model simulated and observed mean annual upper air temperatures at the 10 stations that have at least ten complete years of observations. The model free atmosphere temperatures have a cool bias of up to 2 K, with a maximum deviation at 700 hPa. This bias is acceptable in comparison to the temperature range of 50 K that occurs through the troposphere ($r = 0.999$). This bias is a winter and spring feature, i.e. from April to October; in summer and autumn a 1 K cool bias throughout the troposphere is found. The profile for Macquarie Island (158.9 °E, 54.5 °S) matches particularly well. This is because Macquarie Island is located in the lateral boundary zone of RACMO2/ANT, in which the model is adjusted to the reanalysis data that are directly affected by these observations through data assimilation.

Model simulated 10 m winds, presented in Figure 5.2c, also compare well with observations. The error bars of 1m/s represent the typical uncertainty in the observations; for the model value they represent the uncertainty in representativeness, since many of the observational sites are located in complicated terrain and model values need to be interpolated. In line with the conclusions of *Reijmer et al.* (2005), the model slightly underestimates the range in wind-speeds. Nevertheless, over the range of observations, the correlation between observed and model simulated wind speeds is very high ($r = 0.91$).

5.4.2 Surface energy budget

The surface energy budget (SEB) is evaluated using SEB observations on two automatic weather stations (AWS) in Dronning Maud Land (*Van den Broeke et al.*, 2005). AWS 4 is

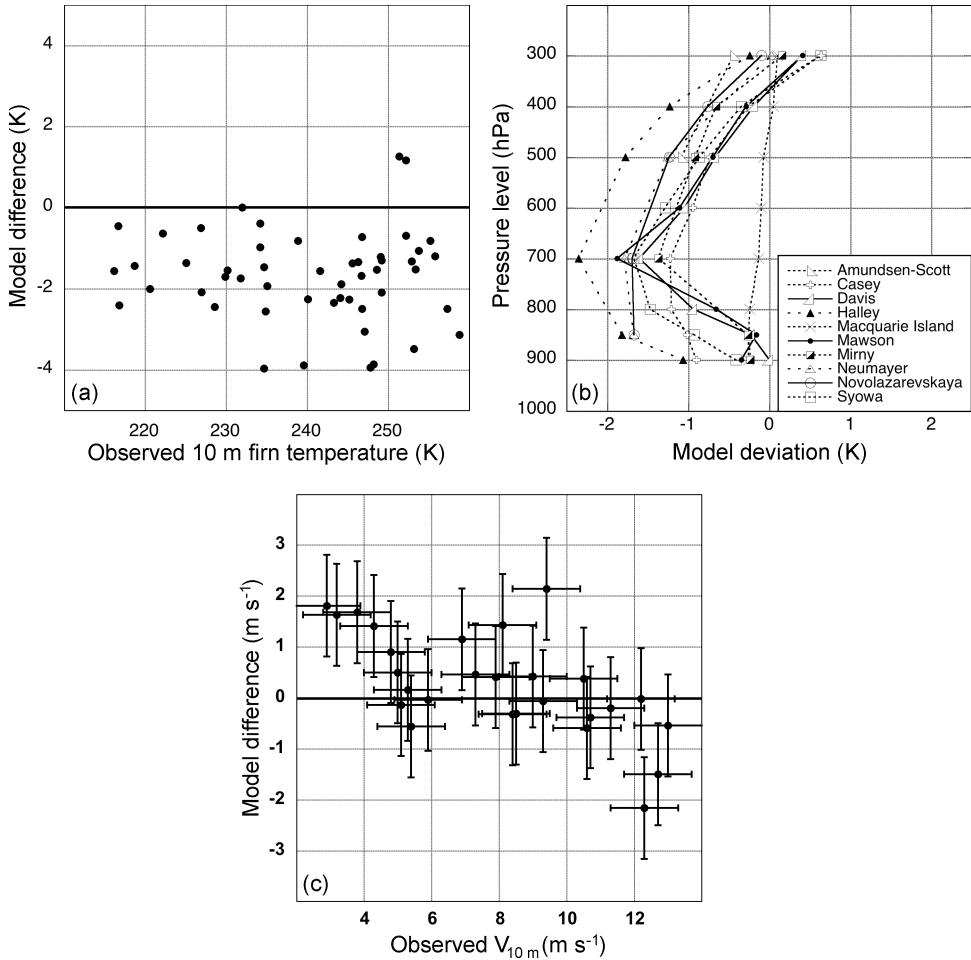


Figure 5.2: (a) Deviation of model simulated surface temperatures from observed 10 m firn temperatures. (b) Deviation of model simulated temperatures compared with radiosonde observations. The radiosonde data are from Turner et al. (2006). (c) Deviation of model simulated 10 m winds compared to observed 10 m winds at (automatic) weather stations. Automatic weather station wind speeds were assumed to be representative for 3 m, and adjusted to 10 m, using $z_{0,m} = 1$ mm and a neutral surface layer. Error bars give an impression of the uncertainty on the observations and model output.

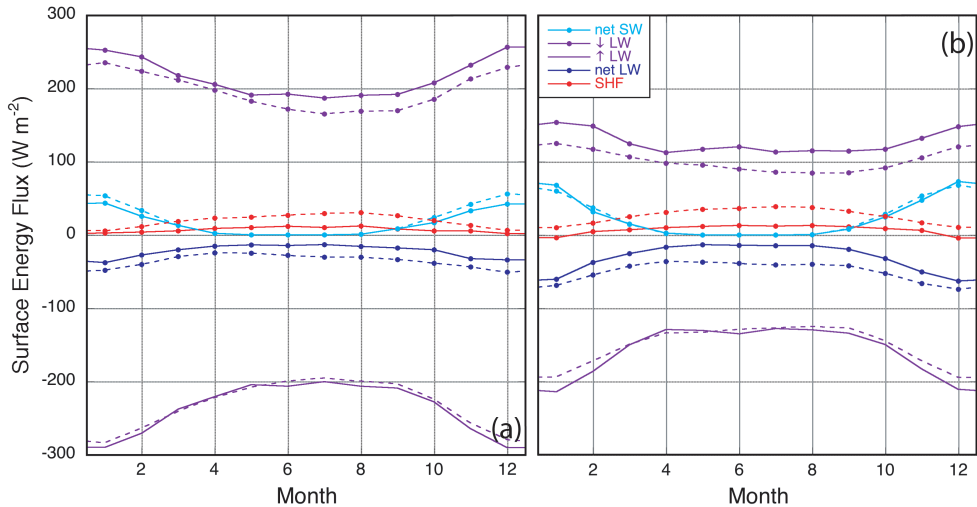


Figure 5.3: Comparison of surface energy fluxes from RACMO2/ANT (dotted lines) and observations (solid lines) at (a) AWS 4, situated at 72.75°S , 15.5°W , 34 m asl, and (b) AWS 9, situated at 75.0°S , 0.0°E , 2892 m asl. Fluxes are positive when pointing towards the surface.

situated on the Riiser-Larsen Ice Shelf (see Figure 5.1), 34 m asl, and AWS 9 is located near Kohlen base in the interior of East Antarctica, 2892 m asl. These observations have been chosen because they are located in relatively homogenous terrain and they represent two different climate zones of Antarctica. The observations are made in the period from 1998 to 2001. Figure 5.3 shows the comparison of observed SEB (solid lines) with model results for the same time span (dotted lines). The results show that RACMO2/ANT reasonably captures the main characteristics of the SEB, but has some significant biases.

Downwelling longwave radiation is underestimated by 10 to 30 W/m^2 throughout the year for both sites. *Guo et al.* (2003) found a similar underestimation and related it to an underestimation of humidity and cloud cover. The errors of both models show similarity, namely, a mid troposphere cool bias and underestimated precipitation on the plateau, which supports the assumption that the cloud parameterization contributes to the underestimation of downward LW . However, comparison of daily net LW against upgoing LW (not shown) indicates that also the LW radiation scheme contributes to the model flaw. AWS observations show that net LW is close to zero at cloudy days, while the maximum net LW emission for cloud free days is a function of the surface temperature (*Van den Broeke et al.*, 2004a, Figure 6). For the location of AWS 9, RACMO2/ANT estimates not only too few cloudy days, but RACMO2/ANT also overestimates net LW emission by 20 W/m^2 for cloud free days, which is likely due to the radiation scheme.

During winter, an excess downward SHF of 15 to 25 W/m^2 balances most of the excess LW cooling. During summer, excess LW cooling is partly compensated by overestimated downward SHF and SW absorption, and partly is introducing a cold surface temperature bias. If SHF is increased only in response to underestimated downwelling LW , the temperature bias should be largest during winter. The comparison with AWS data does not confirm

this. So, the mixing scheme is too active, which introduces a compensating error, resulting in only a small bias in the surface temperature. The net *SW* surface absorption at AWS 9 matches well because overestimated *SW* transmissivity is balanced by a slightly underestimated albedo.

How does this impact the atmospheric heat budget? The atmospheric heat budget and the SEB are closely related, because downwelling *LW* and *SHF* are largely from the ABL. The error margin shows that, although primary variables like temperature and wind are well simulated, *LW* and *SHF* parameterizations still need to be further improved for Antarctic conditions. However, we do not expect improved parameterizations to dramatically alter the results presented in this paper.

5.5 Results

5.5.1 Binning procedure

Vertical profiles of the heat budget terms have been binned in 500 m surface elevation intervals (Table 5.2) for the sector between 30 °W and 150 °E. This sector of East Antarctica excludes the Transantarctic Mountains and has a rather uniform topography, making binning meaningful. Over the coastal seas, binning has been done in 200 km distance intervals, excluding the lateral boundary zone. The heat budget terms are presented as temperature tendencies in K per day.

Over the ice sheet, wind vectors were rotated to obtain cross-slope and alongslope directions for u and v , respectively (Figure 5.4). Over sea, u and v follow the geographical coordinate system. For the analysis of the strength of the near-surface temperature deficit, a background temperature profile (θ_0) was extrapolated from the free atmosphere vertical potential temperature gradient towards the surface. Using this background profile, large-scale wind (u_{lsc}, v_{lsc}) profiles can be obtained assuming thermal wind balance with θ_0 , namely

$$\begin{aligned} \frac{\partial u_{lsc}}{\partial \ln p} &= + \frac{R_d}{f} \left(\frac{p}{p_0} \right)^{\frac{R_d}{c_p}} \frac{\partial \theta_0}{\partial y} \\ \frac{\partial v_{lsc}}{\partial \ln p} &= - \frac{R_d}{f} \left(\frac{p}{p_0} \right)^{\frac{R_d}{c_p}} \frac{\partial \theta_0}{\partial x}, \end{aligned} \quad (5.5)$$

in which $p_0 = 1013.25$ hPa. θ_0 , u_{lsc} and v_{lsc} have been calculated with monthly means.

5.5.2 Climatological setting

Figures 5.5a and 5.5b show the potential temperature (colours) and cross-slope wind profiles (contours) for winter (JJA) and summer (DJ), respectively, averaged for 1980 to 2004. Figures 5.5c and 5.5d enlarge Figures 5.5a and 5.5b near the surface, respectively. Vertical (colours) and alongslope (contours) wind speeds are shown in Figures 5.5e and 5.5f. In all these figures, the dotted lines indicate two η -layers for orientation and interpretation of the advection terms.

A prominent feature of the winter lower atmosphere over East Antarctica is the strong near-surface temperature deficit (Figures 5.5a and 5.5c). The potential temperature near the

Table 5.2: Characteristics of the bins, which contain the data from grid-points between 30°W and 150°E . DTC is the distance to the nearest coastal grid-point.

Bin no	Elevation / DTC	Bin name	Area (% of total)	Mean DTC (km)
1	>3750 m asl	High interior	1.7	-1245
2	3250-3750 m asl	Middle interior	10.8	-956
3	2750-3250 m asl	Low interior	13.9	-757
4	2250-2750 m asl	High escarpment	11.1	-544
5	1750-2250 m asl	Middle escarpment	5.6	-336
6	1250-1750 m asl	Low escarpment	4.1	-212
7	750-1250 m asl	High coastal	3.1	-134
8	150- 750 m asl	Middle coastal	2.7	-76
9	0- 150 m asl	Low coastal	2.3	-40
10	0- 200 km	Coastal sea	10.2	116
11	200- 400 km		11.3	306
12	400- 600 km		10.4	500
13	600- 800 km		7.7	693
14	800-1000 km		5.2	893

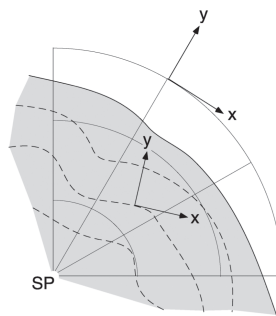


Figure 5.4: Orientation of the cross- (x) and along-slope (y) coordinates over the ice sheet, the dashed lines are schematic height contours. Over the ocean, ordinary W-E (x) and N-S (y) coordinates are used.

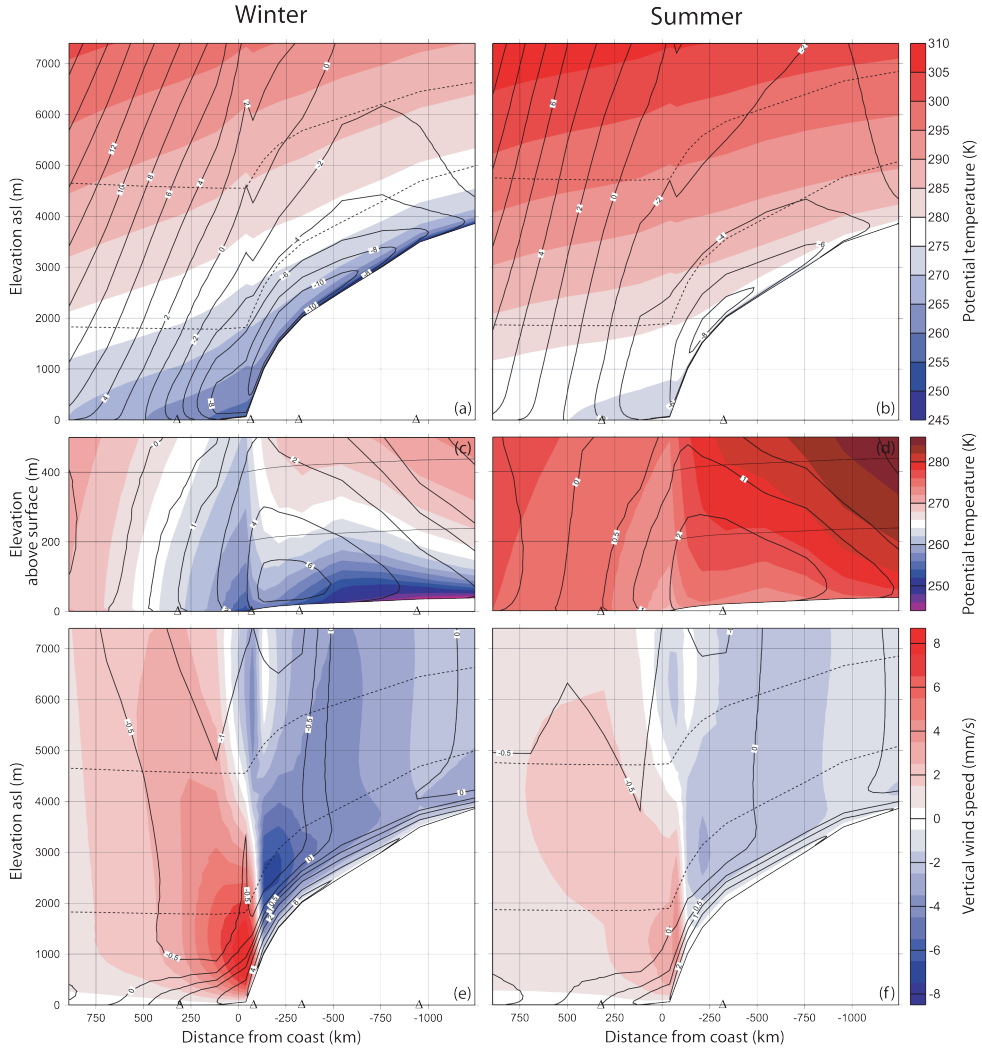


Figure 5.5: Bin average potential temperature (colours) with contours of cross-slope wind speed ($m s^{-1}$) for (a) winter, (b) December and January, i.e. summer. (c) and (d) Magnifications of the near surface potential temperature and alongslope wind ($m s^{-1}$) for winter and summer, respectively. The surface elevation is schematically included for orientation. (e) and (f) Bin average of vertical velocity (colours, $mm s^{-1}$, positive is upwards) and contours of alongslope wind speed ($m s^{-1}$) for winter and summer, respectively. In figures (a), (b), (e) and (f), dashed lines show η -levels for orientation. Triangles mark the positions of the presented profiles.

surface in the interior decreases below 250 K while the free atmosphere is close to 280 K (Figure 5.5c). In the free atmosphere the horizontal temperature gradient is large, typically 12 K/2000 km, forcing an eastward thermal wind of $2 \text{ m s}^{-1} \text{ km}^{-1}$. Thus the winds rotate from upper air westerlies to near-surface easterlies (Figure 5.5a). The katabatic enhancement in the ABL is clearly visible as an increased easterly wind. The wind preserves an along slope component in a shallow layer near the surface, due to friction (Figure 5.5e). Above the ABL, along slope winds are small and directed inland except in the far interior. Figure 5.5e shows large-scale subsidence ($w < 0$) above the ice sheet and upward motion ($w > 0$) over the adjacent ocean. The maximum in vertical velocity at the margin is due to the accumulation of cold air. During summer, the temperature gradients are smaller, and therefore the horizontal and vertical wind speeds are lower throughout the troposphere.

In Figures 5.5a and 5.5b, a discontinuity appears near the margin of Antarctica. This is a feature introduced by the binning procedure. The low coastal bin (0 - 150 m asl) contains ice-shelf grid points, and therefore is the only bin in which the grid-points are not evenly distributed along the coast of East Antarctica; ice shelves are located in coastal Dronning Maud Land and in the Lambert Glacier Basin. Both locations have lower temperatures and weaker westerlies than the coastal average.

In Figures 5.5e and 5.5f, an irregularity is visible in the vertical wind speed at some height above the coastal zone. This is related to diffusion, which damps small scale variations along η -levels. However, as η -levels partly follow the surface, an η -level contains elevation related temperature variations. Although the diffusion scheme corrects for the elevation, some persistent energy transport is nevertheless introduced in regions of steep topographic gradients. This transport is counterbalanced by advection, thereby introducing a secondary circulation. This circulation is negligible on synoptic time-scales as is its effect on climatological means of temperature and horizontal wind. However, it does have a significant influence on the average vertical wind speed, which is a diagnostic parameter in a hydrostatic model. As a result, the advective heat budget terms must be treated with caution in the higher atmosphere over the coastal zone of East Antarctica.

5.5.3 Winter heat budgets

In this section, the heat budgets of East Antarctica for winter, i.e. June, July and August, are presented for four representative bins: the interior, escarpment, coastal zone and coastal seas (Table 5.2).

Interior

Figures 5.6(a-c) show profiles for the middle interior bin, which is representative for all three interior bins. This bin has a surface temperature deficit of 27 K (Figure 5.6a). The temperature deficit layer is shallow; at 500 m above the surface the temperature deficit is reduced to only 3 K. The large-scale circulation is anticyclonic without a significant along slope component. In the ABL momentum budget, a balance is struck between the large-scale and katabatic pressure gradient force, turbulent surface drag and coriolis deflection (*Van den Broeke et al.*, 2002). Close to the surface, the along slope component matches the cross-slope component in size. At the top of the ABL, the wind is directed purely along the elevation contours.

The vertical profiles of turbulent sensible heat flux (SHF), net longwave radiation (LW), and convection heat flux (CHF) are shown in Figure 5.6b. Positive values indicate energy transport towards the surface. The flux of shortwave radiation is not included here in the absence of sunlight during winter. The surface net emission of LW is 36 W/m^2 , one third of the total emission at the top of the atmosphere. At the surface, all the lost energy in the form of longwave radiation is balanced by SHF , heating the surface and cooling the ABL. The flux of energy related to convection is negligible, as is expected in the very cold and stable ABL during the polar winter night.

The vertical divergence of the fluxes shown in Figure 5.6b determines the temperature tendencies in Figure 5.6c. In the ABL, SHD is the dominant cooling term. Higher up, cooling by longwave radiation is dominant. Near the surface, the cooling by LWD nearly vanishes, this cold layer is almost in radiative balance. The very stable and dry conditions over the plateau cause CHD and Q to be insignificant. Therefore, all heat that is lost by LWD and SHD must be supplied by advection. Over the whole column $AdvV$ is the main source of heating, although in the lower ABL $AdvH$ is a significant heating term too, caused by the strong decrease in the depth of the temperature deficit layer towards the interior in combination with a significant along slope wind (Figure 5.5c). Note that on long time scales $AdvH$ is insignificant in the free atmosphere heat budget, despite the fact that synoptic-scale systems like depressions do have a short-term impact on the temperatures through the whole troposphere (Van As *et al.*, 2005).

As concluded in section 5.4.2, SHD and LWD are prone to significant model uncertainties. For SHD this implies that the cooling strength and/or layer depth is overestimated, but because of its overwhelming modeled strength, SHD nonetheless is a dominant heat budget term in the ABL. In return, LWD cooling is somewhat underestimated, but it cannot be determined whether this additional cooling is spread out through the whole atmosphere or enhances the cooling maximum in the ABL.

Escarpment

The escarpment is characterised by increasing surface slopes. Furthermore, the plateau acts as a reservoir of cold air for the escarpment. Profiles for the middle escarpment, 1750 to 2250 m asl, are presented in Figures 5.6(d-f). Figure 5.6d shows that the katabatic winds are much stronger than in the interior, resulting in stronger vertical mixing and a thicker temperature deficit layer. The surface temperature deficit of 18 K is still considerable, and decreases more gradually with height than in the interior. Furthermore, the free atmosphere is about 5 K warmer than in the middle interior bin. Owing to increased baroclinicity, the prevailing winds change from easterly to westerly at a lower elevation. Above 2800 m asl, the winds also have a significant upslope component.

The vertical profiles of the energy fluxes (Figure 5.6e) are qualitatively similar to the middle interior. Again the surface net longwave emission is balanced by SHF , while CHF is negligible.

The katabatic nature of the ABL has a strong impact on the heat budget, as presented in Figure 5.6f. The increased depth of the ABL compared to the interior enables turbulent mixing to extract heat from a deeper layer, and therefore the maximum cooling rate by SHD

is less than half of that in the interior. Above the ABL, LWD remains the dominant cooling term, while subsidence ($AdvV$) is the dominant source of heat.

Contrary to the interior, $AdvH$ is significant, due to a significant alongslope wind in combination with horizontal temperature gradients (Figures 5.5c and 5.6d). In the lowest 150 m of the ABL, $AdvH$ cools the air by along slope advection of cold near-surface air from the interior. Surface friction maintains the along slope wind component, so its effect decreases quickly when moving away from the surface. Cold air descends the escarpment thus faster near the surface than in the upper ABL. The advection of this shallow, cold layer reduces the vertical temperature difference with the colder surface, but enhances the vertical temperature difference with the warmer upper ABL. As a result, the SHF at the top of the cold layer, which is further increased by the strong wind shear in the upper ABL, exceeds the SHF at the surface (Figure 5.6e), resulting in a reversal of the vertical SHF gradient and a heating of a shallow layer by SHD (Figure 5.6f), from now on referred to as SHF inversion layer. Analysis of the control year showed that about half of K can be attributed to SHD , which implies that SHF inversion might be even stronger.

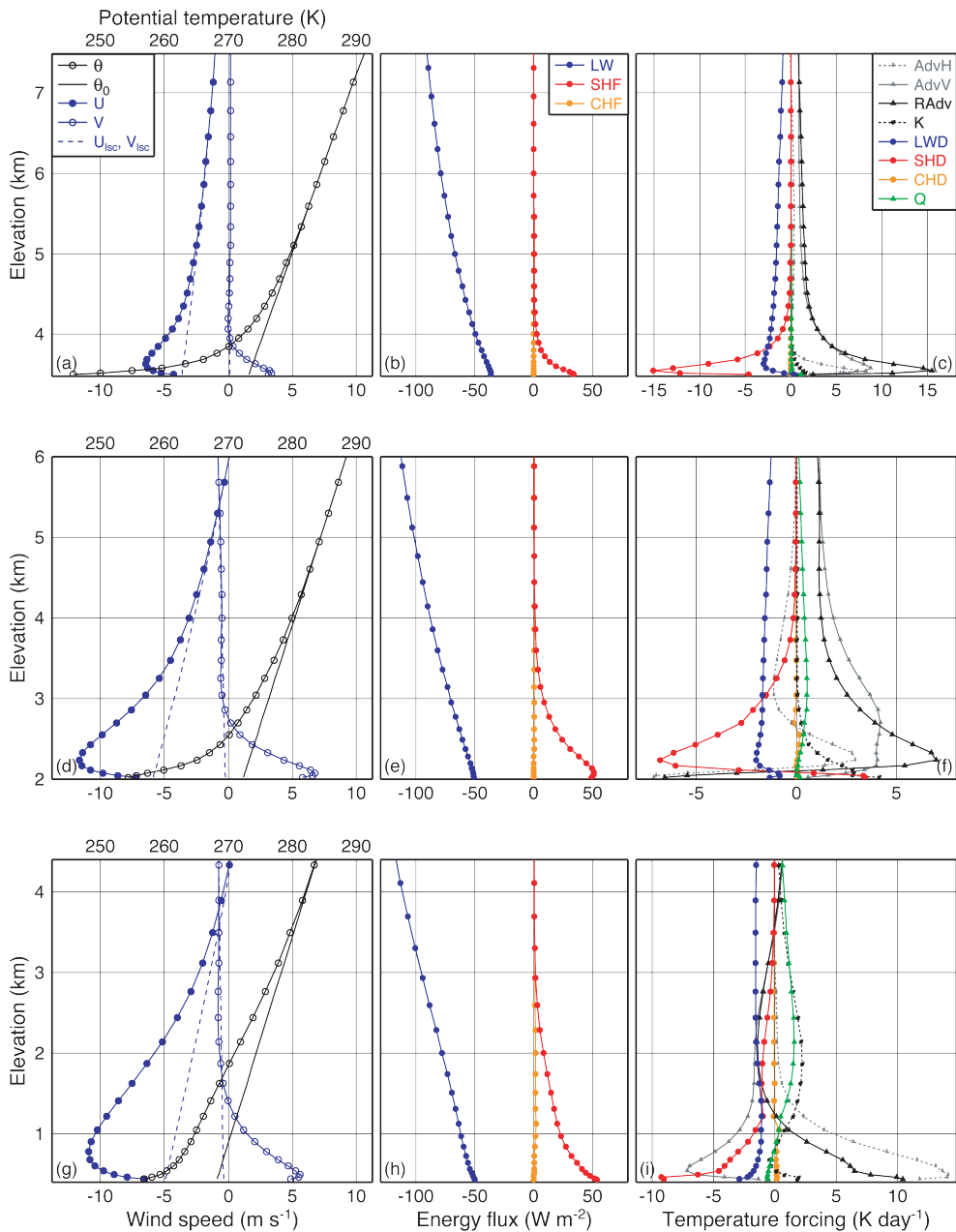
Owing to the deepening of the ABL, the temperature gradient along η -levels changes sign in the middle ABL, and $AdvH$ also becomes a heating term between 150 and 600 m above the surface. Above that level, the alongslope wind component becomes directed upslope (Figure 5.6d) so that $AdvH$ changes sign once more back to cooling. Finally, heating by condensation, represented by Q , gains importance while approaching the coast, but is still small.

The sign reversal of SHD from cooling to heating in a shallow near-surface layer is most pronounced in this transitional bin (~ 336 km inland) between interior and coast (Figure 5.7), but occurs throughout the whole escarpment (200 to 600 km inland). A preliminary analysis of the spatial occurrence of this SHF inversion layer indicates that it appears in places where the katabatic outflow has a long path over homogeneous terrain. For example, the whole margin of Wilkes Land exhibits a thick budget reversal layer, but SHF inversion layers rarely occur in Dronning Maud Land. The spatial variability of the ABL heat budget is the topic of a forthcoming paper.

We consider the SHF inversion layer as a realistic feature. The model simulated near-surface air potential temperature increases towards the coast in the escarpment (Figure 5.5c) agrees with observations (*Van den Broeke et al.*, 1999). Turbulent redistribution of heat in the ABL is the only mechanism that can provide enough heat to establish this temperature increase. $AdvV$, for example, quickly decreases in magnitude in the lowest 100 m because the vertical wind becomes zero at the surface.

Coastal zone

In Figures 5.6(g-i), profiles for the middle coastal bin (150-750 m asl) are shown. The elevation interval has been adjusted, so that the low coastal bin contains mainly grid-points on ice shelves (0-150 m asl) and the middle coastal bins mainly grid-points on grounded ice. The coastal margin is under oceanic influence, but still has similarities with more inland profiles. For example, the temperature deficit (Figure 5.6g) is strongest near the surface, but is also more vertically extensive, reaching up to about 2500 m asl, due to piling up of cold air seawards of the ice sheet on the ice shelves and sea ice. The wind still has a katabatic



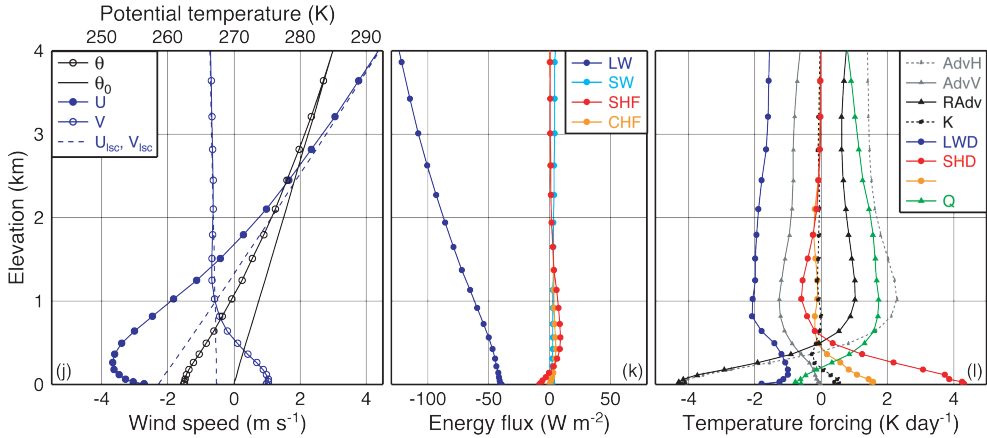


Figure 5.6: Winter vertical profiles for (a, b, c) the middle interior, (d, e, f) the middle escarpment, (g, h, i) the middle coastal bin and (j, k, l) the second sea bin 200 to 400 km offshore of (a, d, g, j) potential temperature (θ), background potential temperature (θ_0), cross-slope (U) and alongslope (V) wind, and their large-scale component (U_{lsc} , V_{lsc}), (b, e, h, k) LW, SW, SHF and CHF, (c, f, i, l) the heat budget terms.

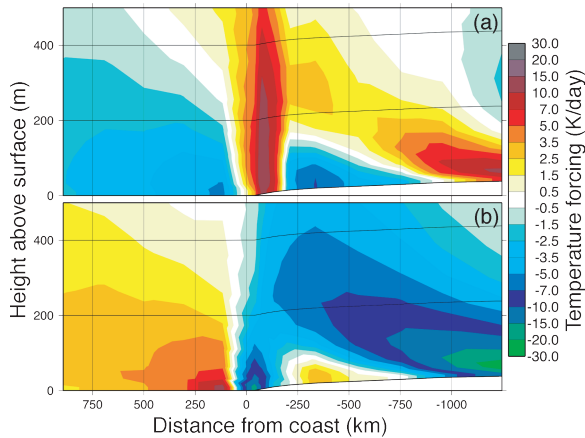


Figure 5.7: Bin winter averages of (a) AdvH and (b) SHD. The surface elevation is schematically included for orientation. Triangles mark the locations of the presented bins.

component and rotates in a 1500 m deep layer from its surface direction to cross-slope in the free atmosphere. The cross-slope wind reversal from East to West is located at 4300 m for this bin. The large-scale upslope wind is nearly equal to that in the middle escarpment, about -1 m/s.

The vertical profiles of the energy fluxes in the mid coastal bin (Figure 5.6h) again show that longwave cooling at the surface is compensated mainly by SHF . SHD (Figure 5.6i) is non-zero over a very deep layer and extracts energy from the air up to 2500 m asl, with the highest cooling rates near the surface. At the foot of the ice sheet, in the absence of katabatic forcing, the cold air from the ice sheet accumulates. The accumulation of air leads to upward motion and a negative $AdvV$, which cools the air together with LWD and SHD . As a result, the ABL potential temperature is lower than in the escarpment (Figure 5.5c), which turns $AdvH$ into a significant heating term in the lowest 1,5 km, which is also visible in Figure 5.7a.

In the cloud layer, between 1 and 5 km asl, heat release by water phase transitions (Q) is an important heat source. Diffusion (K), included in the model dynamics for numerical stability, is a heating term in the lower free atmosphere for the low and middle coastal bins, and a cooling term in this layer for the high coastal and low escarpment bins. No physical process can be directly linked to this model heat transport.

Coastal seas

The eleventh bin represents the seas surrounding East Antarctica from 200 to 400 km offshore (Figures 5.6(j-l)). The wintertime sea ice fraction for this bin is on average 0.79. The profile of the potential temperature (Figure 5.6j) reveals a 1500 m thick layer of cold air, which is made possible by the winter sea ice. Non-continuous sea ice, however, allows a significant ocean-atmosphere heat exchange, therefore a strong surface inversion does not build up. Winds are primarily large-scale driven. The meridional flow is southerly in the lowest 500 m and northerly above. The low-level southerly flow is forced by a combination of friction and cold air spreading out from the continental margin (Van den Broeke *et al.*, 2002). The zonal circulation is easterly in the lower atmosphere and changes to westerly above 1.5 km. As shown in Figure 5.5a, from 500 km offshore northwards, the flow is westerly throughout the atmosphere.

The vertical profiles of the energy fluxes for this bin are shown in Figure 5.6k. This area has a high cloud amount, which reduces the net emission of LW -radiation at the surface compared to the ice sheet. The open water fraction is a source of turbulent heat, i.e. a negative SHF . In winter, the flux of SW is non-zero at this latitude, but still insignificant.

The heat budget for this bin is shown in Figure 5.6l. Compared to bins over the ice sheet, the magnitudes are relatively small, because, unlike the ice sheet, the sea surface does not extract large amounts of heat from the atmosphere. As a result horizontal and vertical temperature gradients are smaller. $AdvH$, related to the outflow of cold air, is the dominant cooling term in the lowest 500 m, while SHD is the largest heating term. This heat is supplied by the upper part of the ABL and the ice-free sea surface part. Analysis shows that $AdvH$ and SHD budgets are larger over largely ice free locations compared to locations with almost full sea ice cover. Convection transports heat from the higher ABL downwards, since ascents are saturated-adiabatic and descents are dry-adiabatic. Q is negative near the

surface due to melt and evaporation of falling snow. The non-zero values of K in this bin do not represent diffusional transport but is related to the mixing in clouds, which have not properly been diagnosed during the model integration (see section 5.3.2).

Above the ABL, LWD and $AdvV$ are the most important cooling terms. Both have a maximum in the cloud layer, at about 1000 m. Below the clouds in the ABL, the net longwave emission is reduced. Above the ABL, the heat losses are balanced by CHF and $AdvH$. This balance reflects the influence of cyclones in the offshore Antarctic heat budget.

5.5.4 Summer heat budgets

In the Antarctic interior, December and January are the only summer months, because insolation already decreases significantly in February. Therefore, averages for these two months are considered representative for the summer period, starting in December 1979 and ending in January 2004.

Ice sheet

The summer heat budget profiles for the middle escarpment (1750-2250 m asl) (Figure 5.8c) are found representative for most ice sheet bins in East Antarctica.

The solar insolation is the principal difference between summer and winter. In summer, SW heating nearly balances the net LW cooling at the surface (Figure 5.8b). As a result, vertical potential temperature gradients are small and turbulent mixing extracts less heat from the ABL. The temperature deficit is strongly reduced and katabatic winds are weaker (Figure 5.8c). Both in the interior and the escarpment, the katabatic and large-scale forcing are of equal importance in the momentum budget of the ABL. The wind in the coastal zone of the ice sheet is even dominated by the large-scale forcing (Van den Broeke *et al.*, 2002).

The summer insolation resulting in a weaker katabatic nature of the ABL reduces nearly all terms in the heat budget (Figure 5.8c). This reduction, up to a factor five, is strongest in the interior (not shown). With the exception of the SHF inversion layer, which disappears in summer, the shape of the profiles is qualitatively similar to winter (c.f. compare to Figure 5.6f). The magnitudes of LWD and Q are similar to the winter profiles. The effect of clouds is especially important with respect to SWD at the same elevation. Evaporation of falling snow cools the lower ABL with a rate of up to 1 K per day of the coastal zone (not shown). Absorption of shortwave radiation SWD provides about half of the energy lost through longwave cooling. As a result of weaker θ gradients and weaker winds, $Adv + K$ is halved in summer compared to winter, whereby the ratios between $AdvH$, $AdvV$ and K do not change significantly.

Finally, CHF is significantly different from zero in the ice sheet summertime ABL. The ECMWF mass flux scheme, which parameterises convection, is activated if the ABL becomes near neutral during daytime. Since convection is bound by the top of the ABL, the extent of the non-zero CHF -layer indicates the maximum depth of the daytime ABL. In the interior (not shown) this is about 600 m; in the escarpment and coastal zone it is about 1400 m. These numbers are generally higher than values reported by observations (Mastrantonio *et al.*, 1999; Van As and van den Broeke, 2006), indicating that the ECMWF mass flux scheme is too active under these conditions.

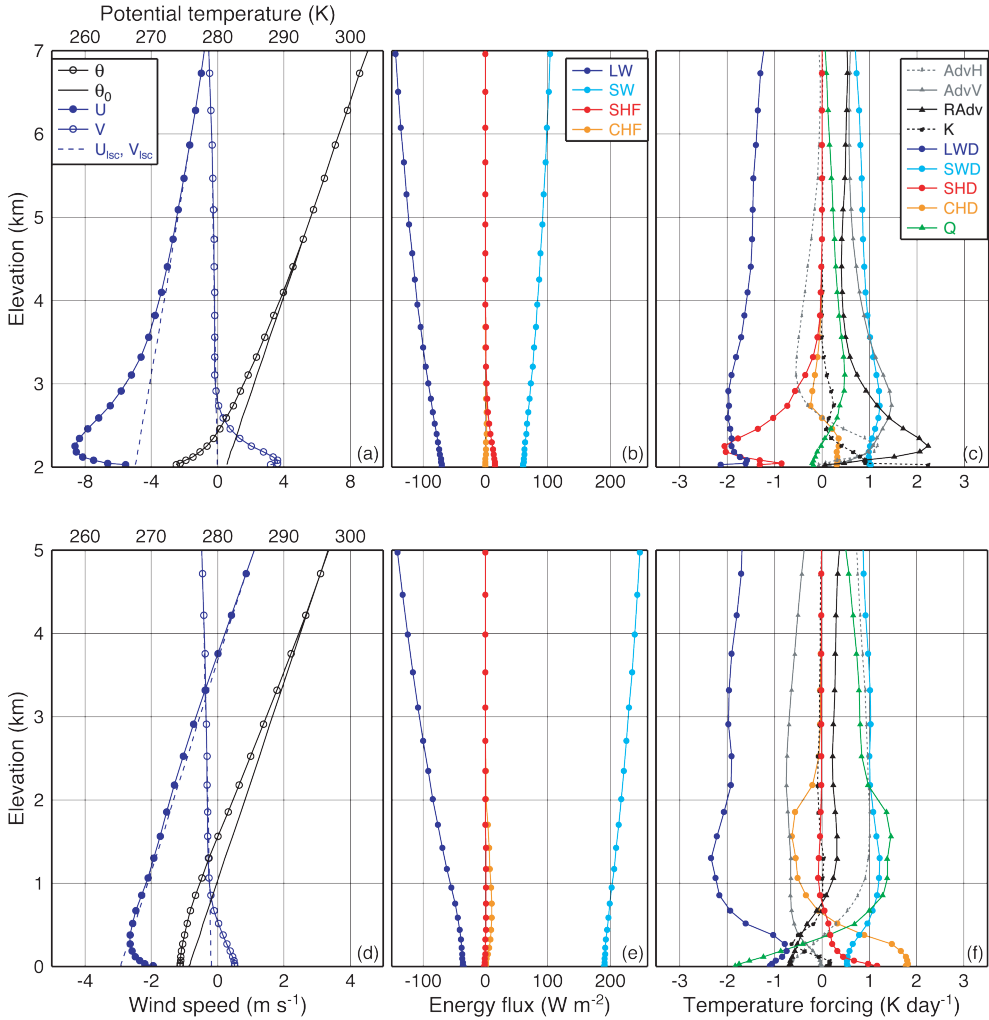


Figure 5.8: Summer vertical profiles for (a, b, c) the middle escarpment and (d, e, f) second sea bin 200 to 400 km offshore of (a, d) potential temperature (θ), background potential temperature (θ_0), cross-slope (U) and alongslope (V) wind, and their large-scale component (U_{isc} , V_{isc}), (b, e) LW, SW, SHF and CHF, (c, f) the heat budget terms.

Coastal seas

Figure 5.8(d-f) shows profiles for bin 11, 200 to 400 km offshore. These profiles are representative for the seas around East Antarctica. In summer, the effect of outflow of cold air from the continent on the temperature is small. A weak but vertically extensive potential temperature deficit (Figure 5.8d) is found for this bin. Diabatically forced lift is the likely cause of the increased stability of the lower atmosphere. The wind profile is primarily determined by the large-scale circulation.

The flux profiles over the sea (Figure 5.8e) are significantly different from those over land. Clouds strongly reduce the net LW emission at the surface, and the low ocean albedo enlarges the net surface SW insolation. CHF is larger than SHF , but both are small compared to the radiative fluxes.

Three layers can be distinguished in Figure 5.8f. The uppermost layer extends from 2 km upwards. This layer is not part of the ABL, since SHD and CHD are both zero. Cyclonic activity is evident from the large-scale upward motion (negative $AdvV$), the enhanced condensation, and the increased LWD and SWD due to the higher cloud amounts compared to the coastal bin (not shown). Although Q and SWD are significant heating terms, the free atmosphere experiences a net sink of heat, hence $RAdv$ is positive.

The middle layer extends from about 500 m up to 2 km. Here, the additional effect of ABL clouds (stratocumulus, shallow clouds) can be noticed. Convection itself removes some heat from the cloud layer, but that is compensated by additional condensation (Q). The profiles of LWD and SWD show that cloud tops experience strong longwave cooling and shortwave heating, while inside the cloud the radiation budgets are reduced.

The lowest 500 m represents the sub-cloud layer. Net LWD and SWD are reduced by the clouds. The downdrafts of the stratocumulus through CHF , absorption of sunlight (SWD) and the sensible heat uptake from the sea surface (SHD) are the dominant heating terms. Melt of snow and evaporation of precipitation have an important cooling effect. The non-zero value of K represents sub-cloud turbulent mixing and not numerical diffusion (see section 5.3.2). In this layer, $AdvH$ is negative due to weak remaining cold air outflow (Figure 5.8d). Further offshore, this term becomes zero (not shown).

5.6 Conclusions

A detailed analysis of the model simulated heat budget of the lower atmosphere over East Antarctica is presented, averaged in nine surface elevation bins over the ice sheet and five distance bins over the coastal seas.

Direct observations of the heat budget are not available, so the results shown here can only be indirectly evaluated by comparing model simulated and observed temperatures and surface energy fluxes at the surface. Over the ice sheet the model tends to overestimate the surface SHF and underestimate the down-welling LW flux. Possible reasons are an overactive mixing scheme and an underestimated cloud cover or atmospheric longwave emissivity. These errors counterbalance, so the surface temperature is found to match the observations well.

The wintertime Antarctic surface is cooled by net longwave emission, which is balanced by a sensible heat flux from the lower atmosphere. As a result, vertical turbulent mixing

is the dominant heat loss in the ABL, balanced by vertical and horizontal heat advection. In the interior, advection is mostly vertical through subsidence; near the coast, it becomes predominantly horizontal. In the escarpment, a shallow (< 100 m) near surface layer is found where turbulent mixing acts as a heat source, while horizontal advection cools. Above the ice sheet ABL, a balance is struck between longwave cooling and heating by subsidence. Heating by condensation is only important in the free atmosphere of the coastal zone.

In summer, the surface is in near-radiative balance, so that the horizontal and vertical potential temperature gradients are strongly reduced over the ice sheet and the coastal seas. As a result, cooling by turbulent mixing and advective heating are much smaller than in winter. Throughout the atmosphere, absorption of shortwave radiation is a heating term, but compensates only half of the longwave cooling. Above the ABL, advection is weaker than in winter, while condensational heating remains largely unchanged.

Apart from insight in the dynamics of the atmosphere, analysis of the heat budget elucidates the possible impact of inaccuracies of parameterizations on the model climate. The ECMWF parameterizations of clouds, longwave radiation and turbulent mixing still have flaws in the cold and stable atmosphere over the East Antarctic ice sheet.

Chapter 6

Factors Controlling the Near Surface Temperature in Antarctica

Abstract

Output from the regional climate model RACMO2/ANT is used to calculate the heat budget of the Antarctic atmospheric boundary layer (ABL). The main feature of the wintertime Antarctic ABL is a persistent temperature deficit compared to the free atmosphere. The magnitude of this deficit is controlled by the heat budget. During winter, transport of heat towards the surface by turbulence and net longwave emission are the primary ABL cooling terms. These processes show horizontal spatial variability on continental scales only. Vertical and horizontal advection of heat are the main warming terms. Over regions with convex ice sheet topography, i.e. domes and ridges, warming by downward vertical advection is enhanced due to divergence of the ABL wind field. Horizontal advection balances any excess warming caused by vertical advection, hence the ABL over domes and ridges tends to have a relatively weak temperature deficit. Conversely, vertical advection is reduced in regions with concave topography, i.e. valleys, where the ABL temperature deficit is enlarged. Along the coast, horizontal and vertical advection is governed by the inability of the large-scale circulation to adapt to small scale topographic features. Meso-scale (~ 100 km) topographic structures have thus a strong impact on the ABL winter temperature, besides latitude and surface elevation. During summer, this mechanism is much weaker; and the horizontal variability of ABL temperatures is smaller.

6.1 Introduction

Antarctica has an extraordinary atmospheric boundary layer (ABL) climate. During the austral winter, the lowest near-surface temperatures on Earth are observed here. The winter is ‘core-less’ and in the interior it lasts from April until the end of September. During winter,

This chapter has been published as: Van de Berg, W. J., van den Broeke, M. R. and van Meijgaard E. (2008), Spatial Structures in the Heat Budget of the Antarctic Atmospheric Boundary Layer, *The Cryosphere*, 2, 1-12.

the climate of the Antarctic ABL is determined by the absence of sunlight and the presence of the vast ice sheet. In the absence of sunlight, the net surface radiation balance becomes negative, creating a near surface temperature deficit, often referred to as ‘temperature inversion’. In this single aspect Antarctica is not unique as similar inversions are observed in Siberia during wintertime. However, over a sloped ice sheet surface, the temperature deficit layer sets up a katabatic force. Due to the vast extent of the ice sheet, the Coriolis force is dominant over inertia and friction, and the Antarctic katabatic winds are anti-cyclonic and nearly across-slope (*Van den Broeke et al.*, 2002). Superimposed on that, the presence of the ice sheet also introduces an anti-cyclonic large-scale circulation (*Parish and Cassano*, 2003a). In the austral summer, when the katabatic forcing is largely restricted to the nocturnal ABL, the topography maintains an anti-cyclonic circulation in the ABL.

Owing to friction, the ABL wind field over the ice sheet is on average divergent. The wind field in a steady state ABL must be divergent as long as the ABL is cooled by longwave radiation and sensible heat transport to the surface: the divergence of the ABL wind field initiates large-scale subsidence over the ice sheet. The meridional circulation of the Antarctic troposphere is thus characterized by a continental scale circulation cell. In spite of the continental scale of these ABL processes, 2 m potential temperature (Figure 6.1) varies on much smaller spatial scales. Near-surface temperatures are determined by the free atmosphere temperature, surface elevation and the ABL temperature deficit. As the free atmosphere temperature only varies on continental scales, this small scale variability must be due to differences in the ABL temperature deficit, and hence in its heat budget. Analysis of the heat budget provides a tool to understand the processes that control the near-surface temperature in Antarctica. Once we understand these processes, it will help us to understand how Antarctic ABL temperature might change in a future climate.

In this chapter, we present the heat budget of the Antarctic ABL as simulated by a regional atmospheric climate model. Only few studies on the atmospheric heat budget of Antarctica have been published up to now. *King et al.* (2001) analyzed the impact of different boundary layer parameterizations on modeled temperature tendency. *Van As and van den Broeke* (2006) quantified the heat budget of the summertime ABL at Kohnen station, Dronning Maud Land (DML); the geographical locations mentioned in this chapter are mapped in Figure 6.2. *Van de Berg et al.* (2007), Chapter 5 of this thesis, presented an analysis of the modeled heat budget of East Antarctica, but with a focus on vertical distribution and the dependency on elevation and distance to the coast. In this Chapter, we will focus on horizontal spatial patterns within the ABL over the entire ice sheet, thus including West Antarctica and the Antarctic Peninsula.

In the next section, a brief description of the atmospheric model is given. Then, in Section 6.3, the heat budget equation is formulated and a suitable ABL depth is defined. Next, the results for winter (JJA) and summer (DJ) are presented in Sections 6.4 and 6.5, respectively. This chapter ends with conclusions.

6.2 Model description and evaluation

The regional atmospheric climate model RACMO2/ANT is used for this study. This model consists of the dynamics of the limited area model HiRLAM, version 5.0.6 (*Undén*

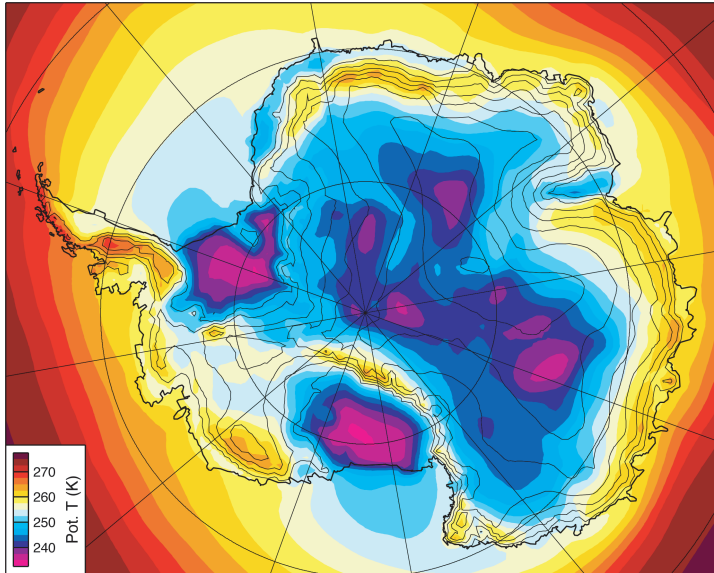


Figure 6.1: Winter (JJA, 1980-2004) 2 m potential temperature in K as simulated by RACMO2/ANT.

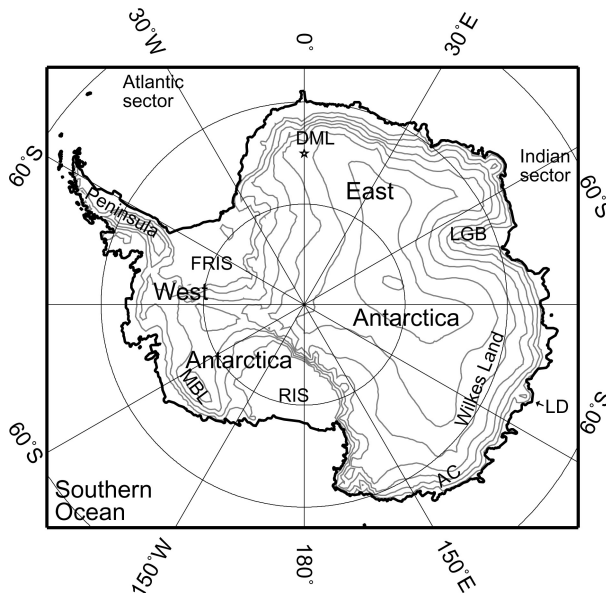


Figure 6.2: Map of Antarctica. The star locate Kohlen Station. DML, LGB, LD, AC, RIS, MBL and FRIS denote Dronning Maud Land, Lambert Glacier Basin, Law Dome, Adélie Coast, Ross Ice Shelf, Marie Byrd Land and Filchner-Ronne Ice Shelf, respectively.

et al., 2002) and the physics of the European Centre for Medium Range Weather Forecasts (ECMWF) model, cycle CY23R4 (White, 2001). The physics package has been adjusted to better represent Antarctic conditions, namely, a slower decaying snow albedo, reduced roughness lengths of heat and moisture, improved snow pack representation, time-dependent greenhouse gasses concentrations and enhanced generation of solid precipitation for freezing conditions. In the dynamics package the artificial horizontal diffusion of moisture has been reduced. During the model integration, the lateral boundaries of RACMO2/ANT are relaxed to six-hourly atmospheric states from ECMWF Re-Analysis (ERA-40) for September 1957 to August 2002. The integration is extended with ECMWF operational analyses until the end of 2004. Also, daily sea ice cover and sea surface temperature are taken from these sources. The interior of the model is allowed to evolve freely. Since the ERA-40 climatology prior to 1979 has insufficient quality in the Southern Hemisphere (Bromwich and Fogt, 2004; Sterl, 2004), only data from the period December 1979 until the end of 2004 is used here.

Reijmer *et al.* (2005) and Van de Berg *et al.* (2006, 2007) evaluated RACMO2/ANT output, and concluded that the model realistically simulates the climate of Antarctica, except that surface sensible heat fluxes and downwelling radiation fluxes over the ice sheet are over- and underestimated by about 20 W/m^2 , respectively. This model shortcoming should be kept in mind for in the remainder of this paper.

To assess the quality of the model simulated radiation, top-of-atmosphere (TOA) radiative fluxes are compared with observations from the International Satellite Cloud Climatology Project (ISCCP Zhang *et al.*, 2004). Figure 6.3 shows TOA net radiation observations and the simulated flux, for winter (JJA, a) and summer (DJ, b), both for the period 1983 to 2004.

During winter, modeled net radiation at TOA, which is predominantly determined by longwave (LW) emission, deviates less than 10 W/m^2 from observations over the ice sheet (Figure 6.3a). Over the Southern Ocean, the deviations are larger, caused by overestimated LW emission, while short-wave (SW) net insolation is well simulated. Deviations are larger over the ice sheet in summer (6.3b), mainly due to the underestimation of SW absorption by 30 W/m^2 . Simulated LW emission matches observations within 10 W/m^2 . Over the Southern Ocean south of 60° S , both SW and LW are well simulated. The results in 6.3a indicates that the net cooling/warming of the atmospheric column by radiation is well simulated during winter. Net summer TOA fluxes are less accurately simulated, and subsidence could therefore be found overestimated in summer.

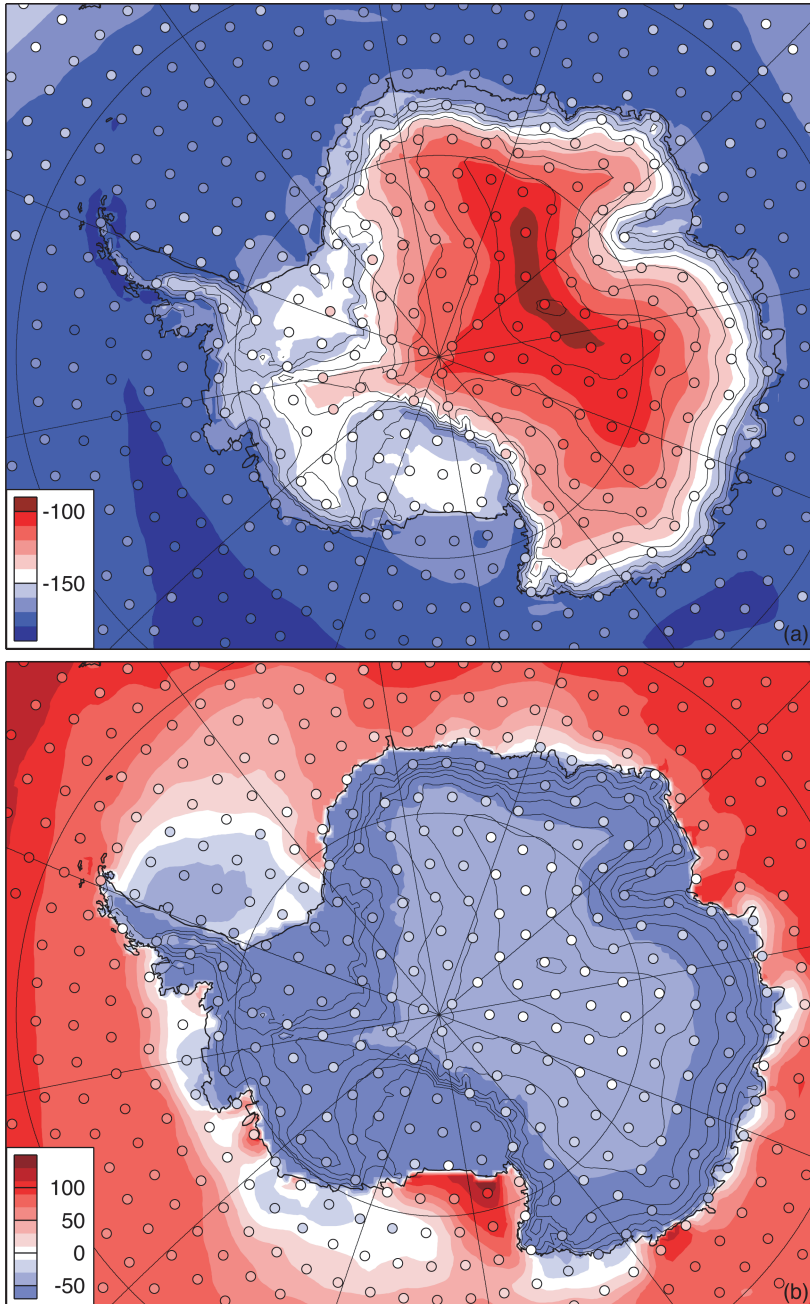


Figure 6.3: Comparison of observed (circles, Zhang et al. (2004)) and simulated TOA net radiative emission (W/m^2) for 1983 to 2004, for (a) Winter (JJA) and (b) Summer (DJ). Positive values indicate net fluxes into the atmosphere.

6.3 Methods

6.3.1 Definition of the heat budget

Van de Berg et al. (2007) presented the heat budget equation, which is

$$\underbrace{\frac{\partial T}{\partial t} - \frac{1}{\rho c_p} \frac{\partial p}{\partial t}}_{LTT} = - \underbrace{\vec{u} \cdot (\nabla T - \frac{1}{\rho c_p} \nabla p)}_{AdvH + AdvV} + K - \underbrace{\frac{1}{\rho c_p} \frac{\partial SW}{\partial z}}_{SWD} - \underbrace{\frac{1}{\rho c_p} \frac{\partial LW}{\partial z}}_{LWD} - \underbrace{\frac{1}{\rho c_p} \frac{\partial SHF}{\partial z}}_{SHD} - \underbrace{\frac{1}{\rho c_p} \frac{\partial CHF}{\partial z}}_{CHD} + Q, \quad (6.1)$$

where *LTT* is the local temperature tendency, i.e. the heat uptake due to temperature changes. On monthly time-scales *LTT* is a negligible contribution. *AdvH* and *AdvV* are the ‘horizontal’ and vertical heat advection, respectively. Both terms are calculated using six-hourly model states; they capture only heat advection on length scales that are resolved by the model. *AdvH* is derived along the hybrid η -coordinate of the model. The η -coordinate closely follows the topography in the atmospheric boundary layer (ABL) and is relaxed to pressure levels in the free atmosphere. *K* represents numerical diffusion that is applied for numerical stability. The external heating terms *SWD* and *LWD* represents the divergence of short-wave and long-wave radiation fluxes, respectively. Heating by divergence of the sensible heat flux (*SHF*) is indicated by *SHD*. Convective heat fluxes (*CHF*) are parameterized separately in RACMO2/ANT; *CHD* is heating by divergence of *CHF*. Finally, *Q* represents heating or cooling by various water phase changes like condensation, evaporation of falling precipitation or melt of falling snow. *SWD*, *LWD*, *SHD* and *CHD* are derived from monthly accumulated flux profiles of *SW*, *LW*, *SHF* and *CHF*, respectively. *Q* is derived from monthly precipitation fluxes, cloud content advection and temporal changes in cloud content.

The validity of this approach has been checked by using one year of model output in which the accumulated temperature tendency corresponding to numerical diffusion and physics, and the heating/cooling coming from water phase changes had all been explicitly stored. The calculated heat budgets are found to match these accumulated temperature tendencies well.

In the graphic presentation of ABL mean heat budgets hereafter, *K* has been included in *AdvV*. We did so because RACMO2/ANT is a hydrostatic model; vertical winds are thus not explicitly calculated. Numerical diffusion is required for model stability, but at locations where the slope of the topography changes, diffusion generates a secondary flow which is balanced by the vertical wind. As a result, vertical advection and diffusion show counterbalancing small-scale patterns that have no physical meaning. If *K* is added to *AdvV*, these patterns disappear. Since the numerical diffusion is derived as a residual, summing implies that we regard *AdvV* as a residual of all other processes. Another method to remove these patterns is by smoothing of *AdvV*, but it would give results similar to those presented here.

6.3.2 Definition of free atmosphere parameters

The background temperature (θ_0) is derived by downward extrapolation of the free atmosphere temperature gradient. The large-scale wind ($\vec{u}_{lsc} = (u_{lsc}, v_{lsc})$) is then derived by vertical extrapolation of the free atmosphere wind assuming a thermal wind balance with θ_0 , namely

$$\begin{aligned} \frac{\partial u_{lsc}}{\partial \ln p} &= + \frac{R_d}{f} \left(\frac{p}{p_0} \right)^{\frac{R_d}{c_p}} \frac{\partial \theta_0}{\partial y} \\ \frac{\partial v_{lsc}}{\partial \ln p} &= - \frac{R_d}{f} \left(\frac{p}{p_0} \right)^{\frac{R_d}{c_p}} \frac{\partial \theta_0}{\partial x}, \end{aligned} \quad (6.2)$$

with $p_0 = 1013.25$ hPa. θ_0 and \vec{u}_{lsc} are calculated on monthly means. The temperature deficit ($\delta\theta$) and the ABL wind ($\delta\vec{u}$) are defined as the deviation from the background temperature and large-scale wind, respectively.

6.3.3 Definition of ABL depth

There are many definitions of the depth of the stable ABL (*Stull*, 1988). Here we utilize a definition of the ABL depth that satisfies the following requirements:

- a) It should be large enough to include the main part of the temperature deficit layer, where θ deviates significantly, i.e. more than 1 K, from the free atmosphere θ_0 .
- b) It should be large enough to include the katabatic wind layer. As these winds are forced by $\delta\theta$, this is equivalent to a).
- c) It should include the turbulent layer, where *SHF* is nonzero.

RACMO2/ANT defines the depth of the ABL as the level where the bulk Richardson number reaches 0.25 of its surface value. These ABL depths are far below the typical temperature inversion and therefore too low for this application. Therefore, we introduced an alternative depth of the monthly mean ABL applying the transformation shown in Fig. 6.4a. Figure 6.4b shows the resulting mean wintertime (JJA) ABL depth. Typical ABL depths thus obtained range from 100 m on the East Antarctic plateau up to 1 km near the coast and over the Southern Ocean, which satisfies our criteria. In the remainder of this paper, we will present averages over this ABL depth.

6.3.4 Example of vertical profiles

Van de Berg et al. (2007) presented vertical profiles of the East Antarctic heat budget averaged in 500 m elevation bins. Figure 6.5 is an example of such profiles, it shows the winter (JJA) heat budget for the East Antarctic middle escarpment between 1750 and 2250 m asl. The horizontal green lines shows the mean ABL depth as used in this paper. Its depth is chosen such that it contains the layer that interacts most strongly with the surface. This elevation bin is characterized by strong katabatic winds and a deep temperature deficit layer (Figure 6.5a).

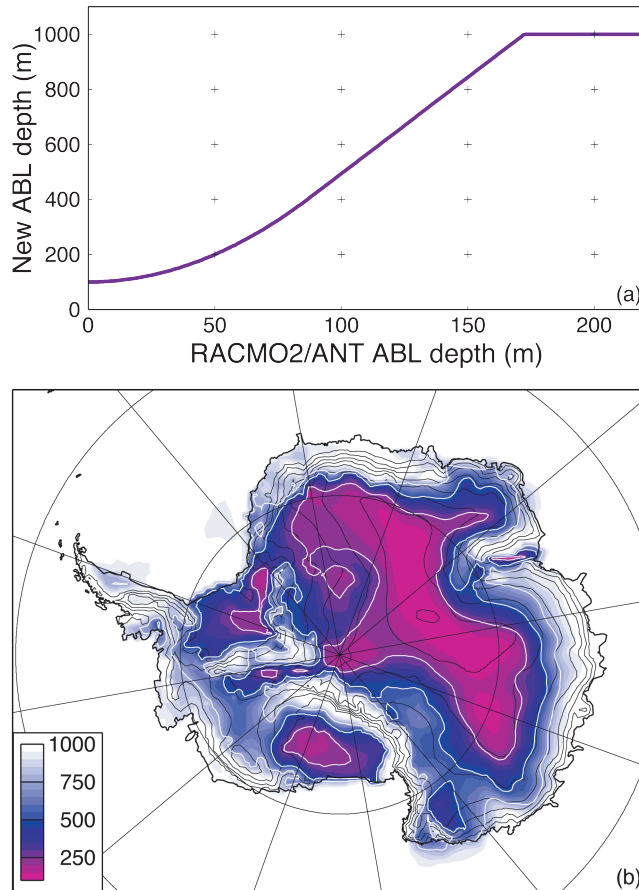


Figure 6.4: (a) Scaling function from RACMO2/ANT ABL depth to new ABL depth. (b) Average wintertime ABL depth in m.

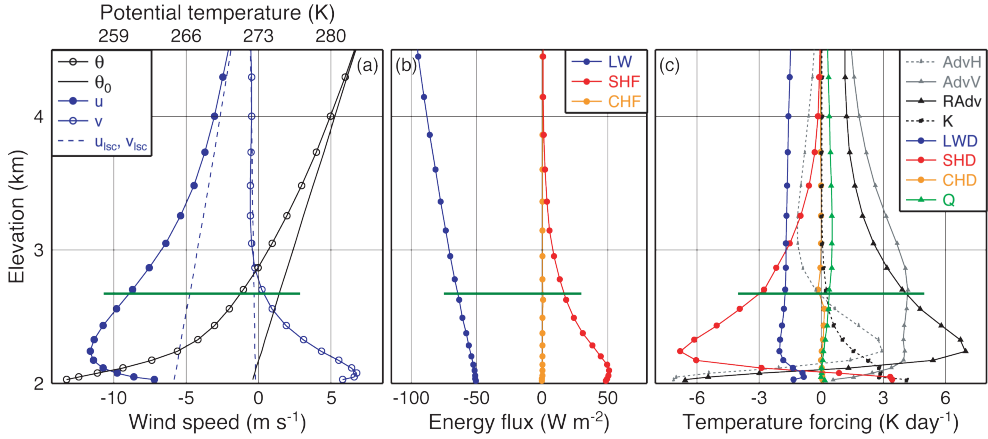


Figure 6.5: Winter (JJA) vertical profiles, binned for the middle escarpment of East Antarctica (1750 and 2250 m asl) of (a) potential temperature (θ), background potential temperature (θ_0), cross-slope (u) and alongslope (v) wind, and their large scale components (u_{lsc} , v_{lsc}), (b) LW, SHF and CHF, (c) the heat budget terms. Radv is the sum of AdvV and AdvH. The horizontal dark green line in (a), (b) and (c) indicates the average depth of the ABL for this bin.

The surface energy budget (Figure 6.5b) is a simple balance between net longwave radiation emission and SHF that is directed towards the surface. Figure 6.5c shows the resulting profiles of the heat budget components, which is remarkably complex. Cooling of the ABL occurs primarily by LWD and SHD. This cooling is mainly compensated by AdvV and to a lesser extent by AdvH. Noteworthy is the sign reversal of AdvH and SHD in the lowest approximately 100m, related to the downward transport of cold air from the plateau (Van de Berg *et al.*, 2007). K is separated from AdvV in this figure only.

6.4 Results: Winter

6.4.1 External heating and surface interactions

Figure 6.6 shows winter (JJA) ABL forcings by SHD, LWD and Q. Of those three, SHD is the dominant cooling term. At the surface in Antarctica, SHF approximately balances net LW cooling. This heat is extracted from the ABL. In the interior of East Antarctica, the ABL is shallow (Figure 6.4b). The divergence of SHF, thus cooling by SHD, is therefore largest in these regions, typically 10 K per day (Figure 6.6a), even though the surface flux is relatively small, typically 30 W/m². Near the coast, the ABL is deeper, forcing SHD cooling rates to be low in spite of the larger surface value of SHF.

The ice free part of the Southern Ocean acts as an enormous source of sensible heat during winter, inducing a positive SHD. Closer to the continent, a persistent and near-complete sea-ice cover isolates the atmosphere from the warm ocean water, so SHD is strongly reduced or becomes even slightly negative in the sea ice zone, but still remains less than -0.8 K per day.

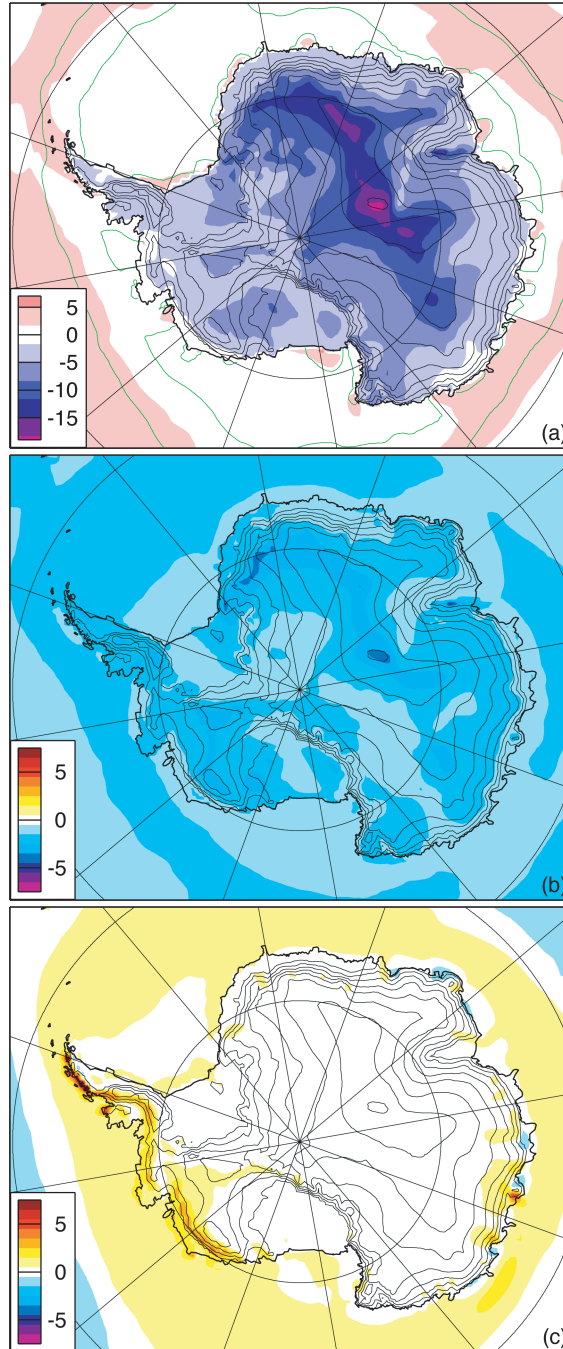


Figure 6.6: Average winter ABL temperature forcing by (a) SHD, (b) LWD and (c) Q in K per day. 20 and 90% sea ice cover isopleths are drawn in green in (a).

Cooling of the ABL by LWD (Figure 6.6b) is generally one order of magnitude smaller than by SHD . Maximum LWD cooling rates are found over the domes of East Antarctica, where the ABL is shallow. On the domes, the surface temperature deficit is large, but decreases steeply with height. As a result, the top of the ABL is warmer in absolute sense than the free atmosphere above and the surface below, which explains the relatively large cooling rates. Locations with a deep ABL have in general least cooling by LWD , because at these points the temperature maximum is less outspoken.

Figure 6.6c shows that Q is generally insignificant over the main ice sheets in Antarctica. Exceptions are those regions with high precipitation rates, namely, the west coast of the Antarctic Peninsula, coastal Marie Byrd Land and the east side of Law Dome in Wilkes Land. Heating by condensation is also a discernible heat source in the ABL of the Southern Ocean. Further north the melt of falling snow becomes dominant, and Q becomes negative.

The contribution of CHD to the heat budget (not shown) is very small during winter. It warms the ABL by up to 2 K per day over the ice-free ocean, elsewhere its contribution is near-zero.

As noted in Sect. 6.2, surface downwelling LW radiation and SHF are under- and overestimated by RACMO2/ANT, respectively. This implies an overestimation of the cooling of the ABL by SHD . Since most of the downwelling LW at the surface is emitted by the ABL, and LW fluxes at the top of the atmosphere (TOA) are found to match well with observations, the underestimation of the TOA-to-surface LW divergence probably implies an underestimation of cooling of the ABL by LWD . Model errors in LWD and SHD therefore partly balance in the heat budget.

6.4.2 Heat advection in East Antarctica

From the previous section it is clear that the energy extracted from the ABL by SHD and LWD must be balanced by horizontal and vertical heat advection. The spatial variability of the *total* heat advection in the ABL ($AdvH + AdvV$, not shown) is only significant on continental scales. This must be so, since SHD , the main ABL heat sink, is also spatially smooth (Figure 6.6a). Evidently, the inner product of the 3D wind field with horizontal and vertical temperature gradients determines the magnitude of the heat advection. In order to better understand the more complicated regional patterns of $AdvH$ and $AdvV$, vertical profiles averaged for East Antarctica are discussed first in this section.

Figure 6.7 shows average profiles of potential temperature, along-slope and vertical wind, horizontal and vertical advection for East Antarctica (30° W- 150° E). The surface temperature deficit is a prominent feature of the ABL in East Antarctica (Figure 6.7a) and it is strongest in the interior. Note that height is given as m above the *surface* level. As a result, the rise of the free atmosphere potential temperature towards the interior is due to increasing surface elevation in a stably stratified atmosphere. If one follows a constant elevation level, the potential temperature would decrease gradually towards the interior.

$AdvV$ (Figure 6.7b) is the main heating term in the atmosphere over the interior of East Antarctica through subsidence ($w < 0$, contours in Figure 6.7b). Warming by $AdvV$ extends all the way downwards to the surface, which indicates that the ABL wind field over East Antarctica is divergent on average. This is in line with the general picture of katabatic outflow. The largest heating rates are found in the interior, a result of the strong vertical temperature

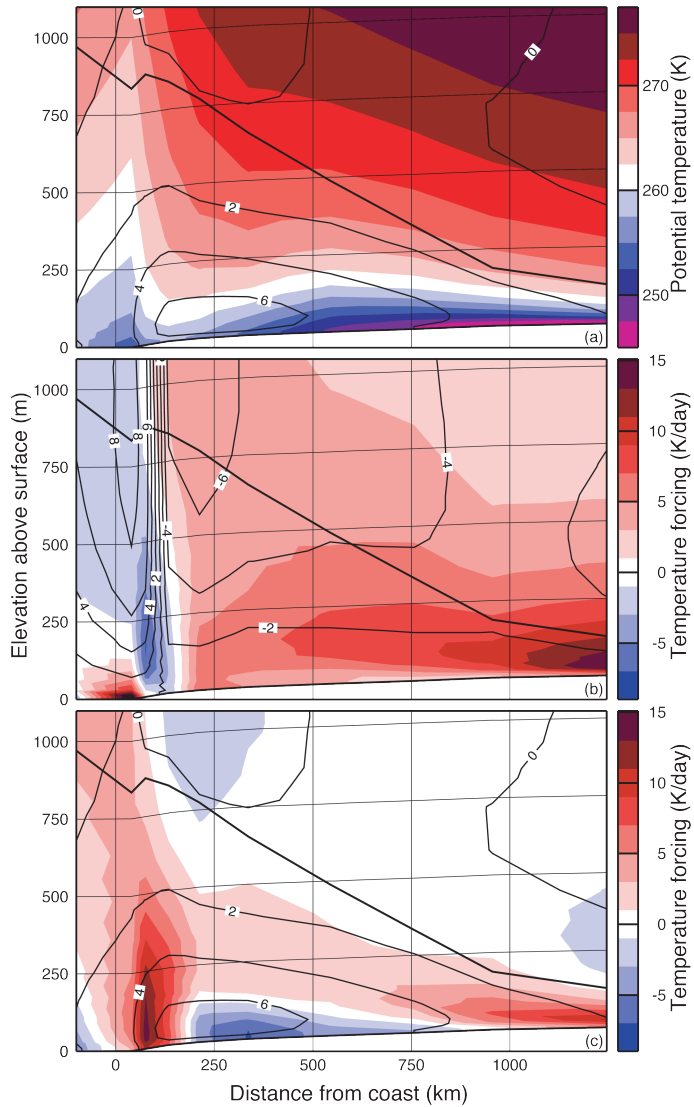


Figure 6.7: Mean winter profiles for the East Antarctic sector between 30°W and 150°E . (a) potential temperature (colors in K) and along-slope wind (contours, m/s); (b) AdvV (colors, K per day) and vertical wind (contours, mm/s); (c) AdvH (colors, K per day) and along-slope wind (contours, m/s). In all three figures, the surface elevation is schematically included for orientation. The thick black line represents the average ABL depth.

gradients in the ABL. Over the coastal slopes of East Antarctica, upward motion is found on average, due to piling up of out-flowing cold air. The near surface warming at the ice sheet margin is related to the persistently large temperature difference between the ice shelf and the ocean.

The $AdvH$ patterns (Figure 6.7c) mainly reflect the changes in the depth and temperature inversion strength in the ABL. The wind has a significant friction-driven downslope component in the ABL (*Van den Broeke and van Lipzig, 2003*), with maximum values near the surface about 250 km inland. Warming by $AdvH$ is related to the deepening of the inversion layer. This process is important in the interior and the upper part of the coastal ABL. In the escarpment, $AdvH$ becomes a cooling term near the surface, where strong vertical turbulent mixing driven by katabatic wind reduces vertical temperature gradients in the ABL. This reverses the near-surface horizontal temperature gradient compared to the interior. Averaged over the depth of the ABL, upper-level heating and low-level cooling by $AdvH$ thus partly cancel in the escarpment (see also Figure 6.5c). Cold air accumulates at the foot of the continent, because the katabatic force vanishes over the flat sea ice surface. Here, $AdvV$ cools the air by rising motion. As a result, the katabatic outflow from Antarctica is relatively warm, which drives the strong heating by $AdvH$ in this region.

6.4.3 Spatial distribution of $AdvH$ and $AdvV$

Figure 6.8 shows potential temperature and wind (a), $AdvV$ (b) and $AdvH$ (c) averaged over the ABL depth. The magnitudes of $AdvV$ and $AdvH$ clearly exceed those of the other heat budget terms in Figure 6.6. Superimposed on the continental-scale advection processes described in the previous section, surprisingly fine-scale spatial patterns are visible. These are topographically induced, and can be explained as follows: The ABL mean wind (Figure 6.8a) generally follows the ice sheet height contours, but the curvature of the elevation contours has a distinct impact on the relative wind direction. Convex elevation contours, at domes and ridges, for example, at 135° E, 70° S, enhance horizontal divergence of the ABL wind field and promote downward vertical motion. Figure 6.8b clearly shows that in the interior East Antarctica, ridges and domes have maximum heating rates by $AdvV$. Conversely, concave elevation contours, for example at $0-30^\circ$ E, 82° S, induce a converging ABL wind field and enhance upward motion. As Figure 6.8b shows, this effect is strong enough in some places to change subsidence into upward motion, making $AdvV$ a cooling term. $AdvV$ reaches its extreme positive values in valleys and ridges with length scales of 100 km, which is the minimum length that is properly resolved by the model grid.

Figures 6.8b and 6.8c show that $AdvV$ and $AdvH$ counterbalance in many regions. The primary reason is that $AdvH$ tends to remove temperature gradients that are generated by $AdvV$. As a result, locations with distinct convex topography have a large negative $AdvH$, for example 60° E, 70° S. For the same reason, maximum heating rates by $AdvH$ are found at concave topography, for example $0-30^\circ$ E, 82° S. Furthermore, positive $AdvH$ values are found where the ABL flow is pointed southwards (e.g. Southern DML) or into ice shelves. Although the topography of DML is convex, no large-scale cooling by $AdvH$ is found here. It shows that cooling by $AdvH$ requires an upstream reservoir of cold air. In contrast to most of East Antarctica, such a reservoir is absent in DML.

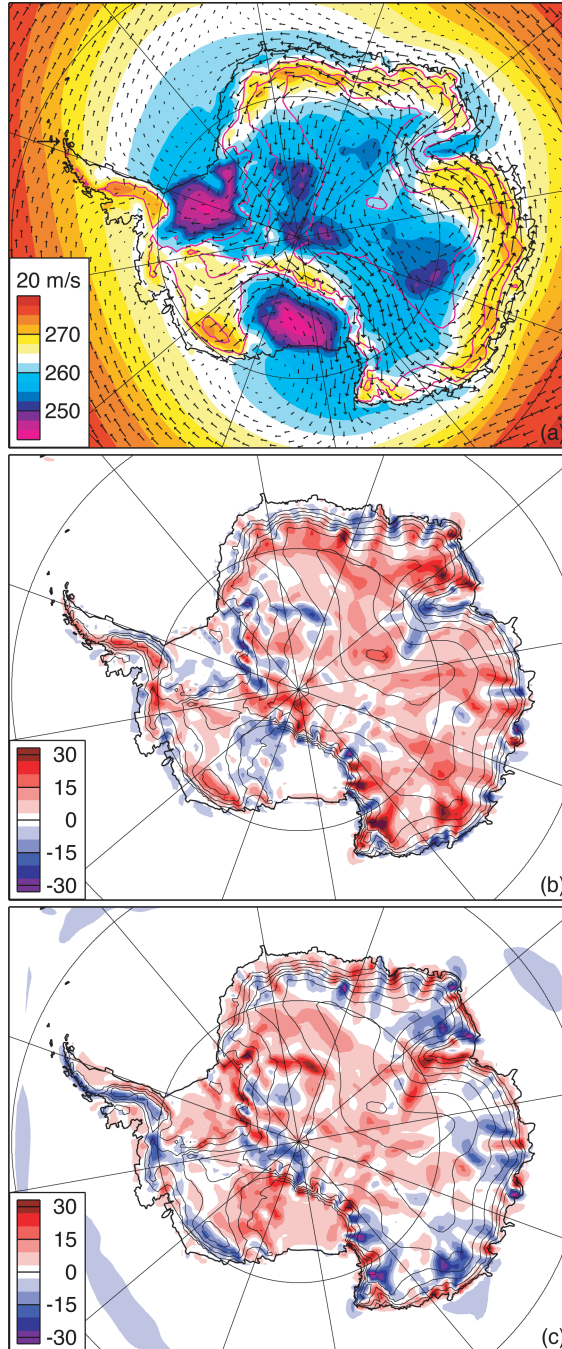


Figure 6.8: Winter averages of (a) ABL mean potential temperature (K) and wind; (b) AdvV in K per day; (c) AdvH in K per day.

Table 6.1: Contributions to $AdvH$.

Abbreviation	product	Horizontal heat advection by:
$AdvH_{ST}$		Synoptical wind and temperature variability
$AdvH_P$		Persistent, monthly mean winds and temperature
$AdvH_{\vec{u}_{lsc}\theta_0}$	$\vec{u}_0 \cdot \nabla\theta_0$	⊥ Large scale wind and background temperature
$AdvH_{\vec{u}_{lsc}\delta\theta}$	$\vec{u}_0 \cdot \nabla\delta\theta$	⊥ Large scale wind and temperature deficit
$AdvH_{\delta\vec{u}\theta_0}$	$\delta\vec{u} \cdot \nabla\theta_0$	⊥ ABL wind and background temperature
$AdvH_{\delta\vec{u}\delta\theta}$	$\delta\vec{u} \cdot \nabla\delta\theta$	⊥ ABL wind and temperature deficit

The coast of West Antarctica and the western side of the Antarctic Peninsula experience cooling by $AdvH$ due to diabatic uplift. Only in these regions, heating by Q (Figure 6.6c) is significant. Since $AdvH$ is calculated using adiabatic trajectories, diabatic uplift along the topography is equivalent with a negative $AdvH$.

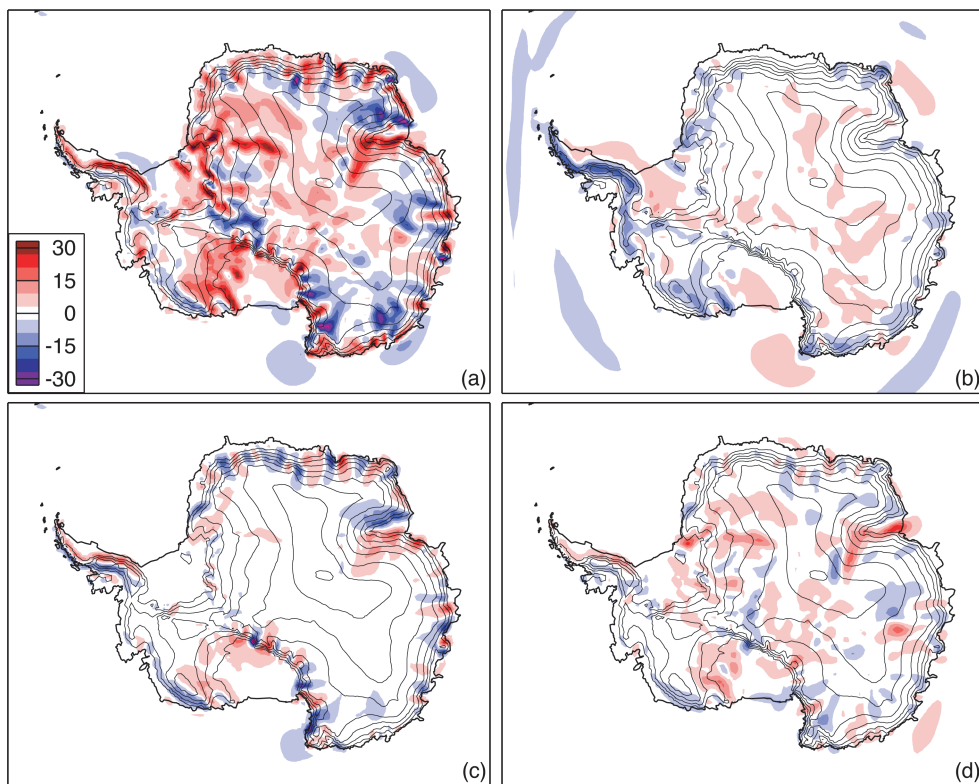
6.4.4 Synoptic and persistent large-scale and ABL contributions to $AdvH$

As mentioned above, $AdvH$ is directly determined by horizontal temperature gradients and the ABL wind field, as shown in Figure 6.8a. In $AdvH$, five contributions can be distinguished, as listed in Table 6.1. First, horizontal heat advection by variability on synoptical time scales ($AdvH_{ST}$) is separated from horizontal heat advection by persistent wind and temperature patterns ($AdvH_P$). Second, following *Van den Broeke et al. (2002)*; *Van den Broeke and van Lipzig (2003)* and *Van de Berg et al. (2007)*, the large-scale, thus background free-atmosphere, and ABL contributions to the temperature and wind profiles are isolated in the persistent wind and temperature patterns. For an example of the profiles of θ_0 , $\delta\theta$, \vec{u}_{lsc} and $\delta\vec{u}$ see Figure 6.5a. Four contributions to $AdvH_P$ are distinguished from these two pairs of wind and temperature fields.

Synoptic and persistent contributions to $AdvH$

$AdvH_P$ (Figure 6.9a) is calculated using monthly mean temperature and wind fields, whereas $AdvH_{ST}$ (Figure 6.9b) is calculated using six-hourly deviations of the monthly mean winds and temperatures.

The similarity between total $AdvH$ (Figure 6.8c) and $AdvH_P$ is high, $AdvH_{ST}$ is generally one order of magnitude smaller. Since topographically driven wind field divergence/convergence is a nearly stationary process, it is expected that $AdvH$ in Antarctica is primarily due to persistent wind and temperature patterns. This is only so because Antarctica has an extreme ABL climate, in which $AdvH$ locally exceeds heating rates of 1 K per hour. Only in Antarctica significant and persistent temperature gradients are found along the prevailing wind. Elsewhere on Earth, $AdvH$ averaged over longer time-scales is at least one order of magnitude smaller, because temperature gradients along the dominant wind become small after a while. Outside of Antarctica, $AdvH_{ST}$ can thus be easily as significant as $AdvH_P$, if not larger.



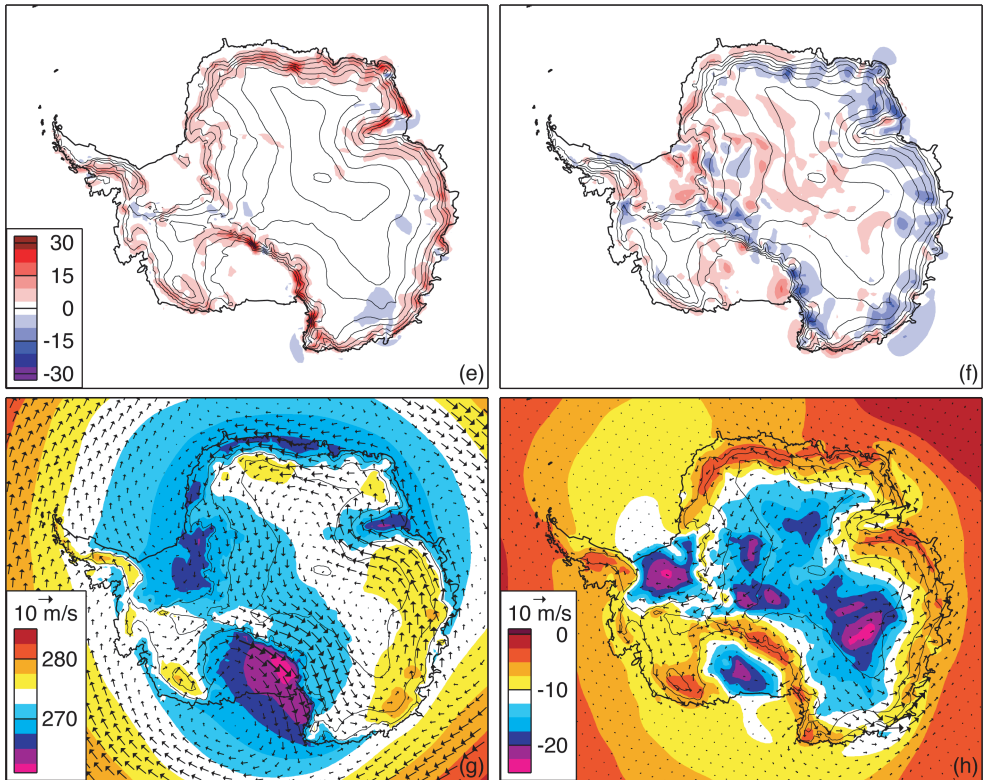


Figure 6.9: Decomposition of winter $AdvH$ into its various contributions (Table 6.1) in K per day: (a) monthly mean temperature and winds; (b) short time-scale variability; (c) large-scale circulation and background temperature profile; (d) large-scale circulation and temperature deficit; (e) ABL winds and background temperature profile; (f) ABL winds and temperature deficit. (g) Large-scale winds on background potential temperature in K (h) ABL residual wind on temperature deficit in K.

Some patterns can be recognized in $AdvH_{ST}$ (Figure 6.9b). In the ABL over the East Antarctic plateau and over the Ross and Filchner-Ronne Ice Shelves, $AdvH_{ST}$ is heating, and in the coastal zone it is cooling. The spine of the Antarctic Peninsula has the highest cooling rates, due to the difference in lapse-rate of wet-adiabatic ascents and dry-adiabatic descents. In contrast to many other high accumulation sites in Antarctica, the directional persistency of the wind is low over the Peninsula, therefore the net heat advection becomes part of $AdvH_{ST}$. Cold air advection is also found on the edges of the sea-ice zone.

Large-scale and ABL contributions to $AdvH$

The winter-mean ABL temperatures and winds (Figure 6.8a) are decomposed in free-atmosphere contributions (Figure 6.9g) and ABL components (Figure 6.9h). Figure 6.9g shows the ABL mean background potential temperature (θ_0) and the large-scale wind vector \vec{u}_{lsc} . θ_0 is mainly a function of latitude and elevation. As a result, the ice shelves have low θ_0 , while northward extending parts of East and West Antarctica have relatively high θ_0 . The sector between 100 and 160° E of the Southern Ocean is relatively warm, while the Atlantic sector is colder. The large-scale circulation consists of westerly winds around Antarctica turning into easterlies over East Antarctica. Quasi-stationary cyclonic cells can be found on the Ross and Filchner-Ronne Ice Shelves and off the coast of Wilkes Land. As was pointed out by *Van den Broeke and van Lipzig* (2003), \vec{u}_{lsc} closely follows the large-scale topography of the ice sheet, reflecting the influence of the ice sheet on the troposphere large-scale circulation through the thermal wind balance.

Figure 6.9h shows the ABL mean temperature deficit ($\delta\theta$) and ABL wind vectors ($\delta\vec{u}$). Over the ocean, the ABL temperature deficit is restricted to the sea ice covered areas, and vanishes over open water. Over the ice sheet, the dependency of the temperature deficit on topographic curvature is clearly visible: Convex topographic features have a weak inversion, while the temperature deficit is larger over concave topography. ABL winds are mainly katabatic, and therefore weak over the sea ice. The importance of friction is apparent from the relative down-slope direction of the vectors. Strongest ABL winds are found in the major ABL outflow locations in East Antarctica, i.e. Adélie Coast and west of the Lambert Glacier Basin.

Figure 6.9c shows heat advection by the large-scale wind and the background temperature ($AdvH_{\vec{u}_{lsc}\theta_0}$). This term highlights the alternating cooling and warming patches in the coastal zone, located at the upwind and downwind side, respectively, of small scale (~ 100 km) topography. It shows that the large-scale circulation does not follow these smaller topographic features, and thus tries to smoothen the smaller scale temperature field induced by $AdvV$ (Figure 6.8b). The large-scale circulation only partly follows the embayment of the Lambert Glacier, causing the larger scale advection patterns there. Cooling and warming patterns on the Antarctic Peninsula and in Marie Byrd Land are related to condensation at the upwind side (see Figure 6.6c) and föhn on the lee side.

Figure 6.9d shows the advection of heat by the large-scale circulation of the ABL temperature deficit ($AdvH_{\vec{u}_{lsc}\delta\theta}$). This frame shows most variability, partly reflecting the large spatial variability in ABL temperature deficit in Antarctica (Figure 6.9h). Cooling and heating patterns match gradients in inversion strength along the large-scale wind. Above 2000 m in

East Antarctica (Figure 6.9a), the similarity between the patterns in $AdvH_P$ and $AdvH_{\bar{u}_{isc}\delta\theta}$ indicates that this component dominates the $AdvH$ variability there.

The advection by ABL wind of background temperature ($AdvH_{\delta\bar{u}\theta_0}$) is primarily a heating contribution in the coastal zone (Figure 6.9e). This represents downslope advection of potentially warmer air, driving a large-scale föhn effect.

Figure 6.9f shows advection of temperature deficit by ABL wind ($AdvH_{\delta\bar{u}\delta\theta}$). $AdvH_{\delta\bar{u}\delta\theta}$ mostly cools the escarpment of East Antarctica, where the inversion strength is reduced by extensive mechanically driven vertical mixing. In contrast to the large-scale circulation, $\delta\bar{u}$ has a significant downslope component, and $AdvH_{\delta\bar{u}\delta\theta}$ can therefore maintain low-level cold air advection. Warming by $AdvH_{\delta\bar{u}\delta\theta}$ is found in regions where $\delta\bar{u}$ points into a location with a stronger inversion. Besides regions in the East Antarctica plateau with concave topography, such warming is found where the ice sheet is fringed by ice shelves.

6.5 Results: Summer

6.5.1 External heating and surface interactions

The strong katabatic winds in the winter ABL are indirectly forced by a large surface radiation deficit. In the austral summer months December and January, net solar insolation brings the surface radiation budget into balance. The summer ABL is thus not dominated by katabatic flow. SHD is thus largely reduced, as is visible in Figure 6.10a, with cooling rates of on average 2 K per day. Over the ocean, SHD is also small.

The cooling by longwave divergence (LWD) has even less spatial variability (Figure 6.10b). Over the ocean, LWD is reduced on those locations where cloud top height is mostly above the ABL depth.

The heating or cooling by water phase changes is similar to winter (Figure 6.10c). Over the ocean, the heat released by condensation is balanced by melt of falling snow near the surface. The small cooling spots along the coast are due to evaporation of precipitation in the adiabatically dried ABL.

The heating by shortwave radiation divergence (SWD) and convection (CHD) are not shown. SWD heats the ABL by about 1 K per day. SWD is slightly larger over Antarctica than over the Southern Ocean. Evaluation of model results with satellite observations (Section 6.2) showed that the model underestimates total net SW absorption over the ice sheet, but still SWD would be small. CHD is less than 1 K per day over land, and on average 1 K per day over the ocean.

6.5.2 Heat advection

In absence of continuous surface cooling, the surface temperature deficit (Figure 6.11a) is small in the austral summer. Katabatic winds and thus subsidence are weaker. Vertical heat advection (Figure 6.11b) is still a net source of energy, but one order of magnitude smaller than during winter. Domes and convex ridges are again locations with slightly stronger warming by $AdvH$. Even more than in winter, $AdvH$ counterbalances $AdvV$ (Figure 6.11c). $AdvV$ and $AdvH$ are thus mostly determined by topographical induced convergence or divergence of the surface wind field and the resulting vertical winds. The large-scale circulation

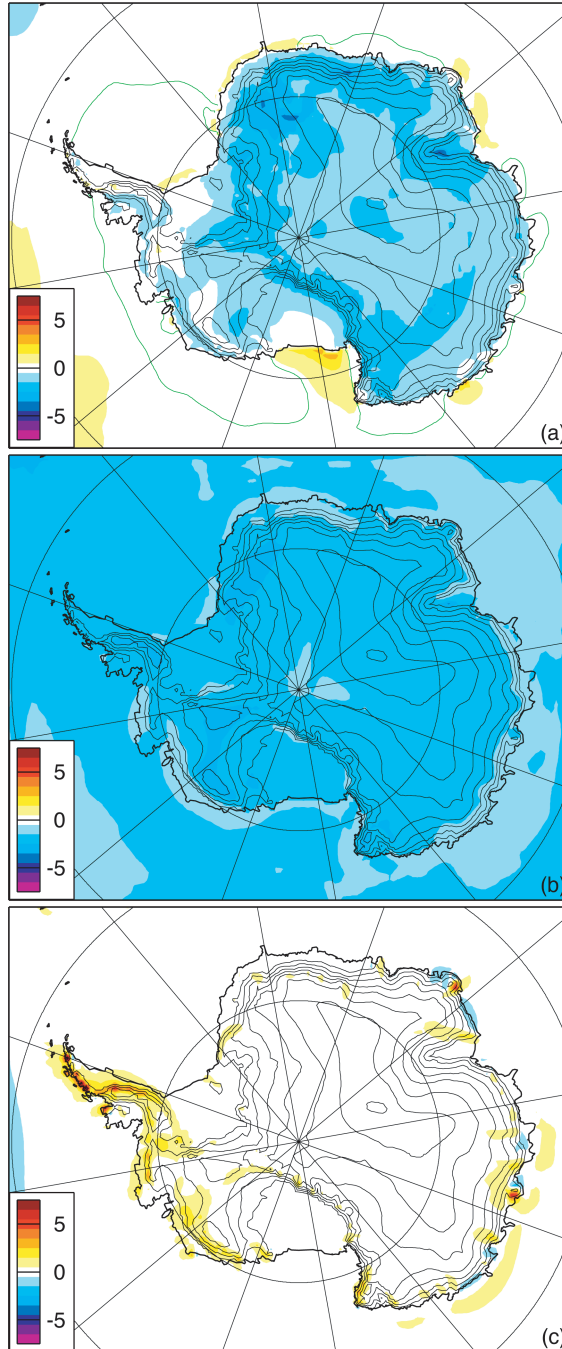


Figure 6.10: Average summer boundary layer temperature forcing by (a) SHD, (b) LWD and (c) Q in K per day. 50% sea ice cover isopleths are drawn in green in (a).

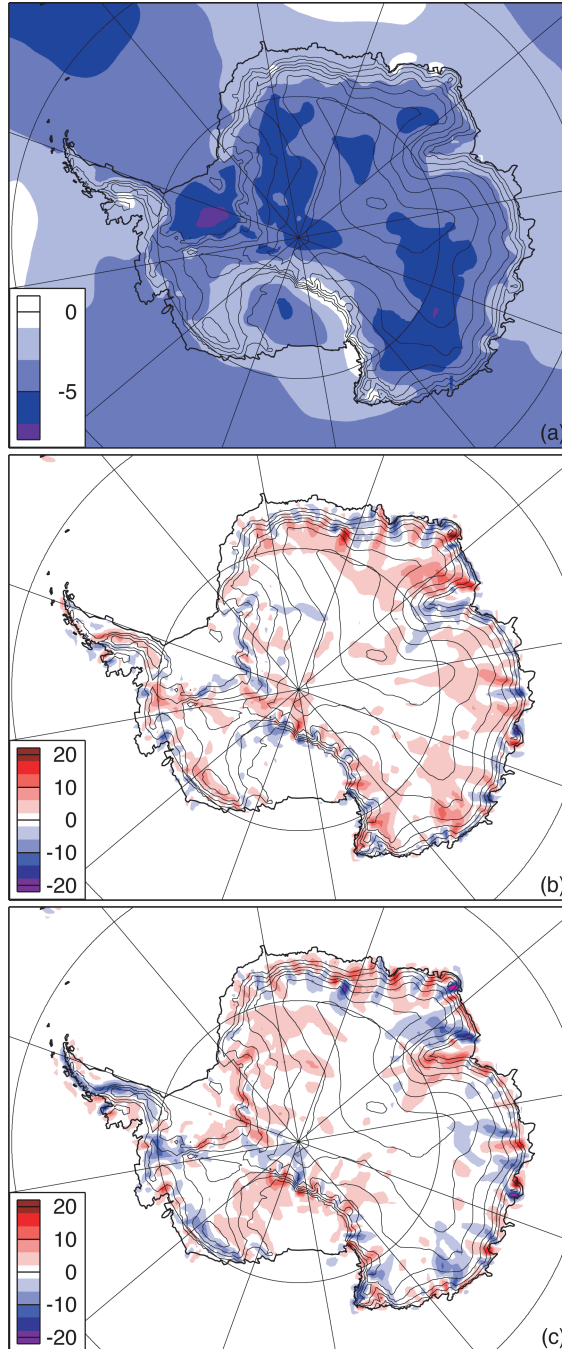


Figure 6.11: Summer averages of (a) ABL mean potential temperature deficit in K, (b) AdvV in K per day and (c) AdvH in K per day.

in the ABL is rather independent of season (Van den Broeke and van Lipzig, 2003), but ABL deviations are strongly reduced. $AdvH_{\bar{u}_{isc}\theta_0}$ is the main contributor to $AdvH$, and nearly equals its winter value (Figure 6.9c). The other four contributions ($AdvH_{ST}$, $AdvH_{\bar{u}_{isc}\delta\theta}$, $AdvH_{\delta\bar{u}\theta_0}$ and $AdvH_{\delta\bar{u}\delta\theta}$) also resemble the winter spatial patterns, but the magnitudes are reduced by a factor of three on average.

6.6 Summary and conclusions

The heat budget of the Antarctic ABL is investigated using output of the regional atmospheric climate model RACMO2/ANT.

During winter, divergence of the sensible heat flux (SHD) and long-wave radiation flux (LWD) are the primary cooling terms over the ice sheet. Both terms are spatially smooth, and SHD is largely controlled by ABL depth. Averaged over the ice sheet, vertical heat advection ($AdvV$) by subsidence is the primary heat source. Horizontal heat advection ($AdvH$) is a secondary heating term. $AdvV$ and $AdvH$ show counterbalancing spatial patterns. At domes and ridges, where the topography is convex, the ABL wind field diverges so that ABL is heated by subsidence ($AdvV$). In response, $AdvH$ cools at these locations. Conversely, in valleys, which have concave topography, the ABL wind converges; subsidence is reduced or even reverted, and $AdvV$ can become a cooling term. The temperature deficit thus increases there, and $AdvH$ warms the ABL.

$AdvH$ is predominantly determined by the climatological wind and temperature fields, as can be expected for a process that is governed by topography. In the interior of East Antarctica, $AdvH$ is mainly determined by the advection of the ABL temperature deficit along the large-scale and ABL wind. Along the coast, advection of background temperature along the large-scale wind mainly determines the patterns in $AdvH$. This is because the large-scale wind and background temperature are unable to adjust to topographic features smaller than a few hundred km.

During summer, the ABL temperature deficit is restricted to the nocturnal ABL. Warming by $AdvV$ and $AdvH$ are therefore much reduced in magnitude compared to winter, but spatial patterns are found to be similar.

These processes govern the temperature in the Antarctic ABL. A next step will be to investigate how these processes might alter in a changing climate, and thus how Antarctic near surface temperatures might change in the future.

Chapter 7

Suggestions for future work

In this last chapter, we give some suggestions for further research and model refinements. One topic is discussed in more detail, using of results of a pilot study with adjusted model cloud parameters.

7.1 Applications for heat budget analyses

The heat budget quantifies processes that determine the temperature tendency. On time scales larger than a few weeks temperature tendencies are small, yielding a climatological heat budget that is a balance between counteracting processes. In Chapters 5 and 6 of this thesis, the vertical and horizontal structure of the seasonal mean heat budget is presented. A logical next step is to analyze the variability and trends of the heat budget components. Analogously, *Van den Broeke et al. (2002)* presented the momentum budget of the Antarctic ABL, which was used by *Van den Broeke and van Lipzig (2002)* to investigate the effect of polar vortex variability on ABL temperatures.

Analyzing the relation between temperature variability and the heat budget is, however, less straightforward than for wind and the momentum budget. Wind is explicitly represented in the momentum budget by the Coriolis effect, but temperature is only indirectly represented in the atmospheric heat budget. Nevertheless, it is expected that the atmospheric heat budget *for the ABL* will also show clear patterns, because of its strong connection to the surface energy balance. However, analysis of heat budget variability and trends for the free troposphere will not necessarily provide coherent results, since the magnitudes of the components are relatively small compared to the ABL.

A critical additional condition for variability or trend analysis is that observed variability and trends are well reproduced by the atmospheric model. If not, it is likely that the processes governing the trends are not well captured either. We compared observed temperature trends in Antarctica with model results from RACMO2/ANT, and found for the moment insufficient agreement for a meaningful interpretation of observed temperature trends in terms of heat budget changes. The main problem is that warming in the Antarctic atmosphere is overestimated in RACMO2/ANT. The interior of RACMO2/ANT closely reproduces the free

atmospheric temperature trends of ERA-40, which are provided through the lateral boundary conditions. Analysis of temporal heat budget variability in regional climate models is thus hampered as long as re-analyses are unable to faithfully reproduce large-scale Antarctic temperature trends.

7.2 SMB of the Antarctic ice sheet

The other focus of this thesis is the SMB of the Antarctic ice sheet. The ice sheet mass balance of the Antarctic is determined by the total accumulation on the grounded part of the ice sheet and the ice flux across the grounding line. A precise estimate of the present day SMB is thus very valuable. In Chapters 3 and 4, observations and model results are combined in order to estimate the SMB of the ice sheet and the error margin of this estimate.

It is clear from the results that the lack of coastal in situ observations is the primary obstacle for a more precise SMB estimate. In coastal Antarctica, the discrepancy between calibrated model SMB and estimates from interpolated observations (*Vaughan et al.*, 1999; *Arthern et al.*, 2006) is largest. Unfortunately, the coastal and escarpment zones are also the most difficult regions of Antarctica to perform SMB observations. The local climate is harsh; the ice sheet may be crevassed and local SMB variability is large. But without new observations from these regions, Antarctic SMB estimates from various methods are not likely to converge.

Furthermore, every new assessment of Antarctic SMB must critically review the quality of the observations that are used for interpolation or evaluation. *Magand et al.* (2007) showed that in East Antarctica, inferior observations leads to a 20% overestimation of SMB on the high plateau. Moreover, if the method described by *Arthern et al.* (2006) is applied to the quality controlled data set described in Chapter 3, SMB estimates in coastal sectors of 90° to 150° W and 80° to 120° E increase by 100 mm w.e. per year (R. J. Arthern, personal communication).

Apart from increasing the number of in situ observations, model adjustments could certainly improve SMB. A resolution of 50 km is sufficient to estimate total accumulation in Antarctica and to resolve large-scale spatial patterns on the plateaus of East and West Antarctica. However, a higher resolution is required for a more detailed SMB map of the Antarctic coastal zone and in particular of the Antarctic Peninsula. An example of such a study is *Van Lipzig et al.* (2004), who ran RACMO1/ANT at 14 km resolution over the Antarctic Peninsula. This study shows, in line with results from field studies (*Frezzotti et al.*, 2007), that on small spatial scales snow drift strongly influences the SMB distribution. However, snow surface characteristics and snow history are as important for drifting snow processes as the near-surface wind field (*Pomeroy and Essery*, 1991). Meaningful high resolution SMB estimates thus require thus a parameterization of snow drift and snow surface structure (*Gallée et al.*, 2005).

7.3 A pilot study with decreased ice crystal fall speed

RACMO2/ANT tends to overestimate the coast-to-interior SMB gradient. In Sections 2.5 and 3.5.2, the neglect of diamond dust is proposed as a possible cause for the underestimated

Table 7.1: Ice cloud particle fall speed estimate and parameterizations, as function of the ice water content (IWC , kg m^{-3}).

Study / parameterization	Terminal fall speed (m s^{-1})	
	small particles	large particles
<i>Heymsfield and Donner</i> (1990)	$3.29 \cdot IWC^{0.16}$	
CY23R4, CY25R1	$3.29 \cdot IWC_{<100}^{0.16}$	“fast”
CY28R1	0.15	$2.3 \cdot IWC_{>100}^{0.16}$
This test	$\text{Min}(0.329 \cdot IWC_{<100}^{0.26}, 0.15)$	$0.23 \cdot IWC_{>100}^{0.16}$

SMB in the interior. Here, another solution for this model inaccuracy is tested, namely a slower removal of snowflakes from pure ice clouds by reducing the ice crystal fall speed.

The ECMWF / RACMO2/ANT physics distinguishes three cloud types: pure water clouds for non-freezing temperatures, mixed phase clouds for temperatures between 0 and -23°C and pure ice clouds for temperatures below -23°C . Pure ice clouds are supposed to consist of small ($< 100\mu\text{m}$) and larger particles. The amount of large particles increases when the cloud ice concentration increases. ECMWF model cycle CY23R4, which was used for ERA-40, and model cycle CY25R1 prescribe an instantaneous fall-out of the large ice particles and a gradual sedimentation of the small ice particles to lower model levels, using fall speeds deduced from *Heymsfield and Donner* (1990) (Table 7.1). In cycle CY28R1, terminal fall speeds were reduced. The model results presented in Chapter 2 were derived using the parameters of cycle CY23R4. Thereafter (Chapter 3), the model code and parameters of cycle CY28R1 were used for cloud parameterization.

Runs with a single column model showed that for all parameter sets as implemented in the ECMWF physics, a large fraction of the cloud ice is removed within one time step of 720 seconds, even for very thin clouds. *Heymsfield and Donner* (1990) state that roughly 60% of the deposited mass precipitates out of the lifting layer after about one hour, so the ECMWF physics might overestimate the snow removal rate from pure ice clouds.

We investigated the effect of a reduced fall speed in a model evaluation from 1998 until the end of 2001. In the test, the relevant parameters were reduced by a factor ten (Table 7.1). In order to avoid discontinuous behavior at -23°C , terminal fall speeds between -13 and -23°C change linearly from those for mixed clouds to those for pure ice clouds. The direct result of the reduced fall speeds is a thickening of pure ice clouds, which induces several important changes of the model climatology.

First of all, horizontal advection of cloud ice becomes more important. In the original configuration, precipitation was predominantly deposited at the location of condensation. In this test run, more snow is advected downstream of the location of condensation. As a result, snowfall slightly decreases over the Antarctic Ocean, where most cloud formation occurs (Figure 7.1a). On the other hand, snowfall increases in Antarctica, and the largest relative increase is found on the East Antarctic plateau. The mean SMB value for the four years of this test are shown in Figure 7.1b. Continent wide SMB patterns are unchanged compared to the original simulated SMB (Figure 2.4a) or the calibrated model SMB (Figure 3.7a). However, in the control run, a large part of the interior of East Antarctica received less

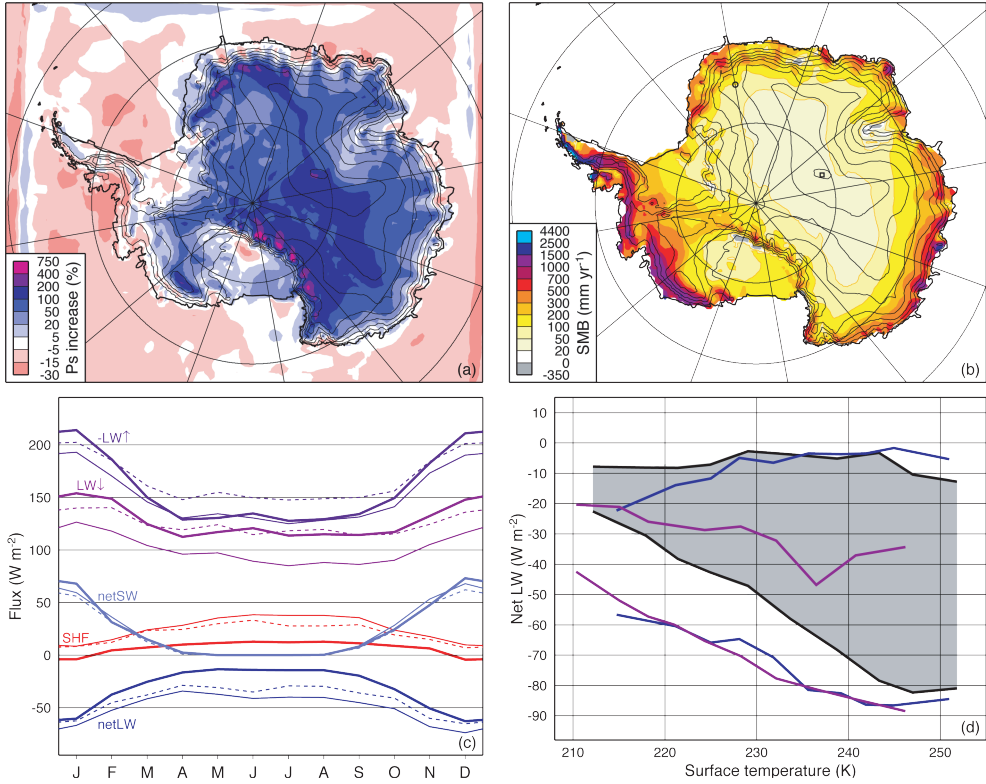


Figure 7.1: Results from a pilot test with decreased ice crystal fall speed. (a) Percentage of change of solid precipitation (P_s) in percents with respect to original model run. (b) Simulated SMB for 1998 to 2001. Dome A and AWS 9 are indicated by a square and circle, respectively. (c) Comparison of observed and simulated surface energy budget at AWS 9 (0° E, 75° S). Observations, original model results and the pilot test results are drawn with a thick, thin and dashed line, respectively. Energy fluxes are positive when pointed towards the surface, except the emitted longwave radiation ($LW\uparrow$). (d) Range of net surface LW as function of the surface temperature for AWS9. Observations, control run and test run are shown in black, purple and blue, respectively.

than 20 mm per year, with a minimum of 5 mm per year near Dome A. In the new run, the SMB on the East Antarctic plateau remains well above 20 mm per year, which agrees better with observations (Figure 3.1). Minimum simulated SMB in the plateau is now 24 mm per year. A quantitative comparison with observations, equal to the analysis described in section 3.4.4, shows that the coast-to-interior precipitation gradient is now smaller than observed. Model simulated SMB especially exceeds observations in the escarpment zone (1500 - 2500 m asl). Furthermore, the total accumulation on the grounded ice sheet increases by 15%. We conclude that this adjustment can indeed improve model SMB, but that a reduction by a factor ten for ice crystal fall speed is too vigorous.

Besides increased precipitation, the thicker clouds also cause an increase in downwelling longwave radiation. Figure 7.1c compares the observed surface energy budget (SEB) at AWS

9 (0° E, 75° S) with results of the original run and the pilot test. The SEB at AWS 9 is representative for inland Antarctica. In this figure, fluxes are positive when pointed towards the surface, except for surface emitted LW ($LW\uparrow$). The observations show that in winter, the emitted LW is largely compensated by downwelling LW ($LW\downarrow$); SHF provides a secondary contribution. During summer, net insolation (netSW) additionally heats the surface, although its contribution is limited due to the high snow albedo. SHF is slightly negative. The latent heat flux is negligible and not shown.

In the original model results, downwelling LW and SHF are systematically underestimated and overestimated by about 20 W/m^2 , respectively. These errors counterbalance in winter, so the surface temperature, i.e. emitted LW, match observations well. A small cool bias is found for summer.

In the pilot test results, thicker clouds brings the downwelling LW in agreement with observations. However, as SHF remains overestimated, an overestimation of $LW\uparrow$ is now found, caused by a positive surface temperature bias during winter. This shows that the overestimated SHF is primarily due to an overactive mixing scheme and *not* a model response to underestimated downwelling LW. So, changes in the cloud scheme revealed deficiencies in the mixing scheme that must also be fixed in order to keep near-surface temperatures unbiased.

Figure 7.1d shows net surface LW as function of daily mean surface temperature at AWS 9 in order to investigate if the range of net LW is well simulated in RACMO2/ANT. The observations (*Van den Broeke et al.*, 2004a) (black) and model results (purple and blue) were binned as function of surface temperature. For a certain surface temperature, net LW emission is mostly influenced by cloudiness. During overcast conditions, observations show that the net LW emission is near zero. Maximum net LW emission occurs during cloud free conditions (lower line).

Results from the control run (purple) show a range that is well below the range of the observations. Simulated atmospheric LW emissivity is underestimated for *all* cloud conditions. For overcast conditions, net LW emission remains well below zero, which implies that model clouds are too thin to become opaque for LW radiation.

The results from the run with decreased ice crystal fall velocity show that net LW emission for overcast conditions agrees well with observations in the results from the pilot test (blue lines). Thus, decreasing the cloud ice fall speed indeed improves the model cloud climatology. However, net LW emission for clear-sky conditions is still biased. The bias could be either due to an erroneous model climatology, thus a too cold and/or too dry atmosphere, or due to a lacking parameterization for atmospheric LW emission under polar conditions. Additional evaluation is needed to isolate the reason of this model shortcoming.

Bibliography

- Andreas, E. L. (1987), A theory for the scalar roughness and the scalar transfer coefficients over snow and sea ice, *Boundary-Layer Meteorology*, 38, 159–184.
- Arthern, R. J., D. P. Winebrenner, and D. G. Vaughan (2006), Antarctic snow accumulation mapped using polarization of 4.3-cm wavelength microwave emission, *Journal of Geophysical Research*, 111(D06107), doi:10.1029/2004JD005,667.
- Bentley, M. J., D. A. Hodgson, D. E. Sugden, S. J. Roberts, J. A. Smith, M. J. Leng, and C. Bryant (2005), Early Holocene retreat of the George VI Ice Shelf, Antarctic Peninsula, *Geology*, 33(3), 173–176.
- Box, J. E. (2005), Greenland ice sheet surface mass-balance variability: 1991–2003, *Annals of Glaciology*, 42, 90–94.
- Box, J. E., D. H. Bromwich, and L.-S. Bai (2004), Greenland ice sheet surface mass balance 1991–2000: Application of Polar MM5 mesoscale model and in situ data, *Journal of Geophysical Research*, 109(D16105), doi:10.1029/2003JD004,451.
- Bromwich, D. H. (1988), Snowfall in high southern latitudes, *Reviews of Geophysics*, 26(1), 149–168.
- Bromwich, D. H., and R. L. Fogt (2004), Strong trends in the skill of the ERA-40 and NCEP–NCAR reanalyses in the high and midlatitudes of the Southern Hemisphere, 1958–2001, *Journal of Climate*, 17, 4603–4619.
- Bromwich, D. H., Z. Guo, L. Bai, and Q.-S. Chen (2004), Modeled Antarctic Precipitation. Part I: Spatial and Temporal Variability, *Journal of Climate*, 17, 427–447.
- Brost, R. A., and J. C. Wyngaard (1978), A model study of the stably stratified planetary boundary layer, *Journal of the Atmospheric Sciences*, 35, 1427–1440.
- Bull, C. (1971), *Research in the Antarctic*, chap. Snow Accumulation in Antarctica, pp. 367–421, American Association for the Advancement of Science.
- Cerni, T. A., and T. R. Parish (1984), A radiative model of the stable nocturnal boundary layer with application to the polar night, *Journal of Climate and Applied Meteorology*, 23, 1563–1572.
- Comiso, J. C. (2000), Variability and trends in Antarctic surface temperature from in situ and satellite infrared measurements, *Journal of Climate*, 13, 1674–1696.
- Connolley, W. M. (1996), The Antarctic temperature inversion, *International Journal of Climatology*, 16, 1333–1342.
- Connolley, W. M., and J. C. King (1996), A modeling and observational study of East Antarctic surface mass balance, *Journal of Geophysical Research*, 101(D1), 1335–1343.

- Cook, A. J., A. J. Fox, D. G. Vaughan, and J. G. Ferrigno (2005), Retreating glacier fronts on the Antarctic Peninsula over the past half-century, *Science*, *308*, 541–544.
- Davis, C. H., Y. Li, J. R. McConnell, M. M. Frey, and E. Hanna (2005), Snowfall-driven growth in East Antarctic ice sheet mitigates recent sea-level rise, *Science*, *308*, 1898–1901.
- De Angelis, H., and P. Skvarca (2003), Glacier surge after ice shelf collapse, *Science*, *299*, 1560–1562.
- Déry, S. J., and M. K. Yau (2002), Large-scale mass balance effects of blowing snow and surface sublimation, *Journal of Geophysical Research*, *107*(D23), doi:10.1029/2001JD001,251.
- Dethloff, K., et al. (2002), Recent Greenland accumulation estimated from regional climate model simulations and ice core analysis, *Journal of Climate*, *15*(19), 2821–2832.
- Domack, E., et al. (2005), Stability of the Larsen B ice shelf on the Antarctic Peninsula during the Holocene epoch, *Nature*, *436*, 681–685.
- Douville, H., J.-F. Royer, and J.-F. Mahfouf (1995), A new snow parameterization for the Météo-France climate model, *Climate Dynamics*, *12*, 37–52.
- Easterling, D. R., and T. C. Peterson (1995), A new method for detecting undocumented discontinuities in climatological time series, *International Journal of Climatology*, *15*, 369–377.
- Ekaykin, A. A. (2003), Meteorological regime of central Antarctica and its role in the formation of isotope composition of snow thickness, Ph.D. thesis, University Grenoble 1.
- Ekaykin, A. A., V. Y. Lipenkov, I. N. Kuzmina, J. R. Petit, V. Masson-Delmotte, and S. J. Johnsen (2004), The changes in isotope composition and accumulation of snow at Vostok station, East Antarctica, over the past 200 years, *Annals of Glaciology*, *39*, 569–575.
- EPICA community members (2004), Eight glacial cycles from an Antarctic ice core, *Nature*, *429*, 623–628.
- Frezzotti, M., S. Urbini, M. Proposito, C. Scarchilli, and S. Gandolfi (2007), Spatial and temporal variability of surface mass balance near Talos Dome, East Antarctica, *Journal of Geophysical Research*, *112*(F2, F02032), doi:10.1029/2006JF000,638.
- Frezzotti, M., et al. (2004), New estimations of precipitation and surface sublimation in East Antarctica from snow accumulation measurements, *Climate Dynamics*, *23*(7-8), 803–813.
- Gallée, H., V. Peyaud, and I. Goodwin (2005), Simulation of the net snow accumulation along the Wilkes Land transect, Antarctica, with a regional climate model, *Annals of Glaciology*, *41*, 17–22.
- Ganachaud, A., and C. Wunsch (2000), Improved estimates of global ocean circulation, heat transport and mixing from hydrological data, *Nature*, *408*, 453–457.
- Genthon, C. (2002), Climate and surface mass balance of the polar ice sheets in ERA40/ERA15, *ECMWF Re-analysis Project Report Series 3*, European Centre For Medium-Range Weather Forecasts (ECMWF).
- Genthon, C., and G. Krinner (2001), Antarctic surface mass balance and systematic biases in general circulation models, *Journal of Geophysical Research*, *106*(D18), 20,653–20,664.
- Genthon, C., G. Krinner, and M. Déqué (1998), Inter-annual variability of Antarctic precipitation from weather forecasts and high-resolution climate models, *Annals of Glaciology*, *27*, 488–494.

- Giovinetto, M. B., and C. R. Bentley (1985), Surface balance in ice drainage systems of Antarctica, *Antarctic Journal of the US*, 20(4), 6–13.
- Giovinetto, M. B., and H. J. Zwally (2000), Spatial distribution of net surface accumulation on the Antarctic ice sheet, *Annals of Glaciology*, 31, 171–178.
- Greve, R. (2000), On the response of the Greenland ice sheet to greenhouse climate change, *Climate Change*, 46, 283–302.
- Guo, Z., D. H. Bromwich, and J. J. Cassano (2003), Evaluation of polar MM5 simulations of Antarctic atmospheric circulation, *Monthly Weather Review*, 131, 384–411.
- Guo, Z., D. H. Bromwich, and K. M. Hines (2004), Modeled Antarctic precipitation. part II: ENSO modulation over West Antarctica, *Journal of Climate*, 17, 448–465.
- Heymsfield, A. J., and L. J. Donner (1990), A scheme for parameterizing ice-cloud water content in general circulation models, *Journal of the Atmospheric Sciences*, 47, 1865–1877.
- Hofstede, C. M., et al. (2004), Firn accumulation records for the past 1000 years on the basis of dielectric profiling of six cores from Dronning Maud Land, Antarctica, *Journal of Glaciology*, 50(159), 279–291.
- Holton, J. R. (1992), *An Introduction to Dynamic Meteorology*, *International Geophysics Series*, vol. 48, 3rd ed., Academic Press.
- Huybrechts, P., D. Steinhage, F. Wilhelms, and J. L. Bamber (2000), Balance velocities and measured properties of the Antarctic ice sheet from a new compilation of gridded data for modelling, *Annals of Glaciology*, 30, 52–60.
- Huybrechts, P., J. M. Gregory, and M. Wild (2004), Modelling Antarctic and Greenland volume changes during the 20th and 21st centuries forced by GCM time slice integrations, *Global and Planetary Change*, 42, 83–105.
- IPCC (2001), *Climate change 2001: The scientific basis. Contribution of working group I to the third assessment report of the Intergovernmental Panel on Climate Change*, Cambridge University Press.
- IPCC (2007), *Climate Change 2007 - The Physical Science Basis*, Cambridge University Press.
- Johanson, C. M., and Q. Fu (2007), Antarctic atmospheric temperature trend patterns from satellite observations, *Geophysical Research Letters*, 34(L12703), doi:10.1029/2006GL029,108.
- Karlöf, L., et al. (2000), A 1500 year record of accumulation at Amundsenisen western Dronning Maud Land, Antarctica, derived from electrical and radioactive measurements on a 120m ice core, *Journal of Geophysical Research*, 105(D10), 12,471–12,483.
- Kaspari, S., P. A. Mayewski, D. A. Dixon, V. B. Spikes, S. B. Sneed, M. J. Handley, and G. S. Hamilton (2004), Climate variability in West Antarctica derived from annual accumulation rate records from ITASE firn/ice cores, *Annals of Glaciology*, 39, 585–594.
- King, J. C., and J. Turner (1997), *Antarctic Meteorology and Climatology*, Cambridge atmospheric and space science series, Cambridge University Press.
- King, J. C., W. M. Connolley, and S. H. Derbyshire (2001), Sensitivity of modelled Antarctic climate to surface and boundary-layer flux parameterizations, *Quarterly Journal of the Royal Meteorological Society*, 127, 779–794.

- Krinner, G., C. Genthon, Z.-X. Li, and P. L. Van (1997), Studies of the Antarctic climate with a stretched-grid general circulation model, *Journal of Geophysical Research*, 102(D12), 13,731–13,745.
- Lenderink, G., B. van den Hurk, E. van Meijgaard, A. van Ulden, and H. Cuijpers (2003), Simulation of present-day climate in RACMO2: first results and model developments, *Tech. Rep. TR-252*, KNMI.
- Liu, H., K. Jezek, B. Li, and Z. Zhao (2001), Radarsat Antarctic Mapping Project digital elevation model version 2, Digital media.
- Liu, J., J. A. Curry, and D. G. Martinson (2004), Interpretation of recent Antarctic sea ice variability, *Geophysical Research Letters*, 31(L02205), doi:10.1029/2003GL018,732.
- MacAyeal, D. R., T. A. Scambos, C. L. Hulbe, and M. A. Fahnestock (2003), Catastrophic ice-shelf break-up by an ice-shelf-fragment-capsize mechanism, *Journal of Glaciology*, 49(164), 22–36.
- Magand, O., M. Frezzotti, M. Pourchet, B. Stenni, L. Genoni, and M. Fily (2004), Climate variability along latitudinal and longitudinal transects in East Antarctica, *Annals of Glaciology*, 39, 351–358.
- Magand, O., C. Genthon, M. Fily, G. Krinner, G. Picard, M. Frezzotti, and A. A. Ekaykin (2007), An up-to-date quality-controlled surface mass balance data set for the 90–180 E Antarctica sector and 1950–2005 period, *Journal of Geophysical Research*, 112(D12106), doi:10.1029/2006JD007,691.
- Marshall, G. J., A. Orr, N. P. M. van Lipzig, and J. C. King (2006), The impact of a changing southern hemisphere annular mode on Antarctic Peninsula summer temperatures, *Journal of Climate*, 19, 5388–5404.
- Mastrantonio, G., V. Malvestuto, S. A. Argentini, T. Georgiadis, and A. Viola (1999), Evidence of a convective boundary layer developing on the Antarctic Plateau during the summer, *Meteorology and Atmospheric Physics*, 71, 127–132.
- Monaghan, A. J., et al. (2006), Insignificant change in Antarctic snowfall since the International Geophysical Year, *Science*, 313, 827–831.
- Morris, E. M., and D. G. Vaughan (2003), *Antarctic Peninsula Climate Variability*, *Antarctic Research Series*, vol. 79, chap. Spatial and temporal variation of surface temperature on the Antarctic Peninsula and the limit of viability of ice shelves, pp. 61–68, American Geophysical Union.
- Mosley-Thompson, E., L. G. Thompson, J. F. Paskievitch, M. Pourchet, A. J. Gow, M. E. Davis, and J. Kleinman (1995), Recent increase in South Pole snow accumulation, *Annals of Glaciology*, 21, 131–138.
- Oerter, H., W. Graf, F. Wilhelms, A. Minikin, and H. Miller (1999), Accumulation studies on Amundsenisen, Dronning Maud Land, Antarctica, by means of tritium, dielectric profiling and stable-isotope measurements: first results from the 1995-96 and 1996-97 field seasons, *Annals of Glaciology*, 29, 1–9.
- Oerter, H., F. Wilhelms, F. Jung-Rothenhäusler, F. Göktas, H. Miller, W. Graf, and S. Sommer (2000), Accumulation rates in Dronning Maud Land, Antarctica, as revealed by dielectric-profiling measurements of shallow firn cores, *Annals of Glaciology*, 30, 27–34.
- Orsi, A. H., G. C. Johnson, and J. L. Bullister (1999), Circulation, mixing, and production of Antarctic Bottom Water, *Progress in Oceanography*, 43, 55–109.

- Parish, T. R., and D. H. Bromwich (1987), The surface windfield over the Antarctic ice sheets, *Nature*, 328, 51–54.
- Parish, T. R., and J. J. Cassano (2003a), The role of katabatic winds on the Antarctic surface wind regime, *Monthly Weather Review*, 131, 317–333.
- Parish, T. R., and J. J. Cassano (2003b), Diagnosis of the katabatic wind influence on the wintertime Antarctic surface wind field from numerical simulations, *Monthly Weather Review*, 131, 1128–1139.
- Pirrit, J., and G. A. Doumani (1961), Glaciology, Byrd Station and Mary Byrd Land Traverse, 1959–1960, *Tech. Rep. Project 968, Report No. 2*, The Ohio State University.
- Pomeroy, J. W., and R. L. H. Essery (1991), Turbulent fluxes during blowing snow: field tests of model sublimation predictions, *Hydrological Processes*, 13, 2963–2975.
- Pudsey, C. J., and J. Evans (2001), First survey of Antarctic sub-ice shelf sediments reveals mid-Holocene ice shelf retreat, *Geology*, 29(9), 787–790.
- Ramillien, G., A. Lombard, A. Cazenave, E. R. Ivins, M. Llubes, F. Remy, and R. Biancale (2006), Interannual variations of the mass balance of the Antarctica and Greenland ice sheets from GRACE, *Global and Planetary Change*, 53, 198–208.
- Reijmer, C., E. van Meijgaard, and M. van den Broeke (2004), Numerical studies with a regional atmospheric climate model based on changes in the roughness length for momentum and heat over Antarctica, *Boundary-Layer Meteorology*, 111(2), 313–337.
- Reijmer, C. H., E. van Meijgaard, and M. R. van den Broeke (2005), Evaluation of temperature and wind over Antarctica in a Regional Atmospheric Climate Model using 1 year of automatic weather station data and upper air observations, *Journal of Geophysical Research*, 110(D04103), doi:10.1029/2004JD005,234.
- Renfrew, I. A. (2004), The dynamics of idealized katabatic flow over a moderate slope and ice shelf, *Quarterly Journal of the Royal Meteorological Society*, 130, 1023–1045.
- Rignot, E., and R. H. Thomas (2002), Mass balance of polar ice sheets, *Science*, 297, 1502–1506.
- Rignot, E., J. Bamber, M. R. van den Broeke, C. H. Davis, Y. Li, W. J. van de Berg, and E. van Meijgaard (2008), Mass flux and contribution to sea level rise from the Antarctic Ice Sheet: 1992–2006, *Nature Geoscience*, *In press*.
- Rogers, R. R., and M. K. Yau (1989), *A Short Course in Cloud Physics, International series in natural philosophy*, vol. 113, 3rd ed., Butterworth Heinemann.
- Scambos, T. A., C. Hulbe, M. Fahnestock, and J. Bohlander (2000), The link between climate warming and break-up of ice shelves in the Antarctic Peninsula, *Journal of Glaciology*, 46(154), 516–530.
- Schneider, D. P., and E. J. Steig (2002), Spatial and temporal variability of Antarctic ice sheet microwave brightness temperatures, *Geophysical Research Letters*, 29(20), 1964, doi:10.1029/2002GL015,490.
- Schneider, D. P., E. J. Steig, and J. C. Comiso (2004), Recent climate variability in Antarctica from satellite-derived temperature data, *Journal of Climate*, 17, 1569–1583.
- Shepherd, A., and D. Wingham (2007), Recent sea-level contributions of the Antarctic and Greenland ice sheets, *Science*, 315, 1529–1532.
- Shepherd, A., D. Wingham, T. Payne, and P. Skvarca (2003), Larsen Ice Shelf has progressively thinned, *Science*, 302, 856–859.

- Shindell, D. T., and G. A. Schmidt (2004), Southern Hemisphere climate response to ozone changes and greenhouse gas increases, *Geophysical Research Letters*, *31*(L18209), doi:10.1029/2004GL020,724.
- Smith, B. T., T. D. van Ommen, and V. I. Morgan (2002), Distribution of oxygen isotope ratios and snow accumulation rates in Wilhelm II Land, East Antarctica, *Annals of Glaciology*, *35*, 107–110.
- Smith, R. C., et al. (1999), Marine ecosystem sensitivity to climate change, *Bioscience*, *49*(5), 393–404.
- Sterl, A. (2004), On the (in)homogeneity of reanalysis products, *Journal of Climate*, *17*, 3866–3873.
- Stull, R. B. (1988), *An Introduction to Boundary Layer Meteorology*, Kluwer Academic Publishers.
- Thomas, R., et al. (2004), Accelerated sea-level rise from West Antarctica, *Science*, *306*, 255–258.
- Thompson, D. W. J., and S. Solomon (2002), Interpretation of recent Southern Hemisphere climate change, *Science*, *296*, 895–899.
- Toniazzo, T., J. M. Gregory, and P. Huybrechts (2004), Climatic impact of a Greenland deglaciation and its possible irreversibility, *Journal of Climate*, *17*, 21–33.
- Torinesi, O., M. Fily, and C. Genthon (2003), Variability and trends of the summer melt period of Antarctic ice margins since 1980 from microwave sensors, *Journal of Climate*, *16*, 1047–1060.
- Turner, J., L. A. Lachlan-Cope, J. P. Thomas, and S. R. Colwell (1995), The synoptic origins of precipitation over the Antarctic Peninsula, *Antarctic Science*, *7*(3), 327–337.
- Turner, J., S. R. Colwell, and S. Harangozo (1997), Variability of precipitation over the coastal western Antarctic Peninsula from synoptic observations, *Journal of Geophysical Research*, *102*(D12), 13,999–14,007.
- Turner, J., W. M. Connolley, S. Leonard, G. J. Marshall, and D. G. Vaughan (1999), Spatial and temporal variability of net snow accumulation over the Antarctic from ECMWF Reanalysis project data, *International Journal of Climatology*, *19*, 697–724.
- Turner, J., T. A. Lachlan-Cope, G. J. Marshall, E. M. Morris, and R. Mulvaney (2002), Spatial variability of Antarctic Peninsula net surface mass balance, *Journal of Geophysical Research*, *107*(D13, 4173), doi:10.1029/2001JD000,755.
- Turner, J., S. R. Colwell, G. J. Marshall, T. A. Lachlan-Cope, A. M. Carleton, P. D. Jones, V. Lagun, P. A. Reid, and S. Iagovkina (2005), Antarctic climate change during the last 50 years, *International Journal of Climatology*, *25*, 279–294.
- Turner, J., T. A. Lachlan-Cope, S. Colwell, G. J. Marshall, and W. M. Connolley (2006), Significant warming of the Antarctic winter troposphere, *Science*, *311*, 1914–1917.
- Undén, P., et al. (2002), The High Resolution Limited Area Model, *Hirlam-5 scientific documentation*, Swedish Meteorological and Hydrological Institute, Norrköping, Sweden.
- Van As, D., and M. R. van den Broeke (2006), Structure and dynamics of the summertime atmospheric boundary layer over the Antarctic Plateau: 2. Heat, moisture and momentum budgets, *Journal of Geophysical Research*, *111*(D07103), doi:10.1029/2005JD006,956.
- Van As, D., M. R. van den Broeke, and R. S. W. van de Wal (2005), Daily cycle of the surface layer and energy balance on the High Antarctic Plateau, *Antarctic Science*, *17*(1), 121–133,

- doi:10.1017/S0954102,005.
- Van de Berg, W. J., M. R. van den Broeke, C. H. Reijmer, and E. van Meijgaard (2005), Characteristics of the Antarctic surface mass balance (1958-2002) using a regional atmospheric climate model, *Annals of Glaciology*, *41*, 97–104.
- Van de Berg, W. J., M. R. van den Broeke, C. H. Reijmer, and E. van Meijgaard (2006), Reassessment of the Antarctic surface mass balance using calibrated output of a regional atmospheric climate model, *Journal of Geophysical Research*, *111*(D11104), doi:10.1029/2005JD006,495.
- Van de Berg, W. J., M. R. van den Broeke, and E. van Meijgaard (2007), Heat budget of the East Antarctic lower atmosphere derived from a regional atmospheric climate model, *Journal of Geophysical Research*, *112*(D23101), doi:10.1029/2007JD008,613.
- Van den Broeke, M. R. (1997), Spatial and temporal variation of sublimation on Antarctica: Results of a high-resolution general circulation model, *Journal of Geophysical Research*, *102*(D25), 29,765–29,777.
- Van den Broeke, M. R. (2005), Strong surface melting preceded collapse of Antarctic Peninsula ice shelf, *Geophysical Research Letters*, *32*(L12815), doi:10.1029/2005GL023,247.
- Van den Broeke, M. R., and N. P. M. van Lipzig (2002), Impact of polar vortex variability on the wintertime low-level climate of east Antarctica: results of a regional climate model, *Tellus*, *54A*, 485–496.
- Van den Broeke, M. R., and N. P. M. van Lipzig (2003), Factors controlling the near-surface wind field in Antarctica, *Monthly Weather Review*, *131*(4), 733–743.
- Van den Broeke, M. R., and N. P. M. van Lipzig (2004), Changes in Antarctic temperature, wind and precipitation in response to the Antarctic Oscillation, *Annals of Glaciology*, *39*, 119–126.
- Van den Broeke, M. R., J.-G. Winther, E. Isaksson, J. F. Pinglot, L. Karlöf, T. Eiken, and L. Conrads (1999), Climate variables along a traverse line in Dronning Maud Land, East Antarctica, *Journal of Glaciology*, *45*(150), 295–302.
- Van den Broeke, M. R., N. P. M. van Lipzig, and E. van Meijgaard (2002), Momentum Budget of the East Antarctic Atmospheric Boundary Layer: Results of a Regional Climate Model budget of the East Antarctic atmospheric boundary layer: Results of a regional climate model, *Journal of the Atmospheric Sciences*, *59*, 3117–3129.
- Van den Broeke, M. R., C. H. Reijmer, and R. S. W. van de Wal (2004a), Surface radiation balance in Antarctica as measured with automatic weather stations, *Journal of Geophysical Research*, *109*(D09103), doi:10.1029/2003JD004,394.
- Van den Broeke, M. R., C. H. Reijmer, and R. S. W. van de Wal (2004b), A study of the surface mass balance in Dronning Maud Land, Antarctica, using Automatic Weather Stations, *Journal of Glaciology*, *50*(171), 565–582.
- Van den Broeke, M. R., C. H. Reijmer, D. van As, R. S. W. van de Wal, and J. Oerlemans (2005), Seasonal cycles of Antarctic surface energy balance from automatic weather stations, *Annals of Glaciology*, *41*, 131–139.
- Van den Broeke, M. R., C. H. Reijmer, D. van As, and W. Boot (2006a), Daily cycle of the surface energy balance in Antarctica and the influence of clouds, *International Journal of Climatology*, *26*, 1587–1605.

- Van den Broeke, M. R., W. J. van de Berg, and E. van Meijgaard (2006b), Snowfall in coastal West Antarctica much greater than previously assumed, *Geophysical Research Letters*, *33*(L02505), doi:10.1029/2005GL025,239.
- Van den Broeke, M. R., W. J. van de Berg, E. van Meijgaard, and C. H. Reijmer (2006c), Identification of Antarctic ablation areas using a regional atmospheric climate model, *Journal of Geophysical Research*, *111*(D18110), doi:10.1029/2006JD007,127.
- Van den Hurk, B., and P. Viterbo (2003), The Torne-Kalix PILPS 2(e) experiment as a test bed for modifications to the ECMWF land surface scheme, *Global and Planetary Change*, *38*, 165–173.
- Van der Veen, C. J. (1998), Fracture mechanics approach to penetration of surface crevasses on glaciers, *Cold Regions Science and Technology*, *27*, 31–47.
- Van Lipzig, N. P. M., and M. R. van den Broeke (2002), A model study on the relation between atmospheric boundary-layer dynamics and poleward atmospheric moisture transport in Antarctica, *Tellus*, *54A*, 497–511.
- Van Lipzig, N. P. M., E. van Meijgaard, and J. Oerlemans (2002a), Temperature sensitivity of the Antarctic surface mass balance in a regional atmospheric climate model, *Journal of Climate*, *15*, 2758–2774.
- Van Lipzig, N. P. M., E. van Meijgaard, and J. Oerlemans (2002b), The spatial and temporal variability of the surface mass balance in Antarctica: results from a regional atmospheric climate model, *International Journal of Climatology*, *22*, 1197–1217.
- Van Lipzig, N. P. M., J. C. King, T. A. Lachlan-Cope, and M. R. van den Broeke (2004), Precipitation, sublimation, and snow drift in the Antarctic Peninsula region from a regional atmospheric model, *Journal of Geophysical Research*, *109*(D24106), doi:10.1029/2004JD004,701.
- Van Ommen, T. D., V. Morgan, and M. A. J. Curran (2004), Deglacial and Holocene changes in accumulation at Law Dome, *Annals of Glaciology*, *39*, 359–365.
- Vaughan, D. G., and C. S. M. Doake (1996), Recent atmospheric warming and retreat of ice shelves on the Antarctic Peninsula, *Nature*, *379*, 328–331.
- Vaughan, D. G., J. L. Bamber, M. B. Giovinetto, J. Russell, and A. P. R. Cooper (1999), Reassessment of net surface mass balance in Antarctica, *Journal of Climate*, *12*, 933–946.
- Vaughan, D. G., G. J. Marshall, W. M. Connolley, J. C. King, and R. Mulvaney (2001), Devil in the detail, *Science*, *293*, 1777–1779.
- Vaughan, D. G., G. J. Marshall, W. M. Connolley, C. Parkinson, R. Mulvaney, D. A. Hodgson, J. C. King, C. J. Pudsey, and J. Turner (2003), Recent rapid regional climate warming on the Antarctic Peninsula, *Climate Change*, *60*, 243–274.
- Velicogna, I., and J. Wahr (2006), Measurements of time-variable gravity show mass loss in Antarctica, *Science*, *311*, 1754–1756.
- White, P. W. (2001), *Part IV, Physical processes (CY23R4)*.
- Wingham, B. J., A. Shepherd, A. Muir, and G. J. Marshall (2006), Mass balance of the Antarctic ice sheet, *Philosophical Transactions of the Royal Society A*, *364*, 1627–1635.
- Winther, J.-G., M. N. Jaspersen, and G. E. Liston (2001), Blue-ice areas in Antarctica derived from NOAA AVHRR satellite data, *Journal of Glaciology*, *47*(157), 325–334.
- Zhang, Y., W. B. Rossow, A. A. Lacis, V. Oinas, and M. I. Mishchenko (2004), Calculation of radiative fluxes from the surface to top of atmosphere based on ISCCP and other global data

- sets: Refinements of the radiative transfer model and the input data, *Journal of Geophysical Research*, 109(D19105), doi:10.1029/2003JD004457.
- Zwally, H. J., and M. B. Giovinetto (1995), Accumulation in Antarctica and Greenland derived from passive-microwave data: a comparison with contoured compilations, *Annals of Glaciology*, 21, 123–130.
- Zwally, H. J., and Y. Li (2002), Seasonal and interannual variations of firm densification and ice-sheet surface elevation at the Greenland summit, *Journal of Glaciology*, 48(161), 199–207.
- Zwally, H. J., M. B. Giovinetto, J. Li, H. G. Cornejo, M. A. Beckley, A. C. Brenner, J. L. Saba, and D. Yi (2005), Mass changes of the Greenland and Antarctic ice sheets and shelves and contributions to sea-level rise: 1992–2002, *Journal of Glaciology*, 51(175), 509–527.

Samenvatting

Antarctica is het ongewoonste continent op aarde. Het continent, bekend van de pinguïns, is bijna geheel bedekt met een ijskap die maar liefst 70% van al het zoetwater op aarde bevat. Het klimaat van Antarctica kent op aarde geen gelijke. De laagste temperatuur nabij de grond, te weten $-89.2\text{ }^{\circ}\text{C}$, is hier gemeten en aan de kust van Antarctica is de hoogste maandgemiddelde windsnelheid (16.9 meter per seconde) waargenomen.

Hoewel Antarctica bijzonder afgelegen ligt, is het klimaat van Antarctica op vele manieren onlosmakelijk verbonden met het klimaat van de rest van de aarde. De ijskap bevat zoveel ijs, dat wanneer al dit ijs aan de oceaan zou worden toegevoegd, het zeewaterniveau met 60 meter zou stijgen. Antarctica zendt netto meer straling uit dan dat het ontvangt en speelt daardoor een belangrijke rol in het warmtebudget van de aarde.

Het is daarom belangrijk om de eigenschappen van het klimaat van Antarctica te kennen, mede in het licht van mogelijke klimaatsveranderingen. In deze dissertatie worden twee aspecten van het klimaat van Antarctica onderzocht, te weten de oppervlakte massabalans (OMB) en het warmtebudget van de troposfeer¹ boven Antarctica. Het onderzoek is gedaan door de uitvoer van een regionaal klimaatmodel te bekijken. De reden om modeluitvoer te gebruiken is tweevoudig. Allereerst zijn er te weinig observaties op Antarctica om daarmee een volledig en gedetailleerd beeld van het klimaat te krijgen. Met een weermodel is een volledig en gedetailleerd beeld wel haalbaar. Daarnaast verschaffen weermodellen inzicht in de fundamentele processen die het weer en het klimaat bepalen, iets wat met observaties alleen praktisch onhaalbaar is. Voor het onderzoek naar Antarctica prevaleren regionale weermodellen boven grootschalige circulatie modellen, omdat regionale weermodellen met meer ruimtelijk detail uitgerekend kunnen worden, en omdat deze beter aangepast kunnen worden aan de typische omstandigheden van Antarctica. In deze dissertatie is het model RACMO2-/ANT gebruikt.

Accumulatie van sneeuw aan het oppervlak van de ijskap, dat wil zeggen, een positieve oppervlakte massabalans (OMB), voedt de Antarctische ijskap. Bij een positieve OMB wordt verse sneeuw na enige tijd bedolven onder nieuwere sneeuw, en comprimeert zo tot ijs. Ijs is relatief makkelijk te vervormen, daarom stroomt het ijs van de ijskap onder invloed van zijn eigen gewicht naar de randen van de ijskap. Na verloop van tijd - dit kan vele duizenden jaren zijn - stroomt het ijs aan de randen van het continent vanuit de ijskap in drijvende ijsplaten.

Vanwege het enorme volume van de Antarctische ijskap hebben kleine veranderingen in het ijsvolume grote impact op het globale zeeniveau. Echter, er bestaat nog veel onduidelijk-

¹De troposfeer is de onderste 7 (aan de polen) tot ± 15 (bij de evenaar) kilometer van de atmosfeer. In de troposfeer speelt zich het weer af.

heid over de huidige bijdrage van Antarctische ijskap aan de zeespiegelstijging. Een van de manieren om deze bijdrage te meten, is het afschatten van zowel de OMB als de totale uitstroom van ijs aan de randen van het continent. Voor deze methode is dus een goede schatting van de OMB onontbeerlijk.

In hoofdstuk 2 van dit proefschrift worden de verschillende componenten van de OMB beschreven. De belangrijkste component is de sneeuwval, weergegeven in Figuur 2.2. Het grootste deel van Antarctica is uitzonderlijk droog, dit komt omdat de zeer koude lucht boven Antarctica ook zeer weinig waterdamp kan bevatten. Daar waar de grootschalige atmosferische circulatie landinwaarts is, bijvoorbeeld op het Antarctische schiereiland, kan jaarlijks meters sneeuw vallen. Ongeveer 7% van de jaarlijkse neerslag verdampt weer en het merendeel van deze verdamping vindt langs de randen van het continent plaats (Figuur 2.3a). De lucht langs de kust is relatief warm en droog en het waait er gemiddeld hard (Figuur 1.2). Verdamping is daarnaast een zomerfenomeen (Figuur 2.6), omdat de verdamping sterk afhangt van de temperatuur. Het smelten van sneeuw (Figuur 2.3b) is over het algemeen onbelangrijk. De uitzondering is het Antarctische Schiereiland (Antarctic Peninsula), waar de jaarlijkse sneeuwsmelt kan oplopen tot een halve meter. Deze drie contributies, te weten: sneeuwval, verdamping en sneeuwsmelt, zijn gebruikt om de OMB te berekenen, deze wordt getoond in Figuur 2.4a. In de schatting van deze dissertatie ontbreekt de invloed van sneeuwdrift op de OMB, lokaal is sneeuwdrift sterk van invloed op de OMB. Omdat dit proces niet in het model is geïmplementeerd, kan er ook geen schatting gemaakt worden van het effect op de OMB. Echter, het zal weinig veranderen aan het globale beeld van de OMB dat uiteindelijk door sneeuwval wordt bepaald. In dit hoofdstuk wordt verder de seizoensafhankelijkheid van de neerslag onderzocht (Figuur 2.6) en de interjaarlijkse variabiliteit van de OMB en zijn componenten (Figuur 2.7).

In hoofdstuk 3 ligt de nadruk op de evaluatie van de gemodelleerde OMB met behulp van observaties. Sectie 3.3 beschrijft de technische vormgeving van de evaluatie. In Figuur 3.5c worden de gemodelleerde en gemeten OMB vergeleken. Wat opvalt is dat de gemodelleerde OMB beter overeenkomt met de metingen dan met de resultaten van *Vaughan et al.* (1999) (vanaf nu afgekort tot V99). De schatting van V99 is gemaakt door de observaties tot een continent omvattend veld te interpoleren, de studie heeft na verschijning als referentieschatting van de OMB gefungeerd. Daarnaast geeft RACMO2/ANT een betere schatting dan V99 voor de metingen die na de verschijning van V99 zijn gepubliceerd. De voorspellende waarde van RACMO2/ANT is dus hoger dan die van V99. Echter, uit de vergelijking blijkt dat RACMO2/ANT de OMB gradiënt van de kust naar het binnenland overschat. De OMB voor de relatief natte kust wordt dus overschat en het droge binnenland wordt nog droger gemodelleerd.

Vanwege de goede prestaties van RACMO2/ANT is het mogelijk om de modelresultaten te kalibreren, het uiteindelijke resultaat is afgebeeld in Figuur 3.7. Het belangrijkste verschil met de schatting van V99 is dat de gekalibreerde schatting van de OMB nog steeds veel hoger is dan de schatting van V99 voor de kustzone, wat resulteert in een 15% hogere schatting van de totale OMB voor heel Antarctica. Het feit dat een andere methode zo'n andere schatting voor de kustzone oplevert, geeft aan dat daar de OMB nog onzeker is. Helaas zijn er in de kustzone maar weinig metingen beschikbaar. Er zijn daarom dringend meer OMB observaties in de kustzone nodig om deze onzekerheid te verkleinen.

In hoofdstuk 4 wordt de onzekerheidsmarge in modelschattingen van de OMB verder uitgewerkt. Er is namelijk nog geen standaardmethode om deze onzekerheidsmarge af te schatten. In de methode wordt allereerst een foutmarge als functie van de gemodelleerde OMB definiëerd. Deze foutmarge wordt exact vastgelegd met behulp van de stelling dat de resulterende relatieve foutenverdeling overeen moet komen met een normale verdeling met een standaarddeviatie van één² (Figuur 4.1). Om deze foutmarge per model gridpunt om te zetten naar een onzekerheid voor grotere gebieden van Antarctica, is de afstand waarover modelfouten met elkaar samenhangen bepaald. Met deze gegevens is de onzekerheid van de OMB schatting voor de afzonderlijke drainage bassins van Antarctica berekend (Figuur 4.3 en Tabel 4.2). De opdeling van Antarctica in drainage bassins wordt in Figuur 4.2 getoond. De onzekerheid van de OMB schatting is groot (30%) voor de kleine natte bassins langs de kust, en kleiner (10%) voor de grotere droge bassins die meer het binnenland bestrijken. Deze getallen reflecteren wederom dat de grootste onzekerheid van de OMB in de kustzone van Antarctica gelegen is.

In de daaropvolgende twee hoofdstukken wordt een ander aspect van het klimaat van Antarctica besproken, namelijk het warmtebudget van de troposfeer boven Antarctica. Het warmtebudget geeft inzicht in hoe de troposfeer van Antarctica aan zijn karakteristieken komt. Het warmtebudget varieert met de hoogte boven het oppervlak en van plaats tot plaats. Beide aspecten worden apart besproken: in hoofdstuk 5 worden de verticale profielen van het warmtebudget besproken; in hoofdstuk 6 de horizontale variabiliteit.

De analyse van het verticale warmtebudget toont duidelijk de dynamische koppeling tussen het oppervlak, de grenslaag en de atmosfeer daarboven. Als voorbeeld hoe het warmtebudget kan helpen bij het begrijpen van de processen in de atmosfeer boven Antarctica, worden hier Figuren 5.6a-c in detail besproken. De resultaten in deze figuren zijn representatief voor het binnenland van Oost Antarctica gedurende de wintermaanden. Figuur 5.6a laat verticale profielen van de potentiële temperatuur³ en de wind zien. Figuur 5.6b toont de verticale energiestromen (energie stromen), waarbij een positief getal een flux naar het oppervlak toe is. Figuur 5.6c toont de profielen van de verschillende warmtebudgetcomponenten.

Gedurende de zuidelijke winter blijft de zon onder de horizon, de energiestroom van zonlicht is nul. Het oppervlak en de atmosfeer daarboven blijven wel continue meer warmtestraling (LW in Figuur 5.6b) uitzenden dan dat deze ontvangen. Het oppervlak verliest gemiddeld -35 W/m^2 . Omdat de atmosfeer ook netto warmtestraling uitzendt, neemt de warmtestralingsflux met de hoogte nog verder in waarde af. Voor het oppervlak geldt dat alle energiestromen samen nul moeten zijn, omdat de temperatuur van het oppervlak over een langere periode gezien gelijk blijft. De negatieve warmtestralingsflux (LW) wordt gecompenseerd door het transport van warmte door middel van turbulentie (SHF). 500 meter boven het oppervlak wordt het transport van warmte door middel van turbulentie nul; door turbulentie wordt warmte uit de onderste honderden meters van de atmosfeer onttrokken. De mate van

²De normale verdeling beschrijft hoe groot de kans is dat een bepaalde waarde wordt gemeten. De gemiddelde waarde heeft de grootste kans; de kans neemt af naar mate de waarde afwijkt van het gemiddelde. De standaarddeviatie geeft aan hoeveel een meting gemiddeld afwijkt. Bijvoorbeeld: de Nederlandse man is gemiddeld 181 cm lang, met een standaard deviatie van 7.5 cm.

³De potentiële temperatuur is de temperatuur die het betreffende luchtpakket zou krijgen als het naar zeeniveau zou worden gebracht. Het samenpersen van lucht verhoogt de temperatuur, zelfs als er geen energie aan het luchtpakket toegevoegd wordt. Door de temperatuur als potentiële temperatuur uit te drukken, is het mogelijk temperaturen op verschillende hoogtes met elkaar te vergelijken.

afkoeling door turbulentie (*SHD*) wordt getoond in Figuur 5.6c, en is maximaal 15 graden Celcius/Kelvin per dag. Deze laag, dicht bij het oppervlak waarin de interactie met de grond intensief is, wordt de grenslaag genoemd. Omdat turbulentie de grenslaag zo sterk probeert af te koelen, wordt deze daardoor daadwerkelijk ook veel kouder (Figuur 5.6a⁴). Om het ‘temperatuurtekort’ te bepalen, vergelijken we de temperatuur in de grenslaag met het achtergrondtemperatuurprofiel (θ_0), dat wordt bepaald door het temperatuurprofiel van boven de grenslaag naar beneden door te trekken. Omdat koude lucht zwaarder is dan warme lucht, stroomt de koude lucht van de grenslaag langs het oppervlak naar beneden. Deze wind wordt de katabatische wind genoemd. De katabatische wind is te zien in Figuur 5.6a; de wind langs de helling naar beneden (V) is alleen vlak bij het oppervlak duidelijk positief. Door de draaiing van de aarde wordt de katabatische wind naar links (n.b. zuidelijk halfrond) afgebogen. De katabatische wind versterkt daarmee in de grenslaag de achtergrondcirculatie (U_{isc}) die op het plateau van Oost Antarctica op elke hoogte aanwezig is. Net als voor het oppervlak moet het warmtebudget van de atmosfeer sluitend zijn voor elke individuele hoogte. *LWD* en *SWD* zijn beide afkoelende processen, er moet dus een balancerend opwarmend proces zijn. De meeste warmte wordt geleverd door de grootschalige neerwaartse beweging van lucht (*AdvV*). Onderin de grenslaag is de horizontale toevoer van warmte (*AdvH*) belangrijk.

Het warmtebudget op het plateau van Oost Antarctica voor de winter is nog behoorlijk eenduidig, maar dicht bij de kust neemt de complexiteit sterk toe. Een belangrijke oorzaak voor deze complexiteit is de verwevenheid van de helling van het oppervlak met de verticale temperatuurverschillen, de katabatische wind en turbulentie. Een grotere helling zorgt voor een sterkere katabatische wind, wat weer voor sterkere turbulentie zorgt en meer turbulentie vermindert de verticale temperatuurverschillen. Als de temperatuurverschillen kleiner worden, wordt de katabatische wind zwakker en de turbulente menging minder effectief en zo wordt er dus een nieuw evenwicht gevonden. Op het plateau is de oppervlaktehelling erg klein, de grenslaag is daarom dun en erg koud. Richting de kust neemt de helling sterk toe, de grenslaag wordt daardoor dikker maar minder koud. Analyse van het warmtebudget geeft meer inzicht in de processen die deze overgang controleren, en daarmee ook inzicht in de gevoeligheid van de grenslaag voor veranderingen.

In Hoofdstuk 6 worden de ruimtelijke patronen in het warmtebudget van de grenslaag onderzocht. In het vorige hoofdstuk hebben we gezien dat turbulentie en de netto emissie van warmtestraling de belangrijkste afkoelende processen zijn in de winter, terwijl de verticale en horizontale toevoer van warmte opwarmende processen zijn. De afkoeling door turbulentie en warmtestralingemissie is tamelijk uniform over Antarctica (Figuur 6.6), toch varieert de 2 meter temperatuur (Figuur 6.1) ook op kleinere ruimteschalen. Met behulp van het warmtebudget wordt duidelijk dat deze variaties in de 2 meter temperatuur worden veroorzaakt door de regionale hoogtevariaties van de ijskap. De stroming in de grenslaag is gekromd rond ruggen en toppen van de ijskap - het windveld probeert de hoogtelijnen te volgen - daardoor divergeert⁵ het windveld hier sterker dan gemiddeld op Antarctica. Als gevolg wordt de neerwaartse beweging van lucht naar het oppervlak versterkt, en daarmee het opwarmend effect van *AdvV*. Daarentegen kromt de stroming rond de dalen zó dat het windveld convergeert,⁶

⁴Figuur 1.2c is een voorbeeld van ‘echte’ temperaturen in een koude grenslaag.

⁵Divergeren is ‘uit elkaar stromen’. Een druppel inkt in een glas water is eerst geconcentreerd, maar divergeert totdat overal evenveel inkt in het water zit.

⁶Convergeren is ‘naar elkaar toe stromen’, het tegenovergestelde van divergeren.

de dalende beweging van lucht wordt sterk onderdrukt en *AdvV* warmt nauwelijks meer op of koelt zelfs af. Toch zijn deze locaties niet direct respectievelijk veel warmer of kouder dan hun omgeving. Dat komt door het middelende effect van de horizontale warmte toevoer (*AdvH*). Stel dat een locatie sterk wordt opgewarmd door dalende lucht, waardoor het veel warmer zou kunnen worden dan zijn omgeving, dan voert de katabatische wind continu koudere lucht uit die omgeving toe, zodat het temperatuurverschil beperkt blijft. Het gevolg is wel dat, ten eerste, *AdvV* en *AdvH* tegengestelde ruimtelijke patronen hebben (Figuur 6.8). Ten tweede neemt in de gebieden met een sterke opwarming door dalende lucht de temperatuur toe langs de stroomlijnen van de wind. Het tegenovergestelde vindt plaats op de locaties waar de dalende beweging is onderdrukt. Daar neemt de temperatuur langs stroomlijnen af. Op deze manier is temperatuur indirect gekoppeld aan de hoogtevariaties van de ijskap.

De hierboven beschreven processen spelen zich vooral in de winter af. Uiteindelijk drijft het continue energieverlies van het oppervlak al deze processen aan. In de zomer compenseert instraling van zonlicht de netto emissie van warmtestraling. Als gevolg daarvan bouwt zich alleen gedurende de korte zomernacht een koude grenslaag op. De componenten van het warmtebudget zijn daarom veel kleiner.

In het laatste hoofdstuk worden enkele suggesties gedaan voor verder onderzoek en verbeteringen van het model. In de hier gepresenteerde analyse van het warmtebudget van de atmosfeer boven Antarctica wordt alleen de klimatologie besproken. Een volgende stap is het bepalen van de natuurlijke variabiliteit van het warmtebudget onder invloed van de bekende forceringsmechanismen van het klimaat van Antarctica. Daarmee zou ook het inzicht kunnen groeien hoe het klimaat van Antarctica in de toekomst kan veranderen. Dit volgende onderzoek zou vooral voor de grenslaag zinvolle resultaten op kunnen leveren. In het onderzoek naar de OMB kan op twee punten winst worden geboekt. Allereerst kan met een hogere resolutie worden gerekend, dat zal vooral de resultaten verbeteren voor de gebieden met een gedetailleerde topografie. Daarnaast moet het effect van sneeuwdrift op de OMB worden meegenomen. Herverdeling van sneeuw door sneeuwdrift is op kleine ruimteschalen een belangrijk proces in de OMB. Om sneeuwdrift echter goed te kunnen modelleren, moet ook de toestand van het sneeuwpakket gedetailleerder worden beschreven. Sneeuwdrift hangt namelijk niet alleen af van de wind, maar ook van de geschiedenis van het sneeuwpakket. Tenslotte worden in dit laatste hoofdstuk de resultaten besproken van een kleine test waarin de valsnelheid van sneeuw kristallen is verminderd. Deze test is uitgevoerd om de gemodelleerde OMB te verbeteren. Het directe gevolg van de verminderde valsnelheid is een toename van de ijsinhoud van wolken, en daarmee het transport door middel van wolken. De test heeft dan ook het beoogde effect, namelijk een toename van de neerslag in het droge binnenland van Antarctica en een lichte afname van de neerslag langs de kust (Figuur 7.1). De toename van de bewolking beïnvloedt echter ook sterk de gemodelleerde energiebalans van het oppervlak, en dus de karakteristieken van de grenslaag. De toename van de bewolking brengt de gemodelleerde warmtestralingsfluxen dichterbij de waarnemingen, de indirecte veranderingen in de grenslaag maken echter dat de algehele representatie van de grenslaag in het model juist minder overeenkomt met de observaties. Deze test laat daarmee zien dat een aanpassing van de valsnelheid van ijskristallen zinvol is, maar alleen tot betere modelresultaten leidt als andere modelparameters tegelijkertijd opnieuw worden geoptimaliseerd.

Dank!

Hoewel alleen mijn naam voorop dit boekje staat, is het een illusie om te denken dat ik ben gepromoveerd zonder hulp van anderen.

Mijn grootste dank gaat uit naar Michiel. Allereerst vanwege het vertrouwen dat je me hebt gegeven door mij indertijd deze AiO positie aan te bieden. Ik ben me bewust dat het een voorrecht is om met een goed model te mogen werken. In de afgelopen vier jaar heb ik met veel plezier onder je supervisie gewerkt, je weet een goede balans te vinden tussen aansturen en vrijlaten. Verder heb je telkens opnieuw je ingezet om mijn engels tot echt engels te transformeren. Het is geen vanzelfsprekendheid dat jij je daar verantwoordelijk voor voelde, daarom ben ik je voor deze minst uitdagende kant van begeleiden het meest dankbaar.

Mijn dank gaat ook uit naar Hans. Je bent gedurende mijn promotie grotendeels op de achtergrond gebleven, ik zie dat als teken van vertrouwen. Toch lijkt er iets bereikt, het binnenklimaat in het BBL is langzaam beter geworden.

Erik wil ik bedanken voor zijn tomeloze inzet om RACMO2/ANT operationeel te houden en zijn inzet om mij wegwijs te maken met het model. Zonder jou zou het modellerwerk op het IMAU een stuk stroever gaan. Ook Carleen wil ik bedanken voor de hulp bij het opstarten.

Promoveren zou een stuk minder leuk zijn als het IMAU niet zo'n gezellige, informele groep was. Het is waardevol dat we betrokken op elkaar zijn, niet alleen op het werkgebied, maar ook op het persoonlijke vlak. Daarnaast zijn de randvoorwaarden goed geregeld; secretariaat, praktisch financieel of qua computerfaciliteiten. Ik wil het 'Zeister kluppie' bedanken voor de gezelligheid buiten kantooruren. Jozanneke, Erik, Guy, Petra, Yvonne, Rianne, Janneke, badmintonners, en alle anderen van het IMAU, bedankt!

Ik wil in het bijzonder mijn kamergenoot Arjen bedanken voor de goede tijd die we samen hebben gehad. Onder het genot van onze eigen koffie hebben we veel bediscussieerd, van *i4D*-var tot de laatste films. Van beide weet je wel iets meer af dan ik, maar dat mocht de pret niet drukken. Je hebt me wat betreft werkinzet zonder twijfel het goede voorbeeld gegeven.

Willine, bedankt voor je liefde en het vertrouwen dat je me door de jaren heen hebt gegeven, je bent fantastisch! Ik wil mijn ouders en schoonouders, (schoon)zussen, stiefbroers en zwagers bedanken voor hun blijvende interesse in de begrijpelijke en onbegrijpelijke kanten van mijn werk.

Het bereiken van deze mijlpaal in het leven maakt me blij en dankbaar. Toch is promoveren best relatief. Titels maken je geleerder, niet wijzer. Mijn dank is aan de Schepper, mijn bede is *Sol iustitiae illustra nos*.

Curriculum Vitae

Willem Jan van de Berg werd geboren op 8 augustus 1979 in Nieuw-Amsterdam, nabij Emmen. Hij groeide op in Apeldoorn, waar hij in 1997 zijn Gymnasium diploma behaalde aan Christelijke Scholengemeenschap Sprengeloo, het voormalig Christelijk Lyceum. Aansluitend volgde hij het EH-Basisjaar aan de Evangelische Hogeschool (EH) te Amersfoort, ter voorbereiding op zijn studie. In 1998 startte hij met de opleiding Meteorologie en Fysische Oceanografie aan de Universiteit Utrecht. In zijn studentenjaren is hij ook actief geweest in de Civitas Studiosorum in Fundamento Reformato, dispuut Sola Scriptura, onder andere bij het organiseren van het tiende lustrum van het dispuut Sola Scriptura. Aan het Utrechtse studentenleven kwam noodgedwongen een einde door zijn afstudeeronderzoek, dat hij bij het Royal Netherlands Institute for Sea Research (NIOZ) op Texel heeft gedaan. Dit onderzoek betrof experimentele verificatie van niet-lineaire getijde effecten in een co-oscillerend getijdebekken. In 2002 studeerde hij af, zowel in de studierichting 'Experimentele Natuurkunde' als 'Meteorologie en Fysische Oceanografie'. Vrijwel aansluitend startte hij zijn promotieonderzoek naar het hedendaagse klimaat van Antarctica met behulp van een regionaal weermodel, waarvan u het resultaat nu in handen hebt. De komende drie jaar zal hij als Post-Doc verbonden blijven aan het IMAU. Hij zal zich richten op het verleden en de toekomst van de Groenlandse ijskap in verschillende en veranderende klimaatsomstandigheden.

Publications

First author

Van de Berg, W. J., M. R. van den Broeke, C. H. Reijmer, and E. van Meijgaard (2005), Characteristics of the Antarctic surface mass balance (1958-2002) using a regional atmospheric climate model, *Annals of Glaciology*, *41*, 97–104.

Van de Berg, W. J., M. R. van den Broeke, C. H. Reijmer, and E. van Meijgaard (2006), Reassessment of the Antarctic surface mass balance using calibrated output of a regional atmospheric climate model, *Journal of Geophysical Research*, *111* (D11104), doi:10.1029/2005JD006,495.

Van de Berg, W. J., M. R. van den Broeke, and E. van Meijgaard (2007), Heat budget of the East Antarctic lower atmosphere derived from a regional atmospheric climate model, *Journal of Geophysical Research*, *121* (D23101), doi:10.1029/2007JD008,613

Van de Berg, W. J., M. R. van den Broeke, and E. van Meijgaard (2008), Spatial Structures in the Heat Budget of the Antarctic Atmospheric Boundary Layer, *The Cryosphere*, *2*, 1-12.

Van de Berg, W. J., M. R. van den Broeke, and E. van Meijgaard (2008), Quantifying the uncertainty in model-based estimates of Antarctic surface mass balance, *In preparation*.

Co-author

Terra, G. M., W. J. van de Berg, and L. R. M. Maas (2005), Experimental verification of Lorentz' linearization procedure for quadratic friction, *Fluid Dynamics Research*, *36*, 175–188.

Van den Broeke, M. R., W. J. van de Berg, and E. van Meijgaard (2006), Snowfall in coastal West Antarctica much greater than previously assumed, *Geophysical Research Letters*, *33* (L02505), doi:10.1029/2005GL025,239.

Van den Broeke, M. R., W. J. van de Berg, E. van Meijgaard, and C. H. Reijmer (2006), Identification of Antarctic ablation areas using a regional atmospheric climate model, *Journal of Geophysical Research*, *111* (D18110), doi:10.1029/2006JD007,127.

Rignot, E., Bamber, J., M. R. van den Broeke, C. H. Davis, Y. Li., W. J. van de Berg, and E. van Meijgaard (2008), Mass flux and contribution to sea level rise from the Antarctic Ice Sheet: 1992-2006, *Nature Geoscience*, *In press*.

Masson-Delmotte, V., S. Hou, A. Ekaykin, J. Jouzel, A. Aristarain, R. T. Bernardo, D. Bromwich, O. Cattani, M. Delmotte, S. Falourd, M. Frezzotti, H. Gallée, L. Genoni, E. Isaksson, A. Landais, M. M. Helsen, G. Hoffmann, J. Lopez, V. Morgan, H. Motoyama, D. Noone, H. Oerter, J. R. Petit, A. Royer, R. Uemura, G. A. Schmidt, E. Schlosser, J. C. Simões, E. Steig, B. Stenni, M. Stievenard, M. R. van den Broeke, R. S. W. van de Wal, W. J. van de Berg, F. Vimeux, J. W. C. White (2008), A review of Antarctic surface snow isotopic composition: observations, atmospheric circulation and isotopic modelling, *Journal of Climate*, *In press*.

Helsen, M. M., M. R. van den Broeke, R. S. W. van de Wal, W. J. van de Berg, E. van Meijgaard, C. H. Davis, Y. Li, I. Goodwin, S. Kaspari (2008), Elevation changes in Antarctica mainly determined by accumulation variability, *Submitted*.

Terra, G. M., W. J. van de Berg, and L. R. M. Maas (2008). Experimental evidence of multiple equilibria in a tidal resonator, *In preparation*.